SPE
Society of Petroleum Engineers

SPE 18427

Implicit Compositional Simulation of Single-Porosity and Dual-Porosity Reservoirs

by K.H. Coats, Scientific Software-Intercomp

SPE Member

This paper was prepared for presentation at the SPE Symposium on Reservoir Simulation in Houston, TX, February 6-8, 1989.

Abstract

This paper describes an implicit numerical model for compositional simulation of single-porosity and dual-porosity oil or gas condensate reservoirs. A 3-component equation-of-state compositional approach is proposed as a desirable alternative to extended black oil modelling, requiring little more computing time than the latter. The approach is illustrated for an actual near-critical volatile oil reservoir. A simple method for reducing implicit formulation time truncation error is described and illustrated. A new bottomhole constraint function is described for better preservation of production well target rates in compositional models. A new matrix-fracture transfer formulation including matrix-fracture diffusion is presented for the dual-porosity description; its accuracy is examined in connection with several test problems where correct results are available from single-porosity simulation. Results are discussed for a 3D 600-block simulation of a highly fractured near-critical volatile oil reservoir.

Introduction

This paper describes a fully implicit numerical model for compositional simulation of multidimensional, three-phase flow in single-porosity and naturally fractured reservoirs. A general description of the model is given, followed by a section giving more detail regarding certain features. The model equations are then presented. The major emphasis here relates to the fractured reservoir application. Therefore, the remainder of the paper describes a new matrix-fracture fluid transfer formulation and estimates its accuracy in connection with a number of example or test problems.

General Description of the Model

The model is fully compositional with a generalized cubic equation-of-state[1] (EOS) for representation of gas-oil phase equilibria and densities. The generalized EOS represents the Redlich-Kwong[2], Soave-Redlich-Kwong[3], Zudkevitch-Joffe Redlich-Kwong[4,5], and Peng-Robinson[6] EOS. A tabular, pressure-dependent K-value option provides an alternative to EOS usage. EOS parameters are obtained using a regression-based PVT program[7]. Different parameter sets are used for reservoir and surface separation calculations. This eases the burden of determining parameters and increases EOS accuracy at reservoir and surface conditions. Viscosities are calculated from the Lohrenz et al correlation[8] and interfacial tension is obtained using the MacLeod-Sugden method[9].

The model simulates 1-, 2- and 3-dimensional flow in Cartesian or cylindrical coordinates. Darcy's Law modified by relative permeability and capillary pressure represents the viscous, capillary and gravity forces. Effects of interfacial tension on capillary pressure are included. The model applies to depletion, water injection, cycling (gas injection), and enriched gas/solvent injection operations in reservoir types ranging from black oil to near-critical volatile oil and condensate to lean gas condensate. Applications include simulation of laboratory experiments, cylindrical-coordinate single-well studies and areal, cross-sectional or 3D field-scale studies.

Implicit formulations generally have a tendency toward greater numerical dispersion effects than the IMPES formulation. A dispersion-control feature is described which reduces sensitivity of results to time step size in some cases.

Production well rate is allocated among layers by pressure and mobility, including an implicit bottomhole constraint treatment to preserve specified target rate. The well rate terms involved are implicit in all variables: compositions, saturations and pressure. A new formulation for the implicit bottomhole target rate constraint gives better preservation of specified rate for the case of compositional simulation.

References and illustrations at end of paper.

Pseudo or extended black oil models are frequently used to approximate compositional effects in volatile oil reservoirs undergoing depletion and/or cycling. There are advantages in many such cases in favor of using a compositional model with a pseudoized, tuned three-component fluid description. These advantages include: easier preparation of PVT data, increased accuracy in representation of compositional phenomena, and only marginally greater computing expense.

The code utilizes mapping so that storage is required only for active grid blocks. For example a 40 x 30 x 5 6000-block grid having 4200 active blocks requires storage for only 4200-block arrays. To our knowledge, this mapping logic was first devised by Dr. A. D. Modine in 1971.

Initial composition may vary with depth throughout the hydrocarbon column in the case of initially undersaturated reservoirs. This depth variation may cross the critical point with near-critical condensate in the upper portions and near-critical volatile oil in the lower portions of the initial column.

The model offers the option of internally-generated vertical-equilibrium (VE) capillary pressure curves[10]. These curves vary in time and from block to block. They reduce the errors and occasional disruptive "steel-plate" effects associated with use of rock capillary pressure curves.

History matching often entails a large number of long runs with production well rates specified as STB/d of oil. Until a good match is approached, runs may encounter erroneously large calculated GOR values with resulting high computing expense. A method of avoiding this is described below. A gathering center logic[11] which has proven useful in field study predictions is also described.

In the dual-porosity case, the model allows reservoir descriptions where the matrix block size and shape vary from block to block throughout the grid. Storage and computing time requirements are proportional to the degree of fracturing. For a 1000 grid block problem with all blocks dual-porosity, these requirements are proportional to 2000. If, due to regional fracturing, only 100 blocks were dual-porosity, then these requirements would be proportional to 1100.

For regionally fractured reservoir descriptions, the model treats the three different types of interblock flow: matrix-matrix flow between blocks in unfractured regions, fracture-fracture flow between blocks in fractured regions, and matrix-fracture flow between block pairs on the interface of such regions. The model can be run in single-porosity mode with virtually no loss of efficiency caused by the presence of dual-porosity code.

The calculations include matrix-fracture liquid-gas and gas-gas diffusion, using a method developed by da Silva and Belery[12].

The linear-solver code includes the three options of D4 (reduced band-width) direct solution[13], iterative block SOR (successive overrelaxation), and the vectorized conjugate-gradient ESPIDO method developed by Don Thurnau.

Discussion of Features

Diffusion

Diffusion is calculated between matrix and fractures within a grid block but not between grid blocks. The matrix-fracture gas-gas and liquid-gas diffusion rates are computed using a method developed by da Silva and Belery. Their method includes detailed equations for calculating diffusion coefficients for each component from the static variable group of (reservoir temperature, component molecular weights and critical properties), and the dynamic group of pressure and compositions. All these variables are present in any compositional model or are calculated in the simulation.

Da Silva proposed some time ago that diffusion can be important in fractured matrix reservoir behavior, especially when injection gas composition (e.g. N_2) differs greatly from native reservoir gas. Computations show that diffusion can act very rapidly to nearly eliminate matrix-fracture composition differences both in the liquid and gas phase. The diffusion ccefficients and rate expressions and their derivatives are coded implicitly in the model.

Table 1 shows the expressions for matrix-fracture gas-gas and liquid-gas diffusion rates. The term τ_{or} is tortuosity, $A\phi/\ell$ is the diffusion "transmissibility" reflecting matrix and grid block dimensions, S_{gg} ($S_{\ell g}$) is a saturation-dependent fraction between 0 and 1, and D_{gg} ($D_{\ell g}$) is the diffusion coefficient, different for each component. Diffusion coefficients for liquid-liquid diffusion can be about 100 times smaller than those for gas-gas diffusion. Liquid-gas coefficients are larger but still less than gas-gas coefficients.

The diffusion rates are illustrated in Table 1 for cells 1 (matrix) and 2 (fracture). If both cells remain 2-phase gas-oil and equilibrate with both the gas-gas and liquid-gas diffusion terms shown, then an equilibrium-state dilemma arises. The equilibrium requirement that all matrix component K-values be equal is a contradiction. The problem is resolved simply by using gas-gas diffusion only. For small matrix blocks (e.g. 1-4 ft. cubes), diffusion is so rapid that gas-gas diffusion alone results in small matrix-fracture composition differences both in the liquid and gas phases.

An estimate of the diffusion transient time is given by solution of the diffusion equation

$$\frac{\partial^2 C}{\partial x_D^2} = \frac{\partial C}{\partial t_D}$$

for initial condition $C(x_D,0) = 1$ and boundary conditions $C(1,t_D) = 0$ and $\partial C/\partial x_D = 0$ at $x_D = 0$, where

$$x_D = x/(\ell/2) \qquad t_D = Dt/\tau_{or}(\ell/2)^2$$

This corresponds to the case of a linear core ℓ feet long initially saturated with fluid of unit concentration and exposed to zero-concentration fluid at $x = 0$ and $x = \ell$. The solution for average concentration is

$$\hat{C} \equiv \int_0^{\ell} C\,dx/\ell = 2\sum_1^{\infty} \frac{1}{\lambda_n^2} e^{-\lambda_n t_D}$$

where λ_n is $(2n-1)\pi/2$. Using first-term approximation, the time t^* necessary for $\hat{C}$ to decay 90% from its initial value is

$$t^* = .85\,\tau_{or}(\ell/2)^2/D.$$

For gas-gas high pressure (e.g. 4500 psia) diffusion, a representative D value is .001 cm^2/sec. For a 1-ft. core and a tortuosity value of 3.5, $t^* = 8$ days. The same analysis performed in three dimensions gives a lower transient time. For practical purposes this is instantaneous.

The Extended Black Oil Application

The extended black oil model generally requires 3 and sometimes 4 (non-aqueous) components. Its computing time then reflects the solution of 4 or 5 equations (per grid block). Its PVT treatment frequently involves multidimensional tables representing certain rules established for presence/absence of various components in the various phases.

Today's EOS compositional technology allows an alternative approach. A black- or volatile-oil laboratory PVT dataset can be used with EOS regression to obtain a pseudoized 3-component fluid description. This 3-component description can represent the oil in respect to reservoir volumetric (expansion) behavior, multiple-contact revaporization under gas injection, and surface separation behavior. If CO_2 or N_2 are to be injected, then this approach entails 4 components, the same as the extended black oil.

The 3-component EOS compositional approach offers several advantages. First, the PVT treatment is both easier and more accurate. Frequently, extended black oil models involve significant effort to devise and code tabular representations of PVT behavior which become increasingly complex. The results in some cases include:

a) distorted PVT behavior causing computational running problems,
b) difficulty in understanding and preparing PVT input data requirements,
c) difficulty in designing meaningful laboratory tests to determine PVT parameters, and
d) difficulty in representing multicomponent surface separations.

The EOS 3-component approach is easier, involving repeated multivariable regressions on a collection of fluid behavior data. The EOS approach should also be more accurate. Whatever its complexity, the extended black oil PVT treatment attempts to represent what are simply compositional phenomena generally handled well by today's EOS compositional technology. The EOS regression on a 3-component basis allows adjustment of a number of EOS parameters and introduces a PVT continuity or consistency over all pressure and compositions. All components are present in both hydrocarbon phases in a manner continuously dependent upon pressure and composition.

This is not to say that any collection of oil (black or volatile) data representing numerous and different types of tests will always be matched accurately by the 3-component EOS description. However, in any case the data should be matched as well or better by the latter than by the extended black oil PVT treatment.

A common argument in favor of the extended black oil model is that the few pseudo components give a faster running model. This is not necessarily true. For the same number of components, the compositional model frequently will require little more computing time. An arguable conclusion is that the compositional model should have a black-oil option for the conventional 2-component black oil case, and any extended black oil PVT behavior should be addressed by the 3-component compositional simulation.

The oil Reservoir A study discussed below is an example of 3-component compositional representation of a volatile oil in a reservoir subjected to depletion and gas injection. Table 2 gives the 10-component composition and some bubble-point data for volatile Oil A. Also listed are the pseudo 3-component description and corresponding EOS regressed match of data at the 266 deg. F. reservoir temperature. Table 2 includes the 3-stage surface separation conditions and the regressed match of data for the 10-component and 3-component descriptions. Figs. 1 and 2 show the differential expansion data and the regressed match for the 10-and 3-component descriptions.

Multiple-contact oil vaporization is a mechanism of some importance in Reservoir A due to the 86% methane content of injected gas. Previous experience in compositional simulation indicates that accuracy in EOS-computed multiple-contact vaporization requires a split of the heavy C_{7+} fraction into several subfractions. In this case no laboratory vaporization test data were available. Therefore, the PVT program was used to generate a 10-point vaporization "test" using the tuned (regressed) 10-component description. This description includes the C_{7+} fractions split into 3 subfractions. The computed results were treated as "data" and entered as part of the dataset for the 3-component regression. Fig. 3 shows the agreement between 3-and 10-component calculations of multiple-contact vaporization.

Overall, Table 2 and Figs. 1-3 illustrate a good approximation of Oil A available data using the 3-component description. The tuned EOS parameters are different for the reservoir and surface calculations.

Vertical-Equilibrium Capillary Pressure Curves

The laboratory or rock capillary pressure (P_c) curve reflects the relationship between capillary pressure and saturation at a point (e.g. grid block center). The VE or integrated curve[10] relates P_c at the point to the average saturation over the grid block height interval encompassing the point. The VE curve is obtained by integrating the laboratory curve over a capillary pressure increment equal to the product of block height and water-oil or gas-oil density difference. Thus each grid block has a different VE P_c curve and the curve changes with time reflecting changes in fluid densities. The gas-oil VE P_c curve also reflects changing interfacial tension.

Used in equilibration of reservoirs having initial gas-oil and/or water-oil contacts, VE P_c curves give the exactly correct initial fluids-in-place. Rock P_c curves give errors in these quantities which increase as the ratio of block thickness to transition zone height increases.

Under dynamic conditions, the VE P_c curves reflect the underlying equilibrium state without assuming that the dynamic fluid distribution is segregated or, in any sense, in equilibrium. If the reservoir were shut-in and allowed to aproach equilibrium, the calculated equilibrium fluid distributions are more correct if VE rather than rock P_c are used.

Table 3 shows differences in initial fluid-in-place values calculated using VE and rock capillary pressure curves for a 400-ft. column with gas-oil and water-oil contacts. Calculations are given for the number of layers (N_z) ranging from 20 (Δz = 20 ft.) to 10, 5, 2 and 1 (Δz = 400 ft.). The VE P_c results are correct and identical for all N_z values. The rock P_c results are good for N_z = 10 and 20 and are only a few per cent in error for N_z = 5. The rock curve results exhibit severe error for N_z values below 5.

The VE P_c curves give better accuracy for a given number of layers and in some cases allow fewer layers by preserving accuracy in regard to definition or transition zone saturation distributions. They also prevent the "steel

plate" condition which occasionally arises during simulation with rock curves. This term refers to the case where a grid block pair interface is temporarily sealed to all flow because (e.g.): a) gas in the upper block does not want to flow down and oil in the lower block does not want to flow up, and b) oil mobility is zero in the upper and gas mobility is zero in the lower block. This phenomenon is most likely to occur when permeability is high, viscous pressure gradients are low and rock P_c is low. It can act in a very destructive or destabilizing manner in implicit formulations.

In the dual-porosity case, capillary pressure is assumed zero in the fractures. The resulting fracture grid block VE P_c curves are:

$$P_{cwo}^{VE} = (1 - 2 S_{wf}) h (\gamma_w - \gamma_o)/2 \quad (1a)$$

$$P_{cgo}^{VE} = (2 S_{gf} - 1) h (\gamma_o - \gamma_g)/2 \quad (1b)$$

Equilibration with the VE matrix and fracture P_c curves gives correct fluid distributions and initial gas-oil and water-oil contacts which are horizontal throughout the fracture system. Fracture saturations are between 0 and 1 in grid blocks intersected by the contacts. Also, within each grid block the matrix and fractures are in equilibrium in the sense that a model run with zero well rates will exhibit no saturation or pressure changes. The matrix and fracture VE P_c curves are used for equilibration and interblock flow but play no role in the matrix-fracture transfer calculations. They are an option in the program and may be deactivated if rock-curve use is desired. Use of nonzero fracture P_c curves gives erroneous initial transition zones in the fracture system.

Well Bottomhole Constraint Equations

In black oil models the bottomhole constraint equations ensuring preservation of production well target rates are easily determined. In compositional models, effective or proper constraint equations are more difficult to determine. The compositional model equations express production rate as mols/d

$$q_{ik} = PI_k (\lambda_o \rho_o x_i + \lambda_g \rho_g y_i)_k (p - p_{wb})_k \quad (2)$$

where i and k denote component and perforated layer, respectively. For a given value of p_{wb}, total wellstream molar rate q and composition z_i are easily obtained from this expression. The multistage surface separation calculation then gives the surface STB/d oil and MCF/D gas rates and compositions. If the well target rate is specified in units of STB/d, then an iterative procedure determines p_{wb} so that the surface oil rate equals the specified STB/d rate at the beginning of each outer iteration. If no bottomhole constraint is used, the well STB/d rate at the end of the iteration will not equal the specified value due to changes in q and z_i over the iteration.

The bottomhole constraint for a well is an equation of the form

$$\delta F = \sum_k \left(\sum_j \left(\frac{\partial F}{\partial P_j} \delta P_j \right)_k \right) = 0 \quad (3)$$

where P_j denotes the compositional model variable set $\{x_i\}$, $\{y_i\}$, p, S_w, S_o, S_g, and δP_j is the new iterate change, $P_j^{\nu+1} - P_j^{\nu}$. The outer sum is over all perforated grid blocks. The objective is choice of an appropriate function F such that invariance of F over the iteration ensures invariance of the STB/d rate over the iteration. Choosing F as the expression for total well bottomhole liquid phase molar rate gives good results if only bottomhole liquid contributes to surface oil. But in general the bottomhole gas phase contributes also to surface liquid. Choosing F as the total bottomhole molar production rate works reasonably well in many cases but can result in rate deviations or in additional outer iterations to reduce them if composition $\{z_i\}$ is changing significantly.

The multistage surface separation results exactly satisfy the equivalent single-stage flash equation

$$0 = \sum_{i=1}^{N_c} \frac{z_i (1 - \hat{K}_i)}{L(1 - \hat{K}_i) + \hat{K}_i} = \sum_{i=1}^{N_c} \frac{z_i}{L + \alpha_i} \quad (4)$$

where

$$\hat{K}_i \equiv y_{is} / x_{is} \qquad \alpha_i \equiv \hat{K}_i / (1 - \hat{K}_i) \quad (5)$$

L is mols of stock tank liquid per mol of feed and subscript s denotes surface compositions. Multiplying numerator and denominator by wellstream molar rate q gives

$$F = \sum_{i=1}^{N_c} \frac{q_i}{q_L + \alpha_i q} = 0 \quad (6)$$

and this is chosen as the constraint function F. q_i is wellstream molar rate of component i and q_L is stock tank rate, mols liquid/d. Assumptions are: over the iteration as q and $\{z_i\}$ change, (a) the α_i values remain unchanged and (b) if q_L remains constant then the corresponding STB/d oil rate remains constant. Both assumptions happen to be very good ones. Thus the constraint equation is

$$\delta F = \sum_{j=1}^{N_c} \frac{\partial F}{\partial q_j} \delta q_j = 0 \quad (7)$$

The variables in F subject to the differentiation are q_i in the numerator and $q = \Sigma q_i$ in the denominator. q_L and α_i are known constants (latest iterate values). Use of Eqn. (7) together with Eqns. (6) and (2) and chain-rule differencing leads to a constraint equation in the form of Eqn. (3).

This constraint equation gives good results even when the bottomhole gas phase is the source of most or all of the surface oil. In the case where specified well rate is MCF/d gas, a similar procedure leads to a constraint function

$$F = \sum_{i=1}^{N_c} \frac{q_i}{q_V + \beta_i q} \quad (8)$$

where $\beta_i = 1/(1 - \hat{K}_i)$ and surface mols/d gas rate q_V and β_i are held constant.

Time Truncation Error Control

Fig. 4 shows a reservoir's total GOR vs. time calculated from the fully implicit formulation with and without the time-truncation error control method. The reservoir is a 3D 8 x 13 x 6 single-porosity grid representation of the fractured Reservoir A described later. The 4380-day simulation run was made using 91-day and 45-day time steps. The figure shows that without the error control, calculated GOR is significantly higher using the larger 91-day steps.

The open and solid circular points represent the same 91-day and 45-day step runs performed with the error control. The sensitivity of results to time step size is reduced significantly. Another point of comparison is

average field pressure, reflecting differences in calculated produced gas, as follows:

Run	Time Steps	Outer Itns.	Error Control	Final GOR SCF/STB	Final P_{avg} PSIA
1	48	102	No	15600	4182
2	96	194	No	13000	4357
3	48	104	Yes	11900	4429
4	96	194	Yes	11500	4463

Initial field pressure was 6943 Psia. The error control feature reduces the 91 vs. 45-day step run p_{avg} difference from 175 psi to 34 psi.

This control feature relates only to immiscible flow, reducing sensitivity of saturation distributions, WOR and GOR to time step size. It does not control the compositional smearing or numerical dispersion effects associated with miscible displacement.

A subtle implication appears in the above tabular results. We prefer implicit over IMPES formulations in cases where maximum IMPES time step is small and computing expense consequently high. However, the implicit formulation generally requires much more arithmetic per step than IMPES and to come out ahead (of IMPES) we must use a large time step in the implicit model. If, however, as shown here, the implicit model time step requires constraint to reduce truncation error, then we are defeating our purpose. The 45-day step runs required twice the computing expense of the 91-day step runs. Thus a method of reducing truncation error is important in regard to computing expense in some cases.

The error control method requires little additional storage and virtually no increased computing time. It is very simple, consisting essentially of a Crank-Nicholson treatment of relative permeabilities. For each phase, the upstream relative permeability used for the new $\ell+1$ outer iteration is

$$\hat{k}_r^{\ell+1} = .5\,(k_{rn} + k_r(S^{\ell+1})) \qquad (9)$$

A violent instability can result when k_r is small and S is decreasing. Methods of protecting against this are numerous and of various complexities. We simply use the fully implicit $\hat{k}_r = k_r(S^{\ell+1})$ when that situation exists. We find no benefit from extending this procedure to capillary pressure and do not apply it to k_r in the dual-porosity matrix-fracture transfer terms.

Maximum Gas Rate

Specification of STB/d oil in history match runs where GOR is a problem can result in a semistable process. As a well GOR rises above its field values, "blowout" can occur. That is, as GOR rises above observed the large free gas rate causes rapid pressure decline - a pressure sink - which in turn results in even higher GOR and higher gas rate -and so on. Also, excessive gas rate at one well can affect its neighbors - reducing pressure regionally, resulting in their erroneously gassing out as well.

The model provides for data entry of a maximum surface gas rate (QGMAX) for each production well. The model then produces the specified STB/d oil rate for each well unless the associated gas rate exceeds the well's entered QGMAX. In the latter event, the well produces the QGMAX gas rate as its target in place of the STB/d oil rate. The occurrence of this event is flagged in the output well summaries (end of step and end of run) and the overall impact of the feature is noted by printing an oil-deficiency variable in each step summary. Oil-deficiency is the total cumulative shortage of oil produced (STB) due to this feature divided by total specified cumulative oil production.

Until a description is tuned to avoid erroneous high GOR values we have a choice of procedure. We can not use the QGMAX feature and simply let the wells blow out, indicating the mismatch. This type of run can take (say) hours of computing time due to very small time steps and/or step cuts due to large changes accompanying blowout. Or we can run with the QGMAX feature with (say) 20-minute runs with high oil-deficiency values. Both runs indicate or tell us the same information - our GOR is too high - but the latter runs tell us that in faster, smoother runs. Also, the QGMAX restraint acts to prevent or reduce the phenomenon of one well's blowout destroying other wells's match or behavior. If GOR is very high, the reservoir voidage effect of a well on QGMAX is not much different than its pressure effect if it were producing specified oil STB/d with correct GOR - provided QGMAX is equal or near the actual gas rate.

In the Reservoir A study discussed below, the QGMAX values were obtained from the history file for each well as the maximum surface gas rates produced over all of history. The end-of-step well summary printout gives oil deficiency by well, showing at a glance which wells are the major culprits in the QGMAX constraint - i.e. which wells have the greatest GOR problems.

Gathering Centers

The wells are assigned in groups to any number of gathering centers (GC). A given GC generally includes a number of production wells and gas and/or water injection wells. Assignment of a GC production target rate results in allocation of that rate among the GC producers on the basis of their current open-flow potentials or deliverabilities. Alternatively, individual production well rates may be specified with omission of a GC production target rate.

GC injection target rates may be specified in three forms: a) absolute units -MCF/d gas and STB/d water, b) fractions of the GC total MCF/d gas and STB/d water production rates, and c) fractions of the total reservoir voidage rate represented by the GC producers. The resulting target injection rates are allocated among the appropriate type GC injectors on the basis of their current injection potentials or injectivities. In the case (c) above, the RB/d voidage rate is converted to MCF/d gas and/or STB/d water injection rates which at current bottomhole pressure give the desired RB/d rate.

In the case of gas injection, the model provides for entry of sales gas, fuel gas, and makeup gas GC values. Entered sales and fuel gas values are subtracted from the GC produced gas to determine gas available for reinjection. If the target injection rate exceeds available gas, makeup gas is added to meet the target. Provision is made for injecting makeup gas first and meeting any difference between available makeup gas and target rate with recycled produced gas. Injection gas composition is calculated from the compositions and amounts of produced and makeup gas constituting the reinjection stream.

If no GC production or injection targets are specified, then all individual well rates must be specified and the assignments of wells to gathering centers becomes an exercise for cosmetic (printout) purposes. The GC feature

is optional; that is, the model can be run with no wells assigned to any gathering centers.

The Model Equations

The conventional single porosity model equations are first reviewed. The model consists of $N_c + 1$ primary equations expressing conservation of mass for N_c hydrocarbon (HC) components and water in each grid block. The HC components include N_2, CO_2 and H_2S and are insoluble in water; water is absent in the oil and gas phases. An additional set of $N_c + 3$ constraint equations apply in each grid block, including N_c equations expressing HC phase equilibrium (equal oil and gas phase component fugacities), and three equations expressing unit sums of HC phase mol fractions and phase saturations. The $2N_c + 4$ unknowns corresponding to these $2N_c + 4$ equations are denoted P_j and are in order $\{x_i\}$, $\{y_i\}$, p, S_o, S_g, S_w.

The time difference notation here is, for any quantity or variable X,

$$\bar{\delta} X \equiv X_{n+1} - X_n \tag{10a}$$

$$\delta X = X^{\ell+1} - X^{\ell} \cong X_{n+1} - X^{\ell} \tag{10b}$$

where superscript ℓ denotes outer iteration and subscript n denotes time step level. The new iterate approximation is obtained as

$$X^{\ell+1} = X^{\ell} + \sum_{j}^{2N_c+4} \left(\frac{\partial X}{\partial P_j}^{\ell}\right) \delta P_j \tag{11}$$

A full description of these equations, their linearization and reduction to a set of $N_c + 1$ equations in the $N_c + 1$ primary unknowns $\underline{P}$ is given elsewhere[14]. For each grid block, the $N_c + 3$ constraint equations are used to eliminate $N_c + 3$ unknowns from the $N_c + 1$ primary equations. The remaining set of $N_c + 1$ primary unknowns is denoted $\underline{P}$, a column vector of mol fractions, pressure and saturations dependent upon whether the block is three-phase, two-phase HC-water, or all water. The result is an equation for each grid block of the form

$$C\delta\underline{P} = \Delta(T\Delta\delta\underline{P}) + \underline{R} \tag{12}$$

where bottomhole pressure variable terms are omitted for clarity, C and T are $(N_c+1) \times (N_c+1)$ matrices and $\underline{P}$ and $\underline{R}$ are column vectors of length $N_c + 1$. All phase mobilities in the transmissibility matrix are upstream. The well injection/production terms are implicitly expressed in C and $\underline{R}$. For each bottomhole pressure variable, an implicit constraint equation exists as described above.

For the dual-porosity case, the grid block mass balance Eqn. (12) is:

$$C\delta\underline{P} + C_m\,\delta\underline{P}_m = \Delta(T\Delta\delta\underline{P}) + \underline{R} + C_m(\underline{P}_{mn} - \underline{P}_m^{\ell}) \tag{13}$$

where the term C_m represents the mass storage capacity of the matrix in the grid block. All terms with no m or f subscript are fracture system terms; matrix variables and terms carry the subscript m. No matrix-fracture transfer rates belong or appear in this mass balance. The mass balance equations for the matrix in the grid block are:

$$-\tau_D S_{gg} D_g((\rho_g y_i)_m - (\rho_g y_i)_f)$$

$$-\tau(\lambda_o\rho_o x_i \Delta p + \lambda_g\rho_g y_i(\Delta p + \hat{P}_{cgo})) = V\bar{\delta}(\phi(\rho_o S_o x_i + \rho_g S_g y_i))_m \quad i = 1,2,\ldots N_c \tag{14a}$$

$$-\tau\lambda_w b_w(\Delta p - \hat{P}_{cwo}) = V\bar{\delta}(\phi b_w S_w)_m \tag{14b}$$

where V here is $\Delta x\Delta y\Delta z\,(1-\phi_f)$ and τ is given by Eqn. (23) below. On the left sides, all mobility, ρ, x_i, y_i and b_w values are upstream - matrix or fracture, depending upon flow direction. Δp is $p_{om} - p_{of}$. The diffusion area S_{gg} is calculated as the geometric mean $2 S_{gm}S_{gf} / (S_{gm} + S_{gf})$. The pseudo capillary pressures P_c are discussed below.

These N_c+1 primary equations in $2N_c+4$ unknowns are linearized and N_c+3 unknowns are eliminated using the constraint equations[14]. The result is a set of N_c+1 unknowns expressible in matrix form as:

$$C_m\,\delta\underline{P}_m = \tau(\delta\underline{P} - \delta\underline{P}_m) + \underline{r} \tag{15}$$

where τ and C_m are $(N_c+1) \times (N_c+1)$ matrices. As previously described for the black oil case[17], multiplying this Eqn. by the inverse matrix C_m^{-1} and inserting the resulting expression for $\delta\underline{P}_m$ into Eqn. (13) gives the final single material balance equation in terms of fracture system unknowns.

$$\hat{C}\delta\underline{P} = \Delta(T\Delta\delta\underline{P}) + \hat{\underline{R}} \tag{16}$$

All coefficient matrices or column vectors (excepting $\delta\underline{P}$) contain known elements evaluated at the latest iteration. A linear solver gives the solution $\delta\underline{P}$ and a matrix and column vector saved from Eqn. (15) manipulation then allow calculation of the matrix $\delta\underline{P}_m$ unknown.

The Matrix-Fracture Transfer Formulation

Assumptions and Definitions

Several authors[15-17] give detailed discussions of the dual-porosity fractured reservoir description addressed in this work. As described by Warren and Root[15], the complex fracture system is idealized to a network of intersecting horizontal and vertical fractures. The dual-porosity assumption/description pictures the matrix rock as an array of discontinuous matrix blocks in the continuous fracture system. The effective fracture porosity is small; the matrix provides nearly all the fluid storage capacity.

Effects of viscous gradients in the fracture on matrix-fracture transfer are neglected. The calculated matrix response to changing fracture saturations assumes phase segregation in the fractures. There is no direct flow from matrix block to matrix block within a grid block; nor is there any direct flow from the matrix blocks in a grid block to those in an adjacent grid block. Most of the published dual-porosity formulations[16-23] assume that all matrix blocks in the grid block exist at the same saturation. Litvak[22] and Rossen and Shen[23] are exceptions. The formulation here assumes that matrix block saturations vary with vertical position within the grid block.

The capillary discontinuities at the horizontal fractures have an adverse effect on ultimate recovery compared to a system having no horizontal fractures. Horizontal shale streaks would act in the same manner as fractures insofar as the capillary discontinuity and effect on recovery are concerned.

If the fracture spacings along the Cartesian axes are ℓ_x, ℓ_y, and ℓ_z, respectively, then a grid block of volume $\Delta x\Delta y\Delta z$ contains $\Delta x\Delta y\Delta z\,(1-\phi_f)/\ell_x\,\ell_y\,\ell_z$ matrix blocks. A grid block of height Δz contains a stack of $n = \Delta z/h$ matrix blocks where h is matrix block height (ℓ_z), and n is 1

or greater. The complexity of the matrix-fracture transfer formulation described below reflects an attempt to accurately represent the case where n is considerably larger than 1. A grid block is referred to as a stack of matrix blocks without literal implication that a grid block has only one stack of matrix blocks. Obviously, there are roughly $\Delta x\ \Delta y\ /\ \ell_x\ \ell_y$ identical columns or stacks in one grid block. The term aspect ratio denotes the ratio of block height h to its lateral dimension ℓ_x.

Many authors state or imply that capillary pressure is zero and relative permeability is linear ($k_r = S$ for each phase) in the fractures. Here, these are assumed physically correct fracture properties. Fracture nonzero P_c or nonlinear k_r may be introduced for methodological or other purposes but are not attributed as real properties to the fractures.

The VE P_c option affects only the interblock flow and initial distributions; the matrix-fracture transfer is unaffected by its use or nonuse. Nonzero fracture P_c may be entered as data but it affects only the interblock flow. Nonlinear fracture k_r will affect interblock flow and, as upstream values, the matrix-fracture transfer.

The term immersion denotes the subjection of an oil-saturated matrix block or grid block to a fixed fracture environment of all gas or all water. The term partial immersion refers to exposure of a grid block to a fixed fracture gas/oil or water/oil contact level between the top and bottom of the block. A frequently unstated dual-porosity assumption is that the recovery rate from an immersed stack of n matrix blocks equals n times that of a single immersed matrix block.

There is little interest in the immersion transient in cases where both the true and calculated transient times are small - e.g. 60 days or less. Inaccuracy of a formulation's transient calculation will have little effect on simulated reservoir behavior in such cases.

This and other similar papers present example problem results reflecting their transfer formulations. These results shed little light on the question of accuracy unless they are compared to correct results. This is possible for single-matrix block problems, for some single grid block studies, and, rarely, for full field-scale problems. These correct results are obtained by single-porosity modeling using grids which subdivide the matrix and fractures into grid blocks. Results from these single-porosity and dual-porosity model runs are designated SPM and DPM results, respectively. All SPM calculations are performed using rock P_c and k_r data. An effort is made to present example problems where the correct SPM results can be obtained.

Thomas et al[17] described a dual-porosity model and presented results for several example problems. In certain cases, our model can duplicate their matrix-fracture transfer method. Therefore, for several example problems our DPM results are compared to those obtained using their method. The term DPMT denotes results of their method generated using our model.

Any calculated effect of injection to or production from the matrix in a dual porosity grid block is error. Physically, a 6-inch diameter wellbore can intersect or penetrate at most one of the many matrix block stacks in the grid block. The only possible effect of the matrix is introduction of a skin factor. This is true even if or especially if horizontal fractures are absent and the well/vertical fracture orientations are viewed such that the wellbore intersects no fractures.

Models of the type described here represent a stack of n matrix blocks by a single grid or nodal point. There is a limit to the accuracy obtainable with such coarse, one-point definition. Test or example problems need to show the inaccuracies as well as accuracies of a proposed transfer method. Ideally, a method's areas of accuracy and inaccuracy should relate to dominant and subdominant aspects of reservoir behavior, respectively. Admittedly, it is difficult to generalize in a definition of what the latter are.

The Shape Factor

Warren and Root[15] introduced a shape factor σ to relate matrix-fracture pressure difference and flow rate as,

$$q = \frac{\sigma k V}{\mu} (\bar{p}_m - p_f) \tag{17}$$

for the single-phase case, where q is the flow rate in an element V of bulk reservoir volume and $\bar{p}_m$ is volumetric average matrix pressure. For a cubic matrix block of dimension ℓ and quasi-steady-state (QSS) flow, they gave

$$\sigma = [illegible](N+2)/\ell^2 \tag{18}$$

where N is the number of normal sets of fractures, 1, 2, or 3. Kazemi et al[16] proposed for finite difference simulation,

$$\sigma = 4\left(\frac{1}{\ell_x^2} + \frac{1}{\ell_y^2} + \frac{1}{\ell_z^2}\right) \tag{19}$$

or $12/\ell^2$ for the cubic block case. The value recommended here is

$$\sigma = 8\left(\frac{1}{\ell_x^2} + \frac{1}{\ell_y^2} + \frac{1}{\ell_z^2}\right) \tag{20}$$

More generally, this work simply uses an exchange transmissibility defined by

$$q = \frac{\tau}{\mu} (\bar{p}_m - p_f) \tag{21}$$

For a single matrix block,

$$\tau = 8\left(\frac{k_x \ell_y \ell_z}{\ell_x} + \frac{k_y \ell_x \ell_z}{\ell_y} + \frac{k_z \ell_x \ell_y}{\ell_z}\right) \tag{22}$$

and for the grid block of bulk volume $\Delta x\ \Delta y\ \Delta z$,

$$\tau = 8\left(\frac{k_x}{\ell_x^2} + \frac{k_y}{\ell_y^2} + \frac{k_z}{\ell_z^2}\right) \Delta x\ \Delta y\ \Delta z\ (1 - \phi_f) \tag{23}$$

For QSS single-phase flow, the diffusivity equation can be solved to give exact values of σ for any anisotropy and any matrix block shape. Appendix A gives this calculation. Results for an isotropic, cubic matrix block of dimension ℓ for N=1, 2 and 3 sets of normal fractures are:

	$\sigma\ell^2$			
N	Warren & Root	Analytical QSS Flow	Kazemi et al	This Work
1	12	12	4	8
2	32	28.45	8	16
3	60	49.58	12	24

The shape factor and lengthy associated discussions contribute confusion with little benefit. Single-phase QSS flow is seldom of interest in the reservoir simulation but if it were the above recommended and Kazemi's shape factors are 2 and 4 times too low, respectively. Two blocks of different shape can have the same shape factor; but block shape, especially aspect ratio, can be a dominant parameter

in reservoir behavoir. The shape factor definition loses meaning altogether for anisotropic matrix permeability.

The shape factor is neither helpful nor relevant in the matrix-fracture transfer formulation described here. The two matrix block transmissibilities of interest are τ (Eqn. (22)) and

$$\tau_z = k_z \ell_x \ell_y / \ell_z \qquad (24)$$

The former gives nearly correct results for the imbibition process. Calculation of τ from the shape factor and Eqn. (19) essentially gives imbibition rates corresponding to an effective matrix permeability 1/2 its true value. τ_z is the transmissibility connected with the gravity drainage process.

The transient decay time for single-phase, matrix-fracture flow is generally very small. As developed in Appendix A, the ratio $(\bar{p}_m - p_f) / (p_i - p_f)$ is about .03 at a time

$$t = .1 \mu \phi c \ell^2 / .00633k$$

where matrix initially at pressure p_i is subjected to a constant fracture pressure p_f on all block faces and $\bar{p}_m$ is volumetric average matrix pressure. For properties

$$\mu = 1 \text{ cp} \quad \phi = .3 \quad \ell = 10 \text{ ft.} \quad k = 1 \text{ md} \quad c = 10^{-5} \text{ psi}^{-1}$$

This gives a 97% transient decay at a time of

$$t = .1(1)(.3)(10^{-5})(100) / .00633(1) = .0047 \text{ days}$$

Equilibrium Saturations

Any matrix-fracture transfer method has two fundamental properties. The first is the grid block equilibrium curve, the relationship between grid block fracture and equilibrium matrix saturations. The second is the nature of the transient by which the equilibrium matrix saturation is reached under conditions of partial or full immersion. The grid block equilibrium curve depends upon values of the matrix block equilibrium saturations S_{ge} and S_{we}. S_{ge} (S_{we}) is the matrix block equilibrium gas (water) saturation reached by full immersion of an oil-saturated matrix block in gas (water). Matrix block ultimate oil recovery in pore volumes is equal to S_{ge} and $S_{we} - S_{wc}$ for the gas and water immersion cases, respectively. The matrix block equilibrium saturations are defined first and then used in expressing the grid block equilibrium curve.

Thomas et al proposed the use of pseudo or VE matrix and fracture capillary pressure curves in the driving forces for matrix fracture exchange. That procedure gives correct matrix block equilibrium gas and water saturations for the immersion case. The equilibrium matrix block saturations S_{ge} and S_{we} described here should equal their values.

The gas/oil gravity drainage process has been described and studied by many authors for decades. In particular, van Golf-Racht[24] gives a detailed analysis for the case of drainage accompanying the immersion of an oil-saturated matrix block in fracture gas. Fig. 5 illustrates this process. Gas flows into the matrix block at the top and laterally along the sides. The lateral gas entry rate is highest at the top and decreases to zero at a height $P_{ce}/\Delta\gamma$ above the bottom of the block. Lateral oil flow rate is zero at the block's vertical sides and oil leaves the block only at the bottom. Due to the viscous pressure gradient induced by the downward oil flow, the point of zero lateral gas flow into the block is above point C in Fig. 5 in early stages and moves downward toward C as time increases. Both oil and gas flow are three-dimensional in the matrix but the oil flow is substantially vertical downward.

A key characteristic of this process is the virtual absence of viscous pressure gradient in the gas phase. That is, gas phase pressure essentially obeys $\partial p / \partial z = \gamma_g$ where gas exists, and oil mobility controls the drainage rate. Capillary forces act to retain oil in the matrix and at equilibrium (large time), the gas saturation distribution, curve ABC in Fig. 5 is the section ABC of the capillary pressure curve. The volumetric or integrated average gas saturation at equilibrium is denoted S_{ge},

$$S_{ge} \equiv \frac{1}{h} \int_0^h S_g(z) dz \qquad (25)$$

At equilibrium, capillary pressure is zero at the bottom and $h\Delta\gamma$ at the top of the block, varying linearly as

$$P_c = (h - z)\,\Delta\gamma \qquad (26)$$

where $\Delta\gamma$ is $\gamma_o - \gamma_g$, the gas-oil density difference expressed in psi/ft. This Eqn. gives $dz = -dP_c/\Delta\gamma$ at equilibrium and Eqn. (25) becomes

$$S_{ge} = \frac{1}{h\Delta\gamma} \int_0^{h\Delta\gamma} S_g(P_c) dP_c \qquad (27)$$

which is the area A_{abcd} of Fig. 5 divided by $h\Delta\gamma$. If threshold capillary pressure P_{ce} exceeds $h\Delta\gamma$, S_{ge} is zero and no drainage occurs. If capillary pressure varies with interfacial tension then Eqn. (27) is

$$S_{ge} = \frac{1}{h\Delta\gamma/\sigma_r} \int_0^{h\Delta\gamma/\sigma_r} S_g(P_c)\, dP_c \qquad (28)$$

where P_c in this Eqn. is the invariant rock (laboratory) matrix capillary pressure curve measured at tension σ^o and σ_r is σ/σ^o. S_{ge} varies with pressure and composition in accordance with their effects on the value of $\Delta\gamma/\sigma_r$. For pressure depletion, both increase as pressure decreases, but σ_r increases faster than $\Delta\gamma$. The result is that S_{ge} can decrease significantly as pressure declines.

Fig. 6 shows drainage and imbibition matrix water-oil capillary pressure curves. We defer discussion of the case of a matrix block in the initial transition zone and consider an oil-saturated matrix block with $S_w = S_{wc}$ and $S_g = 0$. Immersion in water results in oil recovery by imbibition and gravity drainage. Imbibition dominates the early transient with fracture water flowing into all six faces of the matrix block. This process slows as matrix water saturation approaches the value where imbibition capillary pressure equals zero (point C on Fig. 6). Gravity drainage then continues with water entering the matrix at the bottom and laterally along the sides in much the same fashion as described for the gas/oil case. During this late drainage process, oil flows out of the block only at the top; none flows laterally out the sides. At equilibrium, capillary pressure is zero at the top and $-h\Delta\gamma$ at the bottom of the block, where $\Delta\gamma$ is $\gamma_w - \gamma_o$, the water-oil density difference, psi/ft. The average matrix block water saturation at equilibrium is S_{we},

$$S_{we} \equiv \frac{1}{h} \int_0^h S_w(z) dz \qquad (29)$$

Capillary-gravitational considerations similar to those of the gas-oil case give

$$S_{we} = \frac{1}{h\Delta\gamma} \int_{-h\Delta\gamma}^{0} S_w(P_c) dP_c \qquad (30)$$

which is the area A_{abcd} of Fig. 6 divided by $h\Delta\gamma$. At equilibrium, water saturations at the top and bottom of the block are those noted by points C and B, respectively.

The grid block equilibrium curves are now discussed. The grid block is a stack of n matrix blocks where n is 1 or greater. Litvak[22] pointed out that partial immersion of a grid block results in drainage (imbibition) only in those matrix blocks above (below) the fracture gas (water) level. Thus for the gas-oil case, the grid block fracture and equilibrium matrix gas saturations are related by

$$S^*_{ge} = S_{gf} S_{ge} \tag{31}$$

This relationship applies for large n and is approximate to a data-dependent degree for n = 1. As an exception, for zero capillary pressure it is exact for all n, including n = 1, and $S_{ge} = 1 - S_{org} - S_{wc}$.

For the water-oil case, the grid block equilibrium curve can be determined exactly for any value of n. We first consider the case of n = 1 or $\Delta z = h$, the case of a single matrix block and its adjoining vertical fractures. The VE capillary pressure curves for matrix and fracture are easily determined. The fracture VE curve is Eqn. (1a). For each S_{wf}, we calculate P^{VE}_{cf} from this Eqn. and find the equilibrium matrix block saturation from the matrix VE P_c curve at this P_c value. The result is shown by the upper curve on Fig. 37, for an example problem discussed later. The data are those of Table 4 and matrix block dimensions are 10 x 10 x 30 ft.

For the case of intermediate n, n = 3 for illustration here, the grid block curve can be constructed using the upper (n = 1) curve. The result is the step-function curve shown on Fig. 37. For large n, the grid block equilibrium curve is

$$S^*_{we} = S_{wf} S_{we} + (1 - S_{wf}) S_{wc} \tag{32}$$

Our DPM formulation uses this Eqn. in a form complicated by considerations of transition blocks and hysteretic behavior. While Eqn. (32) applies only for large n, it is altered as follows for improved accuracy at small n. The S_{wf} value is replaced by

$$\hat{S}_{wf} \equiv (S_{wf} + S^*_{wf})/(1 + S^*_{wf}) \tag{33}$$

where S^*_{wf} is a displacement with a default value of .1. The resulting grid block equilibrium curve

$$S^*_{we} = \hat{S}_{wf} S_{we} + (1 - \hat{S}_{wf}) S_{wc} \tag{34}$$

for $S^*_{wf} = .0856$ is shown on Fig. 37 and agrees more closely with the correct curve for n = 3.

The Transfer Equations

The pseudo capillary pressures in Eqns. (14) are defined here in the context of matrix to fracture phase flow rates at constant pressure with no mass transfer. This aids clarity and does not affect their definitions. This simplified framework is similar to that presented by Rossen and Shen[23]. The phase transfer rates expressed in reservoir volume units for a single matrix block are,

$$q_g = \tau \lambda_g (\Delta p + \hat{P}_{cgo}) \tag{35a}$$

$$q_o = \tau \lambda_o \Delta p \tag{35b}$$

$$q_w = \tau \lambda_w (\Delta p - \hat{P}_{cwo}) \tag{35c}$$

where τ is given by Eqn. (22). The $\hat{P}_c$ terms are pseudo functions for approximate representation of 3D unsteady-state gravity and capillary forces active in the matrix-fracture transfer. Most published dual-porosity transfer formulations are equivalent to these equations; their expressions of capillary pressure and gravity terms define the $\hat{P}_c$ terms in Eqns. (35). $\hat{P}_{cgo}$ and $\hat{P}_{cwo}$ are functions of (S_{gm}, S_{gf}) and (S_{wm}, S_{wf}), respectively. The phase mobilities are upstream values. The fracture mobilities are calculated from linear curves $k_r = S$ for each phase normally but nonlinear fracture k_r data may be entered.

The condition $q_w + q_o + q_g = 0$ allows elimination of Δp from Eqns. (35) to obtain the 3-phase transfer rates in terms of the pseudo functions $\hat{P}_c$

$$q_w = -\tau \frac{\lambda_w}{\lambda}((\lambda_o + \lambda_g)\hat{P}_{cwo} + \lambda_g \hat{P}_{cgo}) \tag{36a}$$

$$q_o = \tau \frac{\lambda_o}{\lambda}(\lambda_w \hat{P}_{cwo} - \lambda_g \hat{P}_{cgo}) \tag{36b}$$

$$q_g = \tau \frac{\lambda_g}{\lambda}(\lambda_w \hat{P}_{cwo} + (\lambda_w + \lambda_o)\hat{P}_{cgo}) \tag{36c}$$

where $\lambda = \lambda_w + \lambda_o + \lambda_g$.

For the water-oil case $S_w = S_{wc}$, $\lambda_w = 0$ and mass balance gives,

$$q_o = \tau \frac{\lambda_{wf}\lambda_{om}}{\lambda_{wf} + \lambda_{om}} \hat{P}_{cwo} = V\phi_m \, dS_{wm}/dt \tag{37}$$

For the gas-oil case, $S_{gm} = \lambda_{gm} = 0$ and mass balance gives,

$$q_o = -\tau \frac{\lambda_{gf}\lambda_{om}}{\lambda_{gf} + \lambda_{om}} \hat{P}_{cgo} = V\phi_m \, dS_{gm}/dt \tag{38}$$

Integration of these equations gives the saturation (recovery) transient in analytical form for given fracture saturations.

$$\int_o^{S_{wm}} \frac{\lambda_{wf} + \lambda_{om}}{\lambda_{wf}\lambda_{om}\hat{P}_{cwo}} dS_{wm} = \frac{\tau}{V\phi_m} t \tag{39}$$

$$\int_o^{S_{gm}} \frac{\lambda_{gf} + \lambda_{om}}{\lambda_{gf}\lambda_{om}\hat{P}_{cgo}} dS_{gm} = \frac{\tau}{V\phi_m} t \tag{40}$$

If the forms of the pseudo functions are known then the grid block equilibrium curve giving matrix saturation as a function of fracture saturation is obtained by setting the pseudo functions to 0.

For the gas-oil case, the well-known gravity drainage equation describing the initial oil rate response to immersion is[24]

$$q_o = \tau_z \lambda_{om} (h\Delta\gamma - P_{ce}) \tag{41}$$

where $\Delta\gamma$ is $\gamma_o - \gamma_g$. The overall transient reflects a complex interaction of matrix P_c, k_{rog} and block height variables. The basis of the method described here is the observation by van Golf-Racht[24] that many researchers have found experimentally and computationally that the

transient immersion response often approximates the exponential form

$$S_g = S_{ge}(1 - e^{-\lambda^* t}) \tag{42}$$

where λ^* is constant. Our SPM calculations agree with this observation. We adopt this form because it gives better results over a wide range of datasets than any other method we have tried.

A $\hat{P}_{cgo}$ definition is sought which exhibits the following behavior:

a) The immersion transient obeys the exponential form Eqn. (42).
b) The grid block equilibrium saturations obey Eqn. (31).
c) For partial immersion, the transient remains invariant with S_g/S_{gf} vs time independent of S_{gf}.
d) The initial oil rate response obeys the form of Eqn. (41)
e) Immersion transient accuracy for a given rock type (k_{rog}, P_c data) is preserved as block height and interfacial tension vary.

Skipping derivational details, the result is

$$\hat{P}_{cgo} = \frac{\tau_z}{\tau}\,\beta_g\,\frac{h\Delta\gamma - P_{ce}}{S_{ge}}\left(1 + \frac{k_{rocw}}{\mu_o \lambda_{gf}}\right)(S_g - S_{gf}S_{ge}) \tag{43}$$

together with the "constant-λ" condition that $k_{rog} = 1$ in the calculation of λ_{om} in Eqn. (35b). β_g is a parameter easily determined by comparing SPM and DPM single-block immersion transients. It is a single parameter for each rock type, not a different parameter for each grid block. Default value is 1. If the constant λ option is deactivated, the DPM immersion transient exhibits too much curvature and a larger β_g value is required. The form (43) satisfies (a) because the left-hand side of Eqn. (38) is linear in S_g. The conditions (b) and (c) are exactly satisfied. Condition (d) is satisfied by inspection. The degree of satisfaction of condition (e) is generally good but is only approximate and problem (data)-dependent.

Real field problems exhibit a complexity of gas-oil exchange behavior which seldom appears in test or conceptual example problems. The following described logic represents only one of many possible approaches for approximate treatment of this complexity. The sign of the term $S_g - S_{gf}S_{ge}$ in Eqn. (43) is important. A negative sign indicates drainage proceeding toward equilibrium. A positive sign may or may not indicate oil flow from fractures to matrix in the grid block. With no additions to Eqn. (43) a positive sign will result in such fracture-to-matrix oil flow. Whether this is correct depends upon the source or cause of the positive sign. A positive value can result from S_g increasing and/or from S_{gf} and/or S_{ge} decreasing. If the positive sign only reflects increasing interfacial tension and lower S_{ge} then oil flow to the matrix should not be allowed. The upper block region, above the fracture gas-oil contact level, contains the matrix blocks drained to a S_g value larger than the new (decreasing) S_{ge}. But there is no oil in the fractures opposite these blocks available for imbibition. Without additional logic, Eqn. (43) will result in false imbibition of fracture oil from below the gas-oil contact into the matrix blocks above the contact. This in turn results in model GOR values erroneously large.

The sign of the term may be positive when oil is actually continuing to drain to the fractures. A grid block may exist at some time near the equilibrium condition. Then a decrease in S_{ge} and an increase in S_{gf} may simultaneously occur in relative degrees such that the term sign is positive. Let S_{gfn} be the fracture contact level at the beginning of this situation. Then above S_{gfn} no exchange takes place. Below the contact in the vertical interval $S_{gf} - S_{gfn}$, matrix blocks are becoming exposed to fracture gas with drainage resulting (matrix-to-fracture oil flow) in that interval related to the new lower S_{ge}. Additional complexities can be descibed at great length.

For brevity, the equations of additional logic are given without lengthy identification of terms with phenomena. Two arrays are carried. The first is S_{gfmx}. S_{gfmx} is reset equal to S_{gf} at the end of every step where the term sign is negative (normal drainage is occurring). The second S_g^* variable is reset as matrix S_{gmn} only when (a) the end-of-step term sign is positive, and (b) $S_{gfn} < S_{gfmx}$ and the new $S_{gf} > S_{gfmx}$. Two cases are considered for a positive term sign. The first case entails a positive term sign together with $S_{gf} < S_{gfmx}$. Imbibition occurs in this case. The term in Eqn. (43) is multiplied by $(S_{gfmx} - S_{gf})$ and the following additive capillary term appears:

$$(S_{gfmx} - S_{gf})\,(P_{cgo}(S_g - S_{gf}S_{ge}) - P_{ce})\,\sigma_r \tag{44}$$

The imbibition capillary pressure is used here.

The second case entails a positive term sign with $S_{gf} > S_{gfmx}$. The terms X and Y are defined

$$X \equiv S_g^* - S_{gfmx}S_{ge}$$
$$Y \equiv S_g - S_{gf}S_{ge} - X \tag{45}$$

The term in Eqn. (43) is replaced by Y. If Y is negative, drainage is occurring and no additional terms are introduced. If Y is positive, imbibition is occurring and the following additive term appears:

$$(P_{cgo}(Y) - P_{ce})\,\sigma_r \quad \text{if } X \geq 0$$
$$(P_{cgo}(S_g - S_{gf}S_{ge}) - P_{ce})\,\sigma_r \quad \text{if } X < 0 \tag{46}$$

The capillary pressures are drainage or imbibition values depending upon whether S_g is increasing or decreasing, respectively.

The water-oil case is now addressed. For clarity subscript m is omitted from all matrix saturations, mobilities and capillary pressures. Fracture saturations carry the subscript f. Subscript w is omitted since all saturations are water saturations. Fig. 7 illustrates the initial water saturation distribution in a grid block lying within the water-oil transition zone. The block's upper interval between points C and E contains mobile oil with an average water saturation S_b at capillary pressure P_{cb}. The lower interval between points E and H contains immobile oil with an average water saturation S_a. The grid block initial average saturation is

$$S_i = S_{Fi}S_a + (1 - S_{Fi})S_b \tag{47}$$

where S_{Fi} is the fractional distance of the point E up from the bottom of the block. S_{Fi} is not fracture water saturation. S_{fi} is zero for the case shown. The point S_b, P_{cb} lies on the grid block matrix VE capillary pressure curve. In terms of areas, the saturations are

$$S_i = A_{abig}/\Delta z \Delta\gamma$$
$$S_a = A_{abed}/(z_e - z_c)\Delta\gamma \quad (48)$$
$$S_b = A_{deig}/(z_h - z_e)\Delta\gamma$$

where $\Delta\gamma$ is $\gamma_w - \gamma_o$.

The maximum grid block-water saturation attainable corresponds to recovery of the mobile oil in the upper interval and is

$$S_{wro} = S_{Fi} S_a + (1 - S_{Fi})(1 - S_{orw}) \quad (49)$$

The block may have an initial saturation S_i near or above $1 - S_{orw}$ and yet have a significant amount of mobile, recoverable oil. The entered k_{row} curve is stored as a function of normalized water saturation $(S_w - S_{wc})/(1 - S_{orw} - S_{wc})$. For blocks where S_{wro} exceeds $1 - S_{orw}$, k_{row} values are calculated using $(S_w - S_{wc})/(S_{wro} - S_{wc})$ for this normalized saturation. This results in oil mobility at all water saturations up to S_{wro}.

Only the matrix blocks in the upper interval of average saturation S_b will imbibe water. As fracture water enters at the bottom of the grid block, no response occurs. This non-response continues until fracture water level rises to point E. As the level rises above point E, imbibition and gravity drainage occur as an increasing number of upper interval matrix blocks become exposed to fracture water. The imbibition rates of the upper interval matrix blocks reflect rock imbibition capillary pressure forces (not VE capillary pressure). These rock capillary forces are associated with the initial capillary pressure P_{cb} of the blocks at saturation S_b, not any total grid block saturation or P_c value.

For $S_f > S_{Fi}$, the grid block saturation at any time is

$$S = S_{Fi} S_a + (S_f - S_{Fi})\bar{S} + (1 - S_f) S_b \quad (50)$$

where $\bar{S}$ is the average saturation in the vertical interval $S_f - S_{Fi}$ and $\bar{S}_i = S_b$. The imbibition capillary pressure curve is stored as a function of normalized saturation

$$\hat{S} = (S_w - S_{wc})/(1 - S_{orw} - S_{wc}) \quad (51)$$

All scanning curves are the same function of normalized saturation but $\hat{S}$ is calculated as

$$\hat{S} = (S^* - S^*_{wc}) / (1 - S_{orw} - S^*_{wc}) \quad (52)$$

The value of S^*_{wc} for each scanning curve is calculated so the curve passes through the point S_b, P_{cb} as shown on Fig. 6. The matrix block equilibrium saturation S_{we} is $A_{djka}/h\Delta\gamma$. The corresponding equilibrium grid block saturation for any S_f corresponds to $\bar{S} = S_{we}$ and is

$$S^*_e = S_{Fi} S_a + (S_f - S_{Fi}) S_{we} + (1 - S_f) S_b \quad (53)$$

The term S^* is

$$S^* \equiv S_{we} + \frac{S^*_e - S}{S^*_e - S_i}(S_b - S_{we}) \quad (54)$$

Setting S to S_i gives $S^* = S_b$ so imbibition P_c equals P_{cb} at time 0, satisfying the equilibrium requirement.

For the simpler case of a grid block lying above the initial transition zone

$$S_a = S_{Fi} = 0$$
$$S_b = S_i = S^*_{wc} = S_{wc}$$
$$S = S_f \bar{S} + (1 - S_f) S_{wc}$$
$$S^*_e = S_f S_{we} + (1 - S_f) S_{wc} \quad (55)$$
$$S^* = S_{we} + \frac{S^*_e - S}{S^*_e - S_{wc}}(S_{wc} - S_{we})$$

The matrix-fracture water-oil transfer Eqn. (37) above is

$$q_o = \tau \frac{\lambda_o \lambda_{wf}}{\lambda_o + \lambda_{wf}} \hat{P}_{cwo} \quad (56)$$

The capillary portion of $\hat{P}_{cwo}$ is

$$\hat{P}_{cwo} = \frac{\lambda_o + \lambda_{wf}}{\lambda_o + \hat{\lambda}_{wf}} \frac{\hat{\lambda}_{wf}}{\lambda_{wf}} P_c(\hat{S}) \quad (57)$$

The term $\hat{\lambda}_{wf}$ is $k^o_{rw} S_f/\mu_w$ where k^o_{rw} is matrix k_{rw} at imbibition $P_c = 0$. This reflects the effective correct inflow value of Thomas et al. The imbibition continues until $P_c = 0$. Therefore any negative values of the imbibition P_c curve are set to 0. Effects of any positive value of imbibition P_c at $1 - S_{orw}$ are also eliminated.

The gravity drainage portion of $\hat{P}_{cwo}$ is treated as an additive effect and stems from the basic equation

$$q_o = \tau_z \beta_w \lambda_o h \Delta\gamma, \quad (58)$$

analogous to the gas-oil drainage equation (41). The term β_w is a parameter of default value 1. The gravity drainage portion is

$$\hat{P}_{cwo} = \frac{\tau_z}{\tau} \beta_w h \Delta\gamma \Psi(\hat{S}) \quad (59)$$

where Ψ is a straight line equalling 1 at $S^* = S_b$ and 0 at $S^* = S_{we}$. The total water-oil pseudo $\hat{P}_{cwo}$ reflecting capillary and gravity forces is then

$$\hat{P}_{cwo} = \frac{\lambda_o + \lambda_{wf}}{\lambda_o + \hat{\lambda}_{wf}} \frac{\hat{\lambda}_{wf}}{\lambda_{wf}} P_c(\hat{S}) + \frac{\tau_z}{\tau} \beta_w h \Delta\gamma \Psi(\hat{S}) \quad (60)$$

For normal cases where imbibition dominates gravity forces, β_w remains 1. For significant gravity effects, SPM immersion results are used to determine a β_w value giving a good DPM match. β_w is a single parameter for each rock type (saturation table), not a separate value for each grid block.

The above treatment is considerably more complex if a feature allowing trapped water is activated. If fracture water advances then recedes, the temporarily exposed matrix may retain its imbibed water. This depends upon the slopes of the drainage and drainage scanning capillary pressure curves. In this case the model treats two grid block matrix saturations, $\bar{S}$ and S_2 (have run out of symbols), with Eqn. (50) appearing

$$S = S_{Fi} S_a + (S_f - S_{Fi})\bar{S} + (1 - S_f) S_2 \quad (61)$$

Initial S_2 is S_b. S_2 is recalculated by mass balance considerations each time step in a manner dependent upon whether fracture water saturation increased or decreased. The result is that if a grid block were to stabilize at some S_f, the matrix saturation above S_f is not S_b but some larger saturation S_2 reflecting earlier temporary periods of exposure to and imbibition of water.

All calculations of S_{ge}, S_{we}, S_a, S_b, etc. in the above equations are internally performed in the model, requiring no external simulations or calculations.

Discussion

Dean and Lo[21] describe several formulations, including dual-porosity. For the gas-oil case they generate a matrix block pseudo capillary pressure curve using full immersion SPM results in Eqn. (38). This gives the correct S_{ge} value. They then generate a pseudo fracture capillary pressure curve which gives correct equilibrium matrix block saturations for partial immersion. They apply the same procedure in the water-oil case. They state that Thomas et al used a matrix pseudo P_c while they use pseudo P_c curves for both fracture and matrix. In fact, Thomas et al used both fracture and matrix pseudo P_c curves. Thomas' curves give the same correct matrix block equilibrium saturations for full and partial immersion as obtained by Dean and Lo. In addition, Thomas' method does this automatically (internally) for matrix blocks of any size or shape and for changing P_{cgo} (with tension), requiring none of the SPM matching effort of Dean and Lo. An advantage of the Dean and Lo procedure lies in its transient accuracy which should be exact in the full immersion case.

Both of the above methods represent the grid block by a single representative matrix block, similar to other dual-porosity formulations[16,19]. The partial immersion transients and equilibrium saturations are those of a single matrix block rather than those of the grid block (stack of matrix blocks).

Rossen and Shen[23] specified a fracture pseudo P_c of $S_{gf}h\Delta\gamma$ (essentially), then generated the matrix pseudo P_c using full immersion SPM results in Eqn. (38). Through a simple, clever transformation they obtain matrix and fracture pseudos which give exactly correct transients and equilibrium matrix saturations for all S_{gf} on a grid block basis -i.e. for a stack of matrix blocks. They applied the same procedure to the water-oil case.

Our difficulties in use of a method similar to Thomas et al were as follows. Reduced gas-oil transient accuracy was observed as h, k_{ro}, and/or P_c data were changed. As a simple example, consider the case of negligible gas-oil capillary pressure. The matrix VE k_{rog} curve is a straight line in this case, independent of the rock curve. The dual-porosity transient is the same for all k_{rog} curves. However, the SPM transient shows wide variations for different k_{rog} curves. In the water-oil case, the SPM imbibition transient reflects the rock capillary pressure curve regardless of block height. However, the vertical equilibrium pseudo P_c curve use gives a dual-porosity transient rate which increases with height. Loosely speaking, the error in the dual-porosity water imbibition transient is proportional to the difference between the pseudo and rock P_c curves. If their method is applied to the water-oil gravity drainage case (negligible rock P_c), the transient error can be large simply because the full matrix block transmissibility is used (when water is present) as opposed to the gravity drainage z-direction transmissibility. A reasonable presumption is that they intend their water-oil formulation for use in the normal case where imbibition dominates gravity drainage.

We tried methods similar to Rossen and Shen, generating pseudo k_{ro} and/or P_c curves from SPM results. Different $h/k_{ro}/P_c$ combinations gave different pseudo curves, requiring, in general, different pseudo curves for each grid block. Even if only one or a limited number of block heights were allowed, the pseudo curves changed with time due to density and interfacial tension changes. In addition, pseudo curves were different for different positions in the initial transition zone(s). Finally, for some datasets, pseudo P_{cgo} curves with negative slope occurred, leading to computational instability. The pseudo curves apply to the drainage (gas-oil) process but do not represent oil imbibition.

Sonier et al[19] emphasize the need for dynamic models rather than previously published static models. Their term static basically refers to the need for external generation of some parameter(s). In particular they referred to the Thomas et al model as static. In fact it is dynamic. Thomas' use of pseudo capillary pressure curves reflects both capillary pressure and gravity forces with no external calibrations or parameters.

Sonier et al pointed out deficiencies in previous formulations' gravity terms and presented their improved method. They illustrated the accuracy of their method in connection with the Kazemi et al five spot waterflood problem[16]. This problem is treated in detail below and is briefly summarized here. The vertically fractured reservoir is a 600 x 600 x 30 ft. five-spot quadrant with 10 x 10 x 30 ft. matrix blocks and an 8 x 8 x 1 DPM areal grid is used. Therefore matrix block and grid block heights are equal and there are no horizontal fractures. Data provided (Table 4) include matrix block permeability, porosity and k_r and P_c data and nonzero fracture P_c and nonlinear fracture k_r data. Here and below we use zero fracture P_c and linear fracture k_r. This has no effect on the observations and conclusions.

Sonier et al showed that their new gravity terms are so correct that with capillary pressures zeroed and only gravity forces active, their model closely reproduces the nonzero P_c Kazemi et al results. This is surprising because the nonzero P_c Kazemi problem is imbibition dominated; gravity forces are insignificant in the matrix-fracture transfer. Results with capillary pressure zeroed and only gravity forces active differ widely from those with the given capillary pressure.

Since we may be in error in understanding the Sonier et al method, their equations are reproduced here as used for the zero P_c water-oil test problem described below. For water-oil matrix to fracture flow they write

$$q_o = \tau \lambda_o (\Delta p + \gamma_o(Z_{wf} - Z_{wm})) \tag{62}$$

$$q_w = \tau \lambda_w (\Delta p - \gamma_w(Z_{wf} - Z_{wm}))$$

where for a single matrix block

$$\tau = .001127\, \ell_x \ell_y \ell_z \sigma k \qquad (\sigma = .08) \tag{63}$$

and

$$Z_{wf} = (S_{wf} - S_{wfi})\, \ell_z \tag{64a}$$

$$Z_{wm} = \frac{S_{wm} - S_{wmi}}{1 - S_{orwm} - S_{wmi}}\, \ell_z \tag{64b}$$

In this problem oil flows from matrix to fracture and water in the opposite direction so for clarity we omit subscripts m and f on mobilities. Eliminating Δp from their equations using $q_o + q_w = 0$ gives

$$q_o = \tau \frac{\lambda_o \lambda_w}{\lambda_o + \lambda_w} (\gamma_o + \gamma_w) \ell_z (S_{wf} - S_{wfi} - \frac{S_{wm} - S_{wmi}}{1 - S_{orwm} - S_{wmi}}) \quad (65)$$

Comparison with Eqn. (37) shows their equivalent gravity drainage pseudo function is

$$\hat{P}_{cwo} = (\gamma_o + \gamma_w) \ell_z (S_{wf} - S_{wfi} - \frac{S_{wm} - S_{wmi}}{1 - S_{orwm} - S_{wmi}}) \quad (66)$$

For the immersion case, $S_{wmi} = S_{wc}$, $S_{wfi} = 0$ and $S_{wf} = 1$ in the above equations. The above equations reflect only their gravity terms. Capillary pressures are zero in accordance with their application to Kazemi's problem.

The zero P_c immersion transient equation for their method is given by equating q_o from Eqn. (65) to $(V/5.6146)\phi_m \partial S_{wm}/\partial t$ where V is matrix block volume $\ell_x \ell_y \ell_z$. We solved this equation with results shown in Fig. 8, using the data of Table 4. Zero P_c SPM results using a 5 x 5 x 10 grid described below are shown for comparison. The error (in our results using their method) is so large that we altered their method as follows. In a later paper Sonier et al[20] state they revised their gravity terms by using phase density differences rather than phase densities in front of their depth terms, as described by Litvak. They also stated this change resulted in insignificant differences for practical and realistic problems. We don't understand what is meant but assume it may somehow result in $\gamma_w - \gamma_o$ appearing in Eqn. (65) in place of $\gamma_w + \gamma_o$. Results using their method with the $\gamma_w - \gamma_o$ substitution are shown in Fig. 8. Again, their new gravity term exhibits large error on the high side. Fig. 8 also shows the zero P_c DPM results for the method described in this paper. Their (revised) gravity term significantly overestimates the true gravity response (P_c = 0). One source of error in their gravity term is the use of total-block τ in place of the smaller, correct z-direction τ_z for gravity drainage. In addition their new gravity term results in gravity drainage even when oil and water densities are equal (see Eqn. (65)).

With capillary pressures included in their pseudo function (66), two additional errors appear. First, setting the pseudo function to zero does not give correct equilibrium matrix block or grid block saturations (S_{we}, S^*_{we}). Second, the fracture k_{rwf} value for imbibition is not constrained to k_{rwm} (P_{cwo}=0) as suggested by Thomas et al.

A subtle aspect of the above zero P_c gravity drainage SPM calculations relates to the proper value of the upstream k_{rwf} value. By analogy to the Thomas et al recommendation for gas-oil gravity drainage, a DPM transfer formulation should use the matrix k_{rwro} value for upstream k_{rwf}, or (presumably) $S_{wf} \times k_{rwro}$ for the partial immersion case. Our gas-oil drainage calculations to date show the SPM grid results are independent of whether upstream k_{rgf} is k_{rgro} (their recommendation) or 1.0. The reason for this is that gas enters the block laterally over the sides as well as from the top and the effective entry transmissibility is much larger than a 1D vertical picture of the process would indicate. The same situation exists here in the zero-P_c water-oil gravity drainage case. Following are SPM water-oil gravity drainage results for the 5 x 5 x 10 and 2 x 1 x 10 grids with $k_{rwf} = k_{rwro} = .2$ and for the 2 x 1 x 10 grid with $k_{rwf} = 1$. These results are for full immersion of the 10 x 10 x 30 ft. block with Table 4 data except that P_c = 0.

Time	S_{wm}		
Days	5 x 5 x 10 k_{rwf}=.2	2 x 1 x 10 k_{rwf}=.2	2 x 1 x 10 k_{rwf}=1
600	.2753	.2750	.2753
1200	.3003	.2993	.3001
2000	.3326	.3301	.3319
3200	.3786	.3726	.3754

The SPM results are essentially independent of k_{rwf} values ranging from .2 to 1, a factor of 5. For drainage, a DPM formulation should use $k_{rwf} = S_{wf}$ and, in the gas-oil case, $k_{rgf} = S_{gf}$.

Wu and Preuss[25] presented a dual-porosity method allowing matrix block subdivision (MINC) and compared results with conventional DPM results. Their MINC results compare very closely with SPM results. In part, they concluded that for single matrix block studies, their MINC method gives more reliable behavior than the conventional DPM. They showed that MINC (matrix block subdivision) is necessary or desirable when fracture water saturation change is rapid, when block size or oil viscosity are large, and when matrix permeability is low.

We consider a case where fracture water saturation change is rapid - the immersion case of instantaneous change from 0 to 1. The data are the Table 4 data with the 10 x 10 x 30 ft. 1 md matrix block. In the gravity drainage case discussed above the saturation gradients in the 5 x 5 x 10 SPM grid at 500 days are large. Near the block bottom, water saturations range from facial grid block values of .37 to .53 to the initial .25 at the interior block. The DPM one-point representation of such gradients by a single average value might be expected to show error indicating a need for matrix subdivision. However, Fig. 8 shows the DPM and SPM results agree well.

For the imbibition case (P_c = Table 4 values) Fig. 36 shows SPM and our DPM results agree well. Wu and Preuss also made this calculation and showed moderately poorer SPM - DPM agreement. Fig. 9 shows our SPM and DPM results for the case where matrix permeability is lowered tenfold to .1 md. The significantly greater accuracy of MINC (SPM here) is evident. However, a practical question arises relating to the shape of the DPM curve. Uncertainty in actual matrix permeability and history matching result in adjustments to match reservoir behavior. The question is whether a reasonable DPM permeability adjustment simply gives a curve crossing the true curve with no overall improvement in match or whether the DPM curve shape is such that significantly greater overall agreement occurs.

The open circles on Fig. 9 show DPM results for k_m = .14, a 40% adjustment. The agreement is significantly better. Large-time agreement is good:

Time	S_{wm}	
Days	5 x 5 x 10	DPM k_m = .14 md
3200	.5488	.5593
5000	.5812	.5912
10000	.6230	.6306
20000	.6536	.6608

The question of need for matrix subdivision is one that can be argued endlessly with little resolution or agreement. Meaningful answers are problem dependent. Nevertheless we have seen little need for subdivision, especially in respect to other error sources in dual-porosity modeling. In the case just treated oil viscosity was 2 cp, the block was 10 x 10 x 30 ft. and permeability was .1 md. The Reservoir A described later has .23 cp oil, .5 md permeability and

maximum block size of 4 ft. cubes. Without belaboring the various scaling criteria, there is simply no need for subdivision in this case.

To some extent, their conclusions regarding DPM inaccuracy may be affected by the DPM model they used. For example, they present DPM imbibition immersion results for a 10-ft. cubic block with data given by Thomas et al. They show rather poor agreement between MINC (SPM) and their DPM results. However for the same problem Thomas et al showed their DPM matched SPM results virtually exactly.

Comparison With Experimental Data

Kleppe and Morse[26] reported imbibition oil recovery data for a single cylindrical matrix block with an annular vertical fracture. The matrix block was .324 ft. in diameter and 4 ft. in height. Their data are given in Table 5. Constant water injection rate at the bottom of the core was 3.3 and 35 cc/min for their low and high-rate tests, respectively. These resulted in roughly constant rates of fracture water level rise of about 11 and 140 ft./d for the two tests.

Beckner et al[27] simulated these experiments in single-porosity and dual-porosity modes using a numerical simulator. Their fine-grid SPM results agreed well with the low-rate test data but showed almost none of the rate dependency necessary to match the high-rate test. Our SPM results shown in Figs. 10 and 11 exhibit significant rate dependence; agreement with data is good at low rate and moderate at high rate. A 5x12 cylindrical-coordinate grid was used and is described in Table 5.

There is no point in pursuing the SPM match of the high-rate test data because Figs. 10 and 11 indicate the data are in error. The SPM calculates recovery and water level both lower than observed. But this cannot be, since if recovery is lower than observed then water level must be greater than observed. Thus a material balance error is present either in the data or the SPM. The latter's material balances are 1.0 to five decimal places. We return to this matter below.

Beckner et al performed dual-porosity simulator runs and reported "The inability of current double-porosity simulation to model imbibition with an advancing water level was clearly shown...". Fig. 12 compares our DPM and SPM results for the low- and high-rate tests. Agreement is good at the low rate. The high-rate case comparison exhibits a difference similar in type (but much less in magnitude) to that which they reported.

Returning to the question of high-rate test data error, we first qualify our usage of the term "data". The data shown here were interpolated from figures in the Beckner et al paper, obviously with some attendant error. Most cases involving comparisons of theory (calculations) and experimental data involve an unresolvable question of whether the data might be wrong and the calculations correct. Fortunately in this case, the nature of the experiment and reported data allow a material balance check. Defining

W = Cumulative water injection, cc
O = Oil recovery from the core (matrix), cc
A = Annular fracture area = 8.2743 cm^2
ℓ = Height of water in the fracture, cm

yields a simple material balance requirement before breakthrough,

$$O = W - A\ell \quad (67)$$

Since the water level and oil recovery data are nearly straight lines, the material balance check may be performed at any one point prior to breakthrough. For the low-rate test at W = 1400 cc, the data are ℓ = 99.3 cm and O = 575 cc. Eqn. (67) gives

$$O = 1400 - 8.2743(99.3) = 578 \text{ cc.}$$

However, for the high-rate test at W = 1200 cc, observed ℓ and O are about 102.5 cm and 440 cc, respectively, and Eqn. (67) gives

$$O = 1200 - 8.2743(102.5) = 352 \text{ cc.}$$

The discussion of rate dependency and the manner of plotting oil recovery in this experiment are somewhat misleading. They give the impression that there is some meaningful adverse effect of water injection rate on recovery. In fact, there is basically no effect or, arguably, a favorable effect of rate on recovery. Ultimate recovery of course is independent of rate. Plotting recovery vs. cumulative water injection shows, for any fixed value of the latter, decreasing recovery with increasing rate. However, a plot of the same recovery vs. time would show, at any fixed value of time, higher recovery at higher rates. The basic recovery process (imbibition) is independent of water injection rate; a given portion of the matrix will imbibe water, once water is available to it, at a rate independent of the velocity of the water flowing through the fracture.

The matrix properties of this experiment provide an example of the type of problem in which the nature of and ability to match the transient are of no practical consequence. The transient imbibition time in this case is a small fraction of a day, which for practical purposes is instantaneous. Any conceivable error in the calculated transient would have no effect on simulated reservoir behavior.

The Cascade or Reinfiltration Effect

The published dual-porosity matrix/fracture exchange formulations reflect an implied assumption that under immersion gravity drainage conditions, recovery rate from a stack of n matrix blocks equals or approximates the recovery rate of n single matrix blocks subjected separately to immersion.

Du Prey[28] and Festoey et al[29] present SPM calculations for a stack of matrix blocks showing that this assumption is wrong. They show that oil draining from the bottom of one matrix block imbibes into the top of the matrix block immediately beneath and does not enter the vertical fractures. The result is that recovery rate from the stack approximates that of a single matrix block initially, and for a long period thereafter the total stack recovery may remain much less than n times the single block recovery. Further, for the partial immersion case, no oil flows to the vertical fractures above the gas/oil fracture contact; oil flow to the vertical fractures occurs at the first matrix block below the contact.

These results have two damaging consequences for models incorporating the assumption. First, the true recovery rate of a grid block is much less than that calculated. Second, and perhaps more serious, in the case of multilayer grids there is no longer any relationship between available oil recovery in a grid block (oil delivered to the vertical fractures) and grid block fracture saturation. For example, consider a reservoir 150 ft. thick modelled with

three 50-ft. layers with a matrix block height of 10 ft. Let the initial fracture gas/oil contact of 0 be lowered to and held at 75 ft. The top grid block will experience increasing matrix gas saturation but none of the corresponding displaced oil appears in that grid block. Rather, it flows to the vertical fractures in the second (middle) grid block. Thus one grid block's delivery of oil to its vertical fractures depends upon other grid blocks' conditions.

To examine this reinfiltration effect, we performed gravity drainage SPM calculations for a single 10 x 10 x 10 ft. matrix block and for a grid block containing a stack of six of these matrix blocks. Data are given in Table 6. For clarity here we refer to the horizontal fractures as the xy fractures. First, the single matrix block was modelled using the 2 x 1 x 7 grid shown in Fig. 13. The calculated recovery curve is shown by the solid line on Fig. 14. Second, the stack of six matrix blocks was modelled using the 2 x 1 x 37 grid of Fig. 13. The recovery curve is shown by the dashed line in Fig. 14. The initial rate is indeed about six times less than the single-block recovery rate, as reported by the above-mentioned authors.

All authors acknowledge that the cartesian network of vertical and horizontal fractures is an idealization of a far more complex reservoir description. The xy fractures, if they exist at all, are not precisely horizontal, just as vertical fractures are not exactly vertical. A third calculation was therefore performed with a .5 ft. downward vertical displacement of each fracture intersection (sub-) block in the 2 x 1 x 37 grid. This corresponds to xy fractures sloping at an angle of about 11 degrees from the horizontal. The resulting recovery curve shown by the triangular points in Fig. 14 agrees closely with the single-block recovery curve.

In summary, with sloping xy fractures, calculated recovery from a stack of six matrix blocks virtually equals six times the recovery of a single matrix block. A conservative conclusion is that SPM results can be obtained to argue in favor or against the assumption, indicating a need for experimental data. The experiments of Saidi et al[31] indicate our sloped-fracture SPM results are erroneous.

Some sensitivity runs were performed for the sloped xy fracture case. The base case reported here used five (sub-) grid blocks vertically for each matrix block with Δz = 3, 3, 2, 1, 1 ft. The xy fracture grid block permeability corresponds to a contribution of about 50 md to x- or y-direction effective fracture system permeability. The fracture slope is 11 degrees. A run was performed using a 2 x 1 x 49 grid with each matrix block Δz = .5, 1, 1.5, 3, 2, 1, 1 ft. to obtain a small grid block at the top of the matrix block. In addition, a vertical displacement of .2 ft. lowered the dip angle to only 4.6 degrees. This run gave a recovery curve lower than but close to the base case curve - a maximum of 2.7 saturation percentage points less over all time. Another run used the 2 x 1 x 37 base case grid and dip angle but lowered the xy fracture permeability by a factor of 10 to a contribution of only 5 md to fracture system effective x- or y-direction permeability. The result was a lower recovery curve with the maximum difference (from base case) of 4.2 saturation percentage points at 600 days.

In all these sloped-fracture stack runs, the saturation distributions in the individual matrix blocks were essentially independent of position in the stack and very similar to the distribution calculated for the single matrix block case.

In these gas/oil calculations, capillary forces tend to promote the imbibition or reinfiltration of oil. The assumption might be more valid in the water/oil case since oil is the non-wetting phase case and P_{cwo} acts to prevent reinfiltration. This can be argued against by considering negative values of imbibition P_{cwo} at each matrix block bottom, but at this point we tire of further speculation.

Gas Oil Examples

The first examples presented here compare SPM and DPM results for constant-pressure gravity drainage. Calculations are performed for the data of Table 6, and for the data of Table 7 which are roughly representative of the Reservoir A properties. The SPM grid is 2 x 2 x N_z for the symmetrical 1/4 element, actually run as a 2 x 1 x N_z with x-direction transmissibilities doubled.

Figs. 15 and 17 compare SPM and DPM 10- and 1-ft. block results for constant-pressure drainage at bubble-point pressure using the data given in Table 6. The equilibrium gas saturations S_{ge} at bubble-point pressure are .498 and .1258 for the 10 and 1 ft. blocks, respectively. These values reflect the gas-oil density difference of .1477 psi, used in Eqn. (28). The calculated large-time or stabilized S_{gm} values are .4998 and .4974 for the SPM and DPM calculations, respectively. The first value is stabilized; the latter is still increasing very slowly at 10000 days.

Fig. 15 shows good agreement between SPM and DPM results for the 10-ft. block using a β_g of 1.14. The agreement with SPM results shows that the recovery curve is closely approximated by the exponential form, Eqn. (42), for these particular k_r and P_c data.

Thomas et al reported better agreement than we show for their method in Fig. 15. This is because they performed their calculations with pressure depletion - about 750 psi pressure decline over 1000 days. This depletion masks the accuracy or evaluation of the transfer formulation since the increase of matrix gas saturation is a combined result of the matrix-fracture transfer and gas evolution or liberation due to pressure decline. This gas evolution reduces the transient time and improves the apparent accuracy of the transfer formulation.

As previously stated, one difficult objective in DPM development is constructing a transfer or exchange formulation which at least approximately preserves accuracy under time and spatial variation of reservoir/fluid properties. Fig. 16 indicates the sensitivity of DPM accuracy to variation in the k_{rog} curve. The curve of Table 6 was reduced by a factor of 3 except for the entry k_{rog} = 1. The DPM with β_g = .485 only approximately matches the SPM results for the 10-ft. block case. The method of Thomas et al gives a higher recovery curve. The DPM and SPM recovery curve shapes show that the SPM recovery curve does not obey the exponential form as well with $k_{rog}/3$ as it did for the original k_{rog}.

Fig. 17 shows SPM and DPM results for the constant-pressure drainage case for the 1 ft. matrix block. The calculations using Thomas' method agree very well with the SPM results; the agreement is essentially the same as they reported. The reason for similarity of their and our comparisons in this case (as opposed to the Fig. 15 10-ft case) is that their depletion was minimal in the 1 ft. case, having less than 100 days to act due to the faster transient. The DPM gives a recovery curve slightly higher than the SPM and DPMT results. The β_g value of 1.14 determined for the 10-ft. block was used; the SPM/DPM curve differences of Figs. 15 and 17 thus indicate the approximate preservation of accuracy of the DPM formulation for a ten-fold variation of block height.

The results just discussed relate to the case of a single matrix block. For the case of a grid block containing a stack of many matrix blocks, the drainage recovery curve for partial immersion (grid block $S_{gf} < 1$) should be identical to the single-matrix block curve provided S_{gm}/S_{gf} is plotted in lieu of S_{gm}. Our DPM gives this result. Our run using the Thomas et al DPM method for $S_{gf} = .5$ gave a stabilized S_{gm}/S_{gf} of .446 for the 10-ft. block case and an S_{gm} of 0 for the 1-ft. case. The .446 value reflects the equilibrium S_{gm} value of .223 for a single 10 ft. matrix block as opposed to the value of .249 for the stack of blocks represented by the grid block. The 0 value of the 1 ft. case reflects the influence of the threshold capillary pressure on equilibrium S_{gm} of a single 1 ft. matrix block for $S_{gf} = .5$.

The procedure suggested by Rossen et al was used with the SPM results shown in Figs. 15 and 17 to calculate pseudo matrix gas/oil capillary pressure curves for the 10 ft. and 1 ft block cases, respectively. Fig. 18 shows that the curves differ greatly for the two different block heights. The implication of this is that in cases of variable block height over the reservoir grid, each grid block would need to have input and storage of a different pseudo curve. The slope of the pseudo curve is satisfactory (positive) for the 1 ft. case but is negative for the 10 ft case at saturations below .3. A negative slope can cause stability or convergence problems.

In this and other unreported cases, the unorthodox integrated curve shapes obtained lead us to question whether we are in error either in understanding or implementing this proposed procedure. For this reason we include Table 8 which gives the SPM S_{gm} vs. time curve for the 10 ft. block. These are the only data missing for the purpose of performing the integration.

Figs. 19 and 20 compare SPM and DPM results for the gas/oil drainage process for the data of Table 7. A 1x1x4 ft. matrix block containing saturated oil is immersed in equilibrium fracture gas at constant bubble-point pressure. Fig. 19 shows that the SPM and DPM results agree fairly well with $\beta_g = 1.3$. As previously stated, the DPM should give an invariant plot of S_{gm}/S_{gf} for the partial immersion case. The circular points in Fig. 19 are a plot of S_{gm}/S_{gf} from the DPM for the case of a constant $S_{gf} = .5$.

The approximate preservation of DPM accuracy for a fixed β_g and different block heights is indicated in Fig. 20. SPM and DPM results are shown for $S_{gf} = 1$ and $\beta_g = 1.3$ for a matrix block height of 1 ft.

Simple pressure depletion may be a dominant mechanism during periods of production with no gas or water injection. Two cases are considered for a single grid block subjected to pressure depletion. Data in Table 7 are used. The grid block of height 24 ft. is a stack of six 1 x 1 x 4 ft. matrix blocks. In the first case, gas evolved in and escaping from the matrix percolates upward through the vertical fractures leaving the grid block's fractures oil-filled. In the second case, caprock or gas-filled fractures in an overlying block prevents this percolation and the evolving matrix gas enters and accumulates in the fractures, resulting in an increasing S_{gf} or declining gas-oil fracture contact. The SPM and DPM grids are 2 x 1 x 24 and 1 x 1 x 2 respectively. A production well produces a constant total RB/day rate from the fractures from 0 to 1200 days and is shut in from 1200 to 2500 days.

Fig. 21 shows the SPM matrix gas saturation, S_{gm}, plotted vs. time. S_{gm} is the volumetric average of gas saturations in the 24 matrix sub-blocks of the 2 x 1 x 24 SPM grid. S_{gm} increases from 0 to 600 days and decreases from 600 to 1200 days. Gas evolution accompanying pressure decline tends to increase S_{gm} while capillary forces along with weaker gravity forces tend to decrease S_{gm} by forcing flow of matrix gas to the fractures. These opposing tendencies become equal at about 600 days with the capillary-gravity forces dominating thereafter. After shut-in at 1200 days, the depletion/evolution effect is absent and the capillary-gravity forces act alone to reduce S_{gm}. The rate of S_{gm} decline diminishes as S_{gm} decreases, due to decreasing k_{rgm} and P_{cgom}.

The DPM results shown by the open circular points in Fig. 21 match the SPM results well. The growing discrepancy at large time reflects the vertical distribution or variation of gas saturation in each matrix block in the SPM calculation. The DPM uses k_{rgm} and P_{cgom} values evaluated at the average saturation value of this distribution. These values are less than the SPM effective values which reflect values integrated over the vertical distribution.

For the results just discussed, a single matrix capillary pressure curve of S_g^3 was used. The triangular-point DPM results in Fig. 21 indicate the effect of use of a $.1*S_g^3$ imbibition curve along with the S_g^3 drainage curve. Results are identical to 600 days since S_{gm} is increasing and only the drainage curve is applicable. After 600 days, S_{gm} declines and the DPM calculation switches to imbibition curve values. The lower imbibition curve results in a lower rate of gas expulsion from the matrix or greater matrix gas retention.

The SPM and DPM calculations give the same matrix pressure and interfacial tension vs. time curves, shown in the lower portion of Fig. 21. The plotted IFT is ratio of tension to initial tension at the initial 5553.7 psia bubble point pressure. The value of nearly 6 at 1200 days means that gas-oil capillary pressures increase six-fold from bubble point to 4200 psia.

For the second depletion case, gas entering the fractures cannot percolate out of the grid block. Oil production rate at the bottom of the block is constant for 1500 days and 0 thereafter. In this case gas simultaneously flows from fracture to matrix and from matrix to fracture at different positions in the grid block. In the upper part of the block, gas flows from fracture to matrix. In the lower part, fractures are oil-filled and gas flows from matrix to fracture. After shut-in at 1500 days, a circulatory type of flow occurs; gas flows from matrix to the fractures in the lower region, percolates upward and enters matrix blocks above the fracture gas-oil contact.

The DPM cannot represent simultaneous flow of a phase in both directions; it can only approximate that situation by a net flow in one direction. Fig. 22 compares SPM and DPM results for this second depletion case, with and without IFT effects. If the latter are ignored, less gas appears in the fractures which, in terms of reservoir performance, translates into lower GOR. The reason for this is that S_{ge} is larger when IFT effects are ignored and larger S_{ge} corresponds to more gas in the matrix and less in the fractures. Fig. 22 shows only moderate agreement of SPM and DPM results for this second depletion case.

Fig. 23 shows pressure and matrix gas saturation vs. time for the SPM and DPM calculations with and without IFT effects. The curves are the same for all four cases. The interfacial tension ratio rises from an initial value of 1.0 to 4.5 at 4430 psia at 1500 days.

Fig. 24 compares SPM and DPM results for the case of fracture oil imbibition into a gas-filled matrix block at constant, bubble-point pressure. This process may occur in the reservoir if oil is pushed upward into a gas-cap grid block or a previously drained grid block. The 1 x 1 x 4 ft. matrix block initial saturations are $S_{gm} = .9$, $S_{wm} = S_{wc} = .1$, and the fracture oil saturation is constant at 1.0. Table 7 gives other data. An imbibition capillary pressure curve of S_g^3 was used.

Fig. 24 shows close agreement between SPM and DPM single-matrix-block results for the case $S_{of} = 1.0$. However, the DPM formulation does not exhibit the proper invariance to partial fracture saturation. The correct (dashed line) and actual (triangular points) DPM results for the case of $S_{of} = .5$ are shown. The correct DPM S_{gm} value is 1/2 the sum of .9 and the DPM S_{gm} value calculated for $S_{of} = 1.0$. The DPM formulation does give the correct asymptotic or large-time value of S_{gm} of .45.

The above discussion and Figs. 15-24 examined the accuracy of the DPM formulation in connection with single matrix block or single grid block behavior. The sensitivity of DPM full-grid simulation results to inaccuracies in the formulation is of equal interest. Fig. 25 shows the DPM single matrix block, constant-pressure drainage curve calculated with (a) $\beta_g = 1.3$ (as in Fig. 19), (b) $\beta_g = 1.0$, and (c) $\beta_g = 1.0$ and the constant-λ option deactivated. The cases (b) and (c) give moderate and large errors in the DPM results for the single-matrix-block case.

The DPM parameters of the three cases (a)-(c) shown in Fig. 25 were used in 12x5 x-z cross-sectional, constant-pressure gas injection, DPM simulation runs. The cross-section grid and well data are given in Table 7. The injected separator gas composition gives a vaporizing gas drive. Average reservoir pressure during the seven years of simulation is about 5600 psia for all runs discussed here. Gas injection rate is constant and the production well is placed on deliverability at a bottomhole pressure of 5500 psia.

Fig. 26 shows that the moderate and large inaccuracies in the DPM single-block behavior translate to small and moderate inaccuracies in the 12x5 cross-sectional results. This tendency of a change in a given model (reservoir or fluid or mechanism) parameter to cause a significantly smaller change in overall simulation results is well known. Nevertheless, (as, indeed, here perhaps) we frequently belabor the accuracy of a model parameter or mechanism without examining its impact on the overall simulation results.

For several years, da Silva[12] has gathered and presented evidence that diffusion may play a very significant role in dual-porosity reservoir behavior, especially when injection gas composition differs greatly from that of the natural reservoir gas. Fig. 27 shows the effect of diffusion in the DPM cross-sectional simulation for the case of separator gas injection. With diffusion included in the calculations, the results show somewhat higher recovery with significantly lower GOR. Fig. 28 shows a greater effect of diffusion when nitrogen is injected. Oil recovery is roughly 60% greater with diffusion while GOR is significantly lower. A crossplot of GOR vs. recovery would illustrate the effect of diffusion more dramatically; at 16% recovery, calculated GOR is 3800 Scf/STB with diffusion and 25,500 Scf/STB without diffusion.

These cross-section runs with the two different injection gases and with and without diffusion exhibited the following general character. A strong fracture gas override existed at early time with a downward vertical movement over time of a nearly piston-like gas-oil interface. The initial S_{ge} value was .5664 at the initial IFT (ratio of tension to initial tension) of 1.0. Rough averages of IFT, S_{ge} and S_{gm} values over blocks where $S_{gf} = 1.0$ at 7 years are as follows:

Case	Inj. Gas	Diffusion	IFT Fracture	IFT Matrix	S_{ge}	S_{gm}
1	Separator	No	7	1.4	.53	.54
2	Separator	Yes	2	2	.50	.53
3	Nitrogen	No	60	5	.37	.37
4	Nitrogen	Yes	40	40	.23	.50

The average S_{gm} of .53 for Case 2 includes several blocks at and near the gas injector where S_{gm} was .9 due to matrix oil vaporization. With diffusion, matrix/fracture gas compositions were nearly identical as were matrix/fracture oil compositions where fracture oil existed. In Case 4, the large difference between S_{gm} (.5) and S_{ge} (.23) reflects a combination of early-time drainage of oil when S_{ge} was larger and vaporization of matrix oil by the high-N_2 content matrix gas. No complete matrix oil vaporization occurred in Case 4. No grid block matrix oil saturation at seven years was less than .3.

Water/Oil Examples

Single-Block Imbibition

SPM and DPM results are compared first for water imbibition into a single matrix block. The accuracy of the DPM results is examined for changes in two variables -block height and the imbibition capillary pressure curve. The two block sizes are 10 x 10 x 10 ft. and 10 x 10 x 30 ft. The first P_c is that given in Table 6. The second, denoted "low P_c", given in Ref. 30, is identical except for the following entries:

S_{wm}	P_{cwo} Table 6	P_{cwo} Low P_c
.2	50.	1.
.25	9.	.5
.3	2.	.3
.35	.5	.15
.4	0.	0.
.45	-.4	-.2

Obtaining the correct SPM results for these cases is not entirely straightforward. A 1/4-element $N_x \times N_y \times N_z$ SPM grid includes horizontal fracture blocks at $k = 1$ and N_z and vertical fracture blocks at $i = N_x$ and $j = N_y$. The choice of k_{rwf} value in these water-filled fracture blocks for upstream use in water imbibition can affect the SPM results by a fraction to several saturation percentage points. In theory, the facial k_{rwf} value is determinable from the boundary condition $S_{wf} = 1$. First thought leads to a value of $k_{rwf} = k^o_{rwm}$ = the matrix k_{rw} at $S_{wm} = S^o_{wm}$ = water saturation at imbibition $P_{cwo} = 0$. This value is .03 for the data here for both P_c curves. However, the block experiences gravity drainage in addition to imbibition with final equilibrium water saturation equalling S^o_{wm} at the top and the S_w of point B in Fig. 6 at the bottom of the block. The maximum possible value of the latter saturation for any block height is $1-S_{orw}$ and the maximum possible corresponding k_{rwf} value is k_{rwro}, which is .23 for the data here. These values of .23 and .03 are over seven-fold different and at various times and block positions, the true facial k_{rwf} upstream value for water flow into the matrix block may span this range. SPM results obtained using fixed $k_{rwf} = .23$ and .03 values are significantly different.

The problem is reso'ved in the following manner. For a given block height and P_c curve, the value of S_w at point B of Fig. 6 is determined. The value of k_{rwm} at this S_w is calculated. The proper k_{rwf} value cannot exceed this k_{rw} and it is used for facial upstream k_{rwf} in the SPM calculation. The resulting k_{rwf} values for the four cases are:

Matrix Block Size	P_{cwo}	k_{rwf}
10 x 10 x 10	Table 6	.069
10 x 10 x 30	Table 6	.108
10 x 10 x 10	Low	.068
10 x 10 x 30	Low	.104

The value of k_{rwf} only affects calculated flow into the first matrix grid block at the matrix/fracture interface. Therefore use of a sufficiently fine grid will give very small dimensions of this first block and the SPM results become insensitive to the value of k_{rwf}. We used a 5 x 5 x 12 grid for the 1/4-element (x = 0 to 5 ft., y = 0 to 5 ft.) with Δx and Δy matrix spacings from center to fracture face of 2.5, 1.5, .7, .3 ft.

Sensitivity runs with other grids and k_{rwf} values indicated the above procedure gives accurate SPM results. The truncation error of N_z = 12 vs N_z = 22 is small even for the 30 ft. block height and is in the opposite direction of the small error of using the maximum possible k_{rwf}. The vertical spacing for N_z = 12 is .001, 10 * (h/10), .001 ft. The SPM calculation is actually performed as a 1/8-element which reduces computing time. The simplest grid is a 2 x 2 x N_z with the matrix grid point at x = y = 2.5 ft. and is equivalent areally to that used in the DPM formulation -also equivalent to the shape factor Eqn. (20). The 2 x 2 x N_z grid is actually run as a 2 x 1 x N_z with x-direction transmissibility doubled. The resulting S_{wm} vs. time curve ranges from a fraction to about 3 saturation points lower than the 5 x 5 x N_z grid.

Fig. 29 shows SPM and DPM results for the 10 ft. block and Table 6 P_{cwo}. Thomas et al presented SPM and DPM results for this case. Our SPM results and results using their method show about the same agreement as they reported. The two DPM methods give virtually the same transient for this case.

Fig. 30 shows that for the 30 ft. block our DPM results are slightly high and our curve using Thomas' method is higher yet.

Fig. 31 shows for the 10 ft. block and low P_c case good SPM agreement using our DPM and a low transient using Thomas' method.

For the 30 ft. block and low P_c case, Fig. 32 shows good accuracy of our DPM and a significantly more rapid transient using Thomas' method.

For both 10 ft. and 30 ft. block heights, the low P_c case required a β_w value of 2.7 while the higher Table 6 P_c case required no change from the default 1.0 value. This reflects our experience that imbibition-dominated (high P_c) cases generally require no adjustment of β_w.

Figs. 31 and 32 show fair preservation of accuracy of DPM results using the same 2.7 β_w value with a 3-fold change in block height.

If matrix block height is significantly less than grid block height, then a plot of $(S_{wm} - S_{wc})/((S_{wf} * (S_{we} - S_{wc}))$ for the partial immersion calculation should give a transient curve independent of S_{wf}. Fig. 33 shows SPM and DPM results for S_{wf} = .5 and 1.0 for the 10 ft. block and Table 6 P_c. The curves are nearly independent of S_{wf} value.

Three-Dimensional Waterflood Example

Results are compared to those of Thomas et al for their line drive water injection example. Their 10 x 3 x 5 grid describes a 2000 x 2000 x 250 ft. reservoir with water injection and total liquid production rates specified at x = 0 and x = 2000 ft., respectively. P_c and k_r data and fluid properties at 6215 psia formation pressure are given in Table 6. Matrix blocks are 10 ft. cubes. The remaining data are not reproduced here.

Each layer of this grid is 50 ft. thick and contains a stack of five matrix blocks. Fig. 29 shows that both Thomas' and our DPM methods give good agreement with full immersion SPM results for water imbibition into a single 10 ft. matrix block. However, Fig. 34 shows the different grid block equilibrium curves for the two methods. Equating the VE (pseudo) matrix and fracture capillary pressure curves for various S_{wf} values gives the two solid curves shown on Fig. 34. The upper curve is obtained by applying this procedure for a single 10 ft. matrix block and represents Thomas' method. The step-function curve is the correct result obtained by applying the procedure on the basis of the 50-ft. grid block height. The dashed line is the relationship used in our method if S^*_{wf} = 0.

The expected impact of the differences in these equilibrium curves on 3D results is difficult to deduce. Confusion arises in trying to reconcile the curve differences with factors such as (a) the magnitude of the imbibition transient time (Fig. 29, about 1 year) compared with flood displacement times, (b) the time a grid block spends in a partial immersion state, compared with imbibition transient time, and others. If a problem were designed where a dominant aspect of reservoir behavior was a long-term or stabilized establishment of partial fracture saturation (say, .5), then reasoning alone might deduce from Fig. 34 that calculated recovery would be significantly higher for Thomas' method than ours. In any event, it seems safe to infer from Fig. 34 that Thomas' results might reflect faster early imbibition leading to lower WOR and higher recovery. However, all blocks eventually experience permanent S_{wf} values of 1.0 at which recoveries for both methods are identical.

Fig. 35 compares the two methods on the basis of water cut calculated from the 3D simulations. The methods give very similar results. Our water cut is higher early and lower at late times. Thomas reported breakthrough at about 1.5 years, and water cut and recovery values at 10 years of 92% and 35 % OOIP, respectively. Our breakthrough time is about 1 year and 10-year water cut and recovery are 88.4% and 34.6% OOIP, respectively.

Our run was made using an initial 5-day step with automatic step selection limited only by a specified maximum step size and a maximum increase of 50% from step to step. For a maximum step of .5 years, the run required 27 steps and 63 iterations for the 10 years. A maximum step of .25 years resulted in 45 steps and 91 iterations. Time truncation error is small as the faster run gave 10-year water cut and recovery values of 87.4% and 34.4 % OOIP. Results were insensitive to whether the VE P_c option was used for the interblock fracture flow.

Five-Spot Waterflood

Kazemi et al presented data and results for an 8x8x1 areal grid simulation of a waterflood in a five-spot quadrant. Their results were closely reproduced by Thomas et al. The data are in Table 4. Matrix block dimensions are 10x10x30 ft. and reservoir thickness is 30 ft. Therefore matrix block height equals grid block thickness and there are no horizontal fractures.

Several purposes are served in connection with this example. First, the DPM is evaluated in the case where its accuracy is least - the case of n = 1 or equal matrix block and grid block heights. Second, an equivalent line-drive waterflood case is defined. The interwell distance, total volume and rates are the same as in the five-spot quadrant. The correct line drive results can be obtained from a three-dimensional SPM grid. Therefore, the DPM results are compared to correct results, not just to those of another model.

The comparison between line-drive DPM and correct (SPM) results is extended to the case of formation thickness = 90 ft. where $n = \Delta z/h = 3$, a case where DPM accuracy would be expected to be greater. Finally, the areal 8 x 8 x 1 DPM five-spot results are presented with an estimate of the correct five-spot results provided by the DPM-SPM line drive comparisons.

Our calculations utilize data differing from Kazemi et al in the following respects. Our injection and production rates are 200 RB/d. With their data in parentheses, shape factor is .16 (.08) and fracture k_r and P_c are linear (non-linear) and zero (non-zero), respectively. The extended time period of 3200 (1200) days allows more meaningful comparisons. From the data, we calculate effective fracture permeabilities of 50 and 100 md in the x and z directions, respectively. Thomas et al used an effective value of 500 md. The effect on WOR and oil recovery of effective fracture permeability values over this range is essentially absent and isotropic values of 100 and 500 md are used here for line drive and five-spot runs, respectively. In the 3D SPM grids described below for the line drive, wells were completed in all layers and a PI of about .06 RB-cp/day-psi per ft. of completion was used. Results are unaffected by PI values ranging from this level to 100 times larger.

The five-spot quadrant is 600 ft. on each side. The equivalent line drive element having the same interwell distance and total volume is 848.5 ft. long, 424.24 ft. wide and 30 ft. thick. To account for dual porosity, an 8 x 2 x 10 3D single-porosity grid is used with $\Delta z = 3$ ft. The two adjoining 8 x 10 cross-sections, denoted by subscripts j=1 and j=2, represent fractures and matrix, respectively. For the given fracture and matrix porosities of .01 and .19,

$$\Delta y_1 = 4.2425 \text{ ft.} \qquad \phi_1 = 1. \tag{68}$$

$$\Delta y_2 = 420 \text{ ft.} \qquad \phi_2 = .19(.99) = .1881$$

The proper value of k_y for y-direction (matrix-fracture) flow is calculated as follows. A single 10 x 10 x 30 ft. matrix block has a total lateral transmissibility across its four vertical faces of

$$\tau = 2k\left(\frac{\ell_y h}{\ell_x/4} + \frac{\ell_y h}{\ell_x/4}\right) = 16\,kh \tag{69}$$

In a grid block of dimensions $\Delta x \Delta y \Delta z$ there are

$$\Delta x\, \Delta y\, \Delta z(1 - \phi_f) / \ell_x\, \ell_y\, h \tag{70}$$

of these matrix blocks. In the 8 x 2 x 10 grid the y-direction transmissibility between two grid blocks is therefore

$$\tau_y = k_{y2}\,\frac{\Delta x\, \Delta z}{\Delta y_2/2} = 16kh\,\frac{\Delta x\, \Delta y\, \Delta z(1 - \phi_f)}{\ell_x\, \ell_y\, h} \tag{71}$$

where Δy is the total 424.24 ft., Δy_2 is 420 ft., and k_{y2} is the y-direction permeability assigned to the matrix segment j=2. The value of k_{y1} for the fracture segment is infinity. Eqn. (71) gives

$$k_{y2} = \frac{8\,\Delta y_2\,\Delta y}{\ell_x\,\ell_y}\,k = 14254.5 \text{ md} \tag{72}$$

for the data of this example problem. The fracture permeability is $k_{x1} = k_{z1} = 10000$ md; the matrix permeability of 1 md gives $k_{z2} = 1$ md, and $k_{x2} = 0$. This 3D SPM grid represents a fractured formation with a normal set of both x-z and y-z vertical fractures. The DPM equivalent grid is 8 x 1 x 1. Both grids represent a line-drive or one-dimensional flood.

The 8 x 2 x 10 grid represents the matrix-fracture flow using a single grid point or grid block for the 10 x 10 ft. xy area of the matrix block. This representation is exactly equivalent to a 2 x 2 x 10 3D grid representation of a (symmetrical) quadrant of a single matrix block with its associated vertical fractures. Thus we can assess the accuracy of the 8 x 2 x 10 field-scale simulation results by performing immersion runs for 1/4 element of a single block using a 2 x 1 x 10 xz grid with x-direction transmissibilities multiplied by two.

Fig. 36 compares the single-block, water imbibition (immersion) curve calculated using a (1/4 element) fine grid of 5 x 5 x 10 and the 2 x 1 x 10 grid. The latter grid gives a transient curve somewhat low. However, increasing the matrix permeability by 20% gives a 2 x 1 x 10 grid result virtually identical to the correct curve, as shown in Fig. 36. Therefore, $k_{y2} = 1.2 \times 14254.5 = 17105.4$ md was used in the 8 x 2 x 10 field-scale SPM grid. The 5 x 5 x 10 fine grid used Δx and Δy spacings from fracture to block center of ε, .3, .7, 1.5, 2.5 ft. and vertical spacing of $\Delta z = 3$ ft. Both grids used $k_{rwf} = .2$ at $S_{wf} = 1$ for flow into the matrix.

Also shown on Fig. 36 are the single-block immersion results using our DPM and Thomas' method. The latter method's use of VE capillary pressures as driving force gives an excessively rapid transient for the 30-ft. block height. Our DPM results are somewhat low but compare well with the correct SPM results. The DPM runs use the 1 md matrix permeability value.

The implication here is that SPM-DPM agreement for the single matrix block full immersion case ensures accuracy of the field-scale SPM 8 x 2 x 10 simulation. One might object that the full immersion comparison is inconclusive since all grid (matrix) blocks in the field simulation experience various states of partial immersion. We therefore repeated the single matrix block 5 x 5 x 10 and 2 x 1 x 10 (with k_m x 1.2) runs for the partial immersion case $S_{wf} = .2$. The following results indicate that the full immersion accuracy is retained under partial immersion conditions.

Time	S_{wm} ($S_{wf} = .2$)	
Days	5 x 5 x 10	2 x 1 x 10
100	.2997	.2970
600	.3610	.3607
1200	.3944	.3953
2400	.4326	.4361
3200	.4493	.4539

Fig. 37 shows the grid block equilibrium curves for the cases here of n = 1 and 3. The upper curve is correct for the case n = 1 and is obtained as discussed previously. Thomas' method reflects this (upper) curve in the matrix-fracture driving force expression for any value of n. The correct curve for the case n = 3 is shown by the step-function solid curve of Fig. 37. The DPM curves (Eqn. (34)) are shown by the dashed lines for S^*_{wf} = 0, .0856 and .314. We used S^*_{wf} = .314 and .0856 for the cases n = 1 and n = 3, respectively. This reduces the DPM error for small n. The value of .463 for equilibrium grid block saturation at S_{wf} = 0 is the equilibrium saturation of a 30-ft. matrix block exposed to water at its bottom face.

Fig. 38 compares SPM and DPM oil recovery and water cut results for the field-scale line-drive waterflood with formation thickness = h = 30 ft. The DPM recovery is moderately high up to 1500 days and too low at larger times. The SPM and DPM recoveries are 37.9 and 39.1% OOIP, respectively, at 1200 days, and are 56.1 and 53.2% OOIP, respectively, at 3200 days. The ultimate recovery for all three calculations is 62.6% OOIP when the fractures are 100% water-filled.

The high DPMT recovery curve simply reflects the high immersion transient of Fig. 36. If the matrix permeability is reduced 65% in that run, agreement with the SPM results is much better.

For the case of reservoir thickness = 90 ft., the well rates are increased to 600 RB/d so that rate per ft. of thickness is unchanged. The SPM grid is 8 x 2 x 30 with 30 3-ft. layers and zero z-direction transmissibilities between layers 10 and 11 and between layers 20 and 21 in the matrix cross-section j = 2.

Fig. 39 compares SPM and DPM recovery and water cut results for the case where reservoir thickness = 90 ft. and n = $\Delta z/h$ = 3 for the 8 x 1 x 1 DPM calculation. The DPM results are more accurate in this case than in the previous case of n = 1. The DPMT results for this case are the same as the DPMT results for n = 1 shown on Fig. 38. The SPM and DPM recoveries are 36.1 and 36.4% OOIP, respectively, at 1200 days, and are 53 and 51.4% OOIP, respectively, at 3200 days. Recovery for this 90 ft. thickness case is roughly 2 to 3 recovery percentage points lower than for the 30 ft. thickness case.

Fig. 40 shows five-spot oil recovery and water cut DPM results calculated using the 8 x 8 x 1 areal grid and the 30-ft. reservoir thickness. We believe the correct five-spot recovery curve would compare to the DPM curve on Fig. 40 in about the same fashion as exhibited by the SPM-DPM line drive comparison of Fig. 38.

The five-spot DPM run required 28 timesteps and 34 iterations to 1200 days and 44 steps and 50 iterations to 3200 days. Material balances were .99998. Time steps ranged from the initial 2 days to 180 days. Time step controls were maximum saturation change per step of .15 and maximum step size of 180 days but both were rarely invoked. Rather, output times of every 200 days to 1200 days and every 400 days thereafter together with a maximum increase of 50% from step to step determined the time steps. Runs with various smaller maximum step sizes indicate that time truncation error is minimal.

Application to Volatile Oil Reservoir A

Reservoir A is a fractured matrix reservoir with about 16 years' history. The reservoir oil is an undersaturated volatile oil with B_o of about 2.2 RB/STB and solution gas of 1966 SCF/STB at the 5553 psia bubble point. Original reservoir pressure is about 7000 psia with a water-oil contact about 1200 feet below top of structure. The 3-component EOS representation of the oil was discussed above in connection with Figs. 1-2 and Table 2.

During the last 13 of the 16 years' history, first-stage separator gas (86% methane) was injected. When gas injection began, reservoir pressure was 6800 psia, about 1300 psi above bubble point. Reservoir pressure and oil recovery at the end of history are about 4000 psia and 12% of OOIP, respectively. GOR has risen to about 9000 Scf/STB. Questions concerning future recovery include continued separator gas injection, N_2 injection and/or water injection.

The reservoir study has proceeded far past the status described here. The original history match dataset is retained as a fixed reference for the purpose of testing model changes or enhancements. Table 9 gives some reservoir description data. Since the reservoir is highly heterogeneous, only average values are given for permeability, porosity, etc. The effective fracture permeability is the order of 100 times matrix permeability with the latter averaging about .5 md with variations to much lower values.

Of interest are the small matrix block size (prolific fracturing) on the order of 1x1x3 ft., and the low fracture porosity averaging .0005 or less. A consequence of the first is a large matrix-fracture exchange coefficient the order of 10^7 (RB-cp/day-psi). The low fracture porosity gives small fracture-system pore volumes and high throughput ratios for large time steps. This requires implicit model simulation. The large transfer coefficients result in computational difficulty since the matrix-fracture darcy flow rates are the products of large coefficients and small potential differences (.01 to .001 and lower psi). This combination can cause round-off and computational convergence difficulties, especially for large time steps and large, rapidly changing injection/production rates.

Figs. 41 and 42 show total field oil production rate and gas injection rate vs time as 91-day averages. The rates change every 91 days throughout the dataset, giving a maximum 91-day step size. Fig. 42 shows the extreme variations in gas injection rate from one 91-day period to the next. About 6 of the 47 wells are gas injection wells; only one well injects water, during the last 270 days of history. The gas injection rate changes might be expected to result in oscillating fracture oil saturations from step to step, especially at or near injection and/or production wells. Fig. 43 shows calculated fracture oil saturation vs time in a grid block adjacent to a high-rate injector. Calculated oil saturation is virtually monotonic with time in spite of large injection rate changes.

The S_{ge} value is important in this study. Its internally-calculated value changes with time and from block to block. History runs were made for the three cases of constant S_{ge} (with spatial variation), density-dependent S_{ge}, and density- and tension-dependent S_{ge}. Runs were also made with and without diffusion. The original S_{ge} values are about .4-.5 for block heights in the range of 3 to 4 ft. The model history runs show calculated grid block matrix saturations in close agreement with the S_{gf} x S_{ge} product, reflecting the large matrix-fracture transmissibilities. Two exceptions occur. First, for rock type 2, S_{wc} is large, oil saturation is low and oil easily becomes immobile due to trapping by gas and water in accordance with the Stone 2 k_{ro} method. Thus a number of the type 2

blocks show matrix gas saturation < $S_{gf} \times S_{ge}$ simply because the matrix oil is immobile and cannot drain out. The second exception is that grid block equilibrium occurs at some pressure, followed by significant pressure decline. Oil does not want to (and does not in the calculations) drain out of the block to matrix oil saturations below equilibrium values but the oil shrinks in accordance with the constant-volume expansion. Also, depending upon the nature of injected gas, oil can vaporize, further reducing its saturation or, equivalently, increasing matrix gas saturation above its equilibrium value.

Fig. 44 compares field total observed and model GOR vs time. The model results reflect diffusion and density-and tension-dependent S_{ge}. Calculated GOR is avout 9400 Scf/STB at the end of history. Without diffusion, calculated GOR is about 14% higher. For the time-constant S_{ge} case, calculated GOR is 7700 Scf/STB at the end of history. S_{ge} and diffusion are the controlling parameters in the calculated GOR behavoir. Runs with depth-dependent initial composition (bubble point decreasing with depth) show significantly lower GOR.

Fig. 45 indicates the strong diffusion effect when injected and native reservoir gas compositions differ significantly. Restart runs were made from the time-constant S_{ge} case, injecting N_2 rather than separator gas during the 3472-5753 (end of history) day period, with and without diffusion. Fig. 45 shows that calculated GOR is extremely higher without diffusion than with it. Table 10 shows the effect of diffusion on matrix-fracture oil and gas phase composition for this N_2 injection case in a grid block adjacent to a gas injector. Without diffusion, virtually no N_2 appears in the matrix phases and large composition differences exist between matrix and fracture phase compositions. With diffusion (only gas-gas diffusion was used), matrix and fracture phase compositions are identical, both in the gas and oil.

Table 11 shows calculated matrix and fracture gas saturations at the end of history for the constant S_{ge} run with diffusion. Saturations are shown for several cells, including active and shut-in gas injection blocks. As stated above, equilibrium matrix gas saturation is $S_{gf} \times S_{ge}$. Table 11 shows that the calculated matrix gas saturations are close to equilibrium, due to the large matrix-fracture exchange coefficients. Table 11 shows a matrix gas saturation exceeding S_{ge} for the active gas injection block 4-8-1. This reflects the vaporizing effect of the separator gas, reducing matrix oil saturation to less than its equilibrium value.

In all model runs no computed matrix oil saturations less than .2 were computed. That is, complete vaporization of oil did not occur in any case/block. In fact, the minimum matrix oil saturations over the grid were close to .2 both for N_2 and separator gas injection cases. These minimums occured in gas injection cells and matrix oil saturations were significantly higher throughout the non-injection cells, obeying the equilibrium relationship.

Maximum gas production rates (QGMAX) were entered in the data file for all producing wells. They were obtained from the history file as the maximum gas MCF/D rates produced throughout history. The model produces the specified STB/d oil rate for each well unless the associated gas rate exceeds the well's entered QGMAX. In the latter event, the well produces the QGMAX gas rate. The overall impact of this is noted by printing total cumulative shortage of oil produced (STB) divided by total specified cumulative oil production. This fraction is .0145 for the run shown in Fig. 44.

The 5753-day history run required 60 time steps and 167 total outer iterations, an average of about 3 outer iterations per 91-day time step. 91-day steps were used throughout with larger, up to 200-day, steps used during the first 1280 days before gas injection began. No time-step cuts occurred and total computing time was about 2.5 VAX 780 CPU hours.

An iterative YZ planar SOR was used with resulting omega values of about 1.4 and total inner iterations at 5753 days of about 1700, or an average of 10 SOR iterations per outer iteration. The linear solver takes about 20% of total computing time. All component material balances were the order of .999X to .9999X throughout the runs with the "sensitive" normal denominator basis of cumulative injection or production.

Computer time with 4 components ($3+N_2$) active is about 60% greater than that for 3 components. All runs were made with a 4-component set of PVT data entered with N_2 the last component. Since initial N_2 mol fraction is 0, the model automatically computes with only 3 components until the first time step (if any) of N_2 injection. It then automatically expands to the 4-component calculation. This can save considerable computing expense in problems where certain components(s) are absent initially and throughout part or all of history but become active due to later injection.

Summary

An implicit compositional model has been described for compositional simulation of single- or dual-porosity reservoirs. The model simulates unsteady-state three-dimensional, three phase flow in heterogeneous reservoirs ranging in type from black oil to near-critical oil or gas to lean gas condensate. Applications include depletion and gas and/or water injection. Single-porosity applications incur no loss of efficiency caused by the presence of dual-porosity code. The code is mapped so that storage is required only for active grid blocks. This can significantly reduce machine storage requirements for reservoirs having highly irregular geometry. Dual-porosity applications include regionally fractured reservoirs where unfractured single-porosity regions exist.

Advantages of 3-component compositional as opposed to extended black oil modelling are described and illustrated for an actual near-critical volatile oil reservoir. A simple method for reducing time truncation error in implicit formulations is described and illustrated. A new bottomhole constraint function is presented for preservation of production well target rates in compositional models.

A new matrix-fracture transfer formulation is described for the dual-porosity case. Matrix block size and shape may vary from block to block over the grid. The formulation accounts for matrix-fracture diffusion and effects of changing gas-oil density difference and interfacial tension on gravity drainage recovery. The approximate accuracy of the formulation is shown for a number of test problems where correct results are available from single-porosity simulation. Results are given for a 3D 600-block simulation of a highly fractured near-critical volatile oil reservoir.

Nomenclature

B	Formation volume factor, RB/STB
b	1/B
b_{ij}	EOS binary interaction coefficients

c_r	Matrix rock compressibility, 1/psi
c_f	Fracture compressibility, 1/psi
c	Fluid compressibility, 1/psi
D	Diffusion coefficient, cm^2/sec
GOC	Gas-oil contact depth, ft.
h	Matrix block height, ft.
i, j, k	Grid block indices in x, y, z directions
k	Permeability, md
k_r	Relative permeability
K	K-value, $K_i = y_i/x_i$
ℓ_x, ℓ_y, ℓ_z	Matrix block dimensions, ft.
n	Number of matrix blocks in stack within one grid block
N_c	Number of hydrocarbon components
N_x, N_y, N_z	Numbers of grid blocks in x, y, z directions
p	Pressure, psia
Δp	$P_{om} - P_{of}$
P_c	Capillary pressure, psi
P_{ce}	Threshold gas-oil capillary pressure
PI	Well productivity index, RB-cp/d-psi
P_j	Compositional model variables
q	Flow rate
S	Saturation, fraction
S_{wc}	Connate water saturation
S_{orw}	Residual oil saturation to water
S_{org}	Residual oil saturation to gas
S_w^o	Matrix water saturation at imbibition $P_{cwo} = 0$
S_{we}, S_{ge}	Matrix block equilibrium water and gas saturations
S^*_{we}, S^*_{ge}	Grid block equilibrium matrix water and gas saturations
S^*_{wf}	Fracture water saturation displacement
T	Temperature, ^oF
V	Bulk reservoir volume, cu. ft.
WOC	Water-oil contact depth, ft.
x, y, z	Cartesian coordinates
$\Delta x, \Delta y, \Delta z$	Grid block dimensions, ft.
x_i	Mol fraction of component i in oil phase
y_i	Mol fraction of component i in gas phase
z_i	Wellstream composition
Z	Depth, measured vertically downward, ft. or fluid supercompressibility factor

Greek

β_w, β_g	Dual-porosity model gravity drainage parameters
γ	Fluid specific weight, psi/ft.
λ	Phase mobility, k_r/μ
μ	Phase viscosity, cp
Ω_a, Ω_b	EOS parameters
ϕ	Porosity, fraction
ρ	Phase molar density, mols/volume
σ	Shape factor, $1/ft^2$, or interfacial tension, dynes/cm
σ^o	Initial interfacial tension
σ_r	Interfacial tension ratio, σ/σ^o
τ	Matrix-fracture transmissibility, RB-cp/d-psi
τ_z	Matrix-fracture drainage transmissibility, $k_z \ell_x \ell_y / \ell_z$, RB-cp/d-psi
T	Interblock transmissibility, RB-cp/d-psi
τ_{or}	Tortuosity

Subscripts

f	Fracture
go	Gas-oil
i	Initial
ℓ	(superscript) outer iteration number
m	Matrix
n	Time level
w,o,g	Water, oil, gas
wo	Water-oil
x,y,z	x,y,z directions

Acknowledgment

The author acknowledges the extensive assistance of C. A. Ellis in connection with model code and documentation and of M. A. Martinez and C. A. Ellis in preparation of this paper.

References

1. Coats, K. H.: "Simulation of Gas Condensate Reservoir Performance," J. Pet. Tech. (Oct. 1985) 1870-86.

2. Redlich, O, and Kwong, J.N.S.: "On the Thermodynamics of Solution V. An Equation of State, Fugacities of Gaseous Solution," Chem. Review (1949) 44, 233.

3. Soave, G.: "Equilibrium Constants From a Modified Redlich-Kwong Equation of State," Chem. Eng. Sci., (1972) 27, 1197-1203.

4. Zudkevitch, D. and Joffe, J.: "Correlation and Predictions of Vapor-Liquid Equilibria with the Redlich-Kwong Equation of State," AIChE J. (Jan 1970) 16, 112-19.

5. Joffe, J., Schroeder, O.M., and Zudkevitch, D.: "Vapor-Liquid Equilibria with the Redlich-Kwong Equation of State, "AIChE J. (May 1970) 16, 496-98.

6. Peng, D. Y. and Robinson, D.B.: "A New Two-Constant Equation of State," Ind. Eng. Chem. Fundam. (1976) 15, 59.

7. Coats, K.H. and Smart, G.T.: "Application of a Regression-Based EOS PVT Program to Laboratory Data," SPE Res. Engr. (May 1986) 277-299.

8. Lohrenz, J., Bray, B.G., and Clark, C.R.: "Calculating Viscosities of Reservoir Fluids From their Compositions," J. Pet. Tech. (Oct. 1964) 1171-76; Trans., AIME, 231.

9. Reid, R. C. and Sherwood, T. K.: "The Properties of Gases and Liquids," third edition, McGraw-Hill Book Co. Inc., New York City (1977).

10. Coats, K.H., Nielsen, R.L., Terhune, M.H. and Weber, A.G.: "Simulation of Three-Dimensional, Two-Phase Flow in Oil and Gas Reservoirs," Soc. Pet. Eng. J. (Dec. 1967) 377-88.

11. Marathon Oil Company, Littleton, Colo., Personal Communication, 1985

12. da Silva, F. and Belery, P.: Personal Communication, Petrofina, Brussels, 1987.

13. Price, H.S. and K.H. Coats, "Direct Methods in Reservoir Simulation", Soc. Pet. Eng. J. (June, 1974) 295-308.

14. Coats, K.H.: "An Equation of State Compositional Model," Soc. Pet. Eng. J. (Oct. 1980) 363-376.

15. Warren, J.E. and Root, P.J.: "The Behavior of Naturally Fractured Reservoirs," Soc. Pet. Eng. J. (Sept. 1963) 245-44; Trans., AIME, 228.

16. Kazemi, H., Merrill, L., Porterfield, K. and Zeman, P.: "Numerical Simulation of Water-Oil Flow in Naturally Fractured Reservoirs," Soc. Pet. Eng. J. (Dec. 1976) 317-326; Trans., AIME, 261.

17. Thomas, L.K., Dixon, T.N. and Pierson, R.G.: "Fractured Reservoir Simulation," Soc. Pet. Eng. J. (Feb. 1983) 42-54.

18. Gilman, J.R. and Kazemi, H.: "Improvements in Simulation of Naturally Fractured Reservoirs," Soc. Pet. Eng. J. (August 1983) 695-707.

19. Sonier, F., Souillard, P. and Blaskovich, F.T.: "Numerical Simulation of Naturally Fractured Reservoirs," paper SPE 15627 presented at the 1986 SPE Annual Technical Conference, New Orleans, LA, Oct. 5-8.

20. Sonier, F. and Eymard, R.: "A New Simulator for Naturally Fractured Reservoirs," paper SPE 16008 presented at the Ninth SPE Symposium on Reservoir Simulation held in San Antonio, TX., Feb. 1-4, 1987.

21. Dean, R.H. and Lo, L.L., "Simulations of Naturally Fractured Reservoirs", SPE Reservoir Engineering (May, 1988), 638-648.

22. Litvak, B.L.: "Simulation and Characterization of Naturally Fractured Reservoirs," Proceedings of the Reservoir Characterization Technical Conferences, Dallas (April 29-May 1, 1985). Academic Press, New York (1985).

23. Rossen, R.H., Shen, E.L: "Simulation of Gas/Oil Drainage and Water/Oil Imbibition in Naturally Fractured Reservoirs," paper SPE 16982 presented at the 1987 SPE Annual Technical Conference, Dallas, TX., Sept. 27-30.

24. Golf-Racht, T.D. van: Fundamentals of Fractured Reservoir Engineering, Elsevier Scientific Publishing Col, 1982.

25. Wu, Yu-Shu and Karsten Preuss, "A Multiple-Porosity Method for Simulation of Naturally Fractured Petroleum Reservoirs", SPE Reservoir Engineering (Feb., 1988) 327-336.

26. Kleppe, J. and Morse, R.A.: "Oil Production from Fractured Reservoirs by Water Displacement," paper SPE 5084 presented at the 1974 SPE Annual Technical Conference, Houston, TX., Oct. 6-9.

27. Beckner, B.L., Ishimoto, K., Yamaguchi, S., Firoozabadi, A., Aziz, K.: "Imbibition-Dominated Matrix-Fracture Fluid Transfer in Dual Porosity Simulators," paper SPE 16981 presented at the 1987 SPE Annual Technical Conference, Dallas, TX., Sept. 27-30.

28. Lefevbre du Prey, E.J., "Cascade drainage of blocks in a fissured reservoir," Revue de l'institut Francais du petrole, Janv.-Fev. (1976), p. 173-178.

29. Festoey, S., Van Golf-Racht, T.D.: "Gas Gravity Drainage in Fractured Reservoirs Through New Dual Continuum Approach", paper SPE 16980, presented at the 1987 SPE Annual Technical Conference, Dallas, TX., Sept. 27-30.

30. Thomas, L.K., Firoozabadi, A.: "Tenth SPE Symposium on Reservoir Simulation Dual Porosity Comparative Solution Project," to be presented at the 1989 SPE Symposium on Reservoir Simulation, Houston, TX., Feb. 6-8.

31. Saidi, A.M. and Tehrani, D.H.: "Mathematical Simulation of Fractured Reservoir Performance, Based on Physical Model Experiments," Paper PD10(3) on the Developments in Reservoir Engineering, Proceedings of the 10th World Petroleum Congress, Bucharest, 1979.

Appendix A

For quasi-steady-state (QSS), single-phase, matrix-fracture flow in a bulk volume element V of reservoir, the flow rate is

$$q = -V\phi c \frac{\partial \bar{p}}{\partial t} \qquad (A1)$$

where ϕc is effective porosity-compressibility of the matrix in V. In the diffusivity equation

$$k_x \frac{\partial^2 p}{\partial x^2} + k_y \frac{\partial^2 p}{\partial y^2} + k_z \frac{\partial^2 p}{\partial z^2} = \mu \phi c \frac{\partial p}{\partial t} \qquad (A2)$$

$\partial p/\partial t$ is independent of position within the matrix for QSS flow so that substitution from Eqn. (A1) gives

$$k_x \frac{\partial^2 p}{\partial x^2} + k_y \frac{\partial^2 p}{\partial y^2} + k_z \frac{\partial^2 p}{\partial z^2} + \frac{q\mu}{V} = 0 \qquad (A3)$$

where V is the matrix block volume. If the matrix block has dimensions a, b, c in the x, y, z directions, respectively, then Eqn. (A3) can be written

$$\frac{\partial^2 p}{\partial x_D^2} + r\frac{\partial^2 p}{\partial y_D^2} + s\frac{\partial^2 p}{\partial z_D^2} + Q = 0 \qquad (A4)$$

where

$$x_D = x/a \qquad y_D = y/b \qquad z_D = z/c$$

$$r = \frac{k_y}{k_x}\frac{a^2}{b^2} \qquad s = \frac{k_z}{k_x}\frac{a^2}{c^2} \qquad Q = \frac{q\mu a^2}{k_x V} \tag{A5}$$

Eqn. (A4) can be solved for p using the Fourier finite sine transform and the result integrated to obtain

$$\bar{p}_m - p_f = Q\,8^3 \sum_i \sum_j \sum_k \frac{1}{\lambda_i^2 \beta_j^2 \gamma_k^2 (\lambda_i^2 + r\beta_j^2 + s\gamma_k^2)} \tag{A6}$$

The term $\bar{p}_m$ is volumetric average matrix block pressure and each summation is over odd, positive integers only, and

$$\lambda_i = i\pi \qquad \beta_j = j\pi \qquad \gamma_k = k\pi \tag{A7}$$

Rearrangement gives

$$\frac{q\mu}{k_x V(\bar{p}_m - p_f)} = \frac{1}{8^3 \Sigma\Sigma\Sigma}\frac{1}{a^2} \tag{A8}$$

where $\Sigma\Sigma\Sigma$ denotes the triple summation of Eqn. (A6).

For the two-dimensional x-y case (no horizontal fractures, N=2), the corresponding result is

$$\frac{q\mu}{k_x V(\bar{p}_m - p_f)} = \frac{1}{8^2 \sum_i \sum_j \frac{1}{\lambda_i^2 \beta_j^2 (\lambda_i^2 + r\beta_j^2)}}\frac{1}{a^2} \tag{A9}$$

and for the one-dimensional case (vertical fractures normal to the x-axis, N=1),

$$\frac{q\mu}{k_x V(\bar{p}_m - p_f)} = \frac{1}{8\sum_i \frac{1}{\lambda_i^4}}\frac{1}{a^2} \tag{A10}$$

where, again, each summation is only over odd, positive integers.

Warren and Root defined their shape factor by

$$\sigma = \frac{q\mu}{kV(\bar{p}_m - p_f)} \tag{A11}$$

where

$$\sigma = 4N(N+2)/\ell^2, \tag{A12}$$

ℓ is a representative matrix block dimension, and N is the number of normal sets of fractures, N=1, 2 or 3. Kazemi et al suggested the shape factor

$$\sigma = 4\left(\frac{1}{a^2} + \frac{1}{b^2} + \frac{1}{c^2}\right) \tag{A13}$$

and here we use

$$\sigma = 8\left(\frac{1}{a^2} + \frac{1}{b^2} + \frac{1}{c^2}\right) \tag{A14}$$

A tabular comparison of σ values for the isotropic case a=b=c for N=1, 2 and 3 from the analytical Eqns. (A8)-(A10) and Eqns. (A13) and (A14) is given below Eqn. (23). The sums in Eqns. (A8)-(A10) can be calculated to give σ values for any anisotropy and any set of unequal matrix block dimensions. Warren and Root give expressions for ℓ in terms of unequal a, b, c values for the cases N=1, 2, and 3.

The transient time associated with single-phase matrix-fracture flow can be examined by solving Eqn. (A2) for initial condition $p = p_i$ and boundary conditions $p = p_f$ on all matrix block faces (where p here is matrix pressure). The solution for volumetric-average matrix pressure is

$$\frac{\bar{p}_m - p_f}{p_i - p_f} = 8^3 \sum_i \sum_j \sum_k e^{-(\lambda_i^2 + r\beta_j^2 + s\gamma_k^2)t_D} \frac{1}{\lambda_i^2 \beta_j^2 \gamma_k^2} \tag{A15}$$

Where t_D is $kt/\mu\phi\, ca^2$ and sums are over odd positive integers. For the isotropic, cubic block case this ratio is about .03 at $t_D = .1$ and for $t_D > .1$ the ratio is approximated by the first term of the summation,

$$\frac{\bar{p}_m - p_f}{p_i - p_f} \simeq \frac{8^3}{\pi^6} e^{-3\pi^2 t_D} \tag{A16}$$

Thus a 90+ % decay occurs at $t_D = .1$ or

$$t = \frac{.1\mu\phi c\ell^2}{.00633\,k} \tag{A17}$$

where units are cp, psi^{-1}, ft and md for μ, c, ℓ and k, respectively. For many fractured reservoirs, this decay time is very small, the order of .01 days or less.

TABLE 1

DIFFUSION (MATRIX-FRACTURE)

$$J_{GG}\ \frac{\text{Mole}}{\text{Day}} = \frac{A\phi}{L}\ \frac{S_{GG}\ D_{GG}}{\tau_{or}}\ (C_{G1} - C_{G2})$$

$$J_{LG} = \frac{A\phi}{L}\ \frac{S_{LG}\ D_{LG}}{\tau_{or}}\ (C_{L1} - C_{G2})$$

$$C_L = \rho_L x \qquad C_G = \rho_G y$$

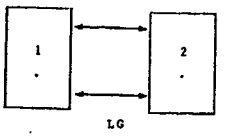

EQUILIBRIUM DILEMMA:

$C_{G1} = C_{G2}$
$C_{L1} = C_{G2}$
$C_{L1} = C_{G1}$
$\rho_{L1} x_i = \rho_{G1} y_i$
$y_i/x_i = K_i = \rho_{L1}/\rho_{G1}$, all i

EACH CELL
2-PHASE GAS-OIL

TABLE 2

VOLATILE OIL RESERVOIR A FLUID COMPOSITIONS AND DATA

T = 266° F

	RESERVOIR FLUID			INJECTION GAS	
	10-CPT	3-CPT		3-CPT	10-CPT
C1	.5898	.5898	PC 1	.8601	.8601
CO2	.0093	.1926	PC 2	.1343	.0113
C2	.0757	.2176	PC 3	.0056	.0775
C3	.0409				.0283
C4	.0300				.0115
C5	.0192				.0039
C6	.0175				.0017
F7	.07812				.0053
F8	.09517	Y_{c7^+} = .8578			.0003
F9	.04431				.0000

		EOS	
	DATA	10-CPT	3-CPT
BUBBLE PT.	5553.7	5553.7	5553.7
ρ_o at B.P.	36.11	36.11	36.11 lbs/cu.ft
σ at B.P.			.2716 dynes/cm

3-CPT EOS B.P. RESULTS

	OIL x_i	GAS y_i	K_i
PC1	.5898	.7966	.13507
PC2	.1926	.1670	.8670
PC3	.2176	.0364	.1672
ΔY_{go}	.1124psi/ft		

3 - STAGE SURFACE SEPARATION

STAGE	P, psia	T, °F
1	1014.7	150
2	264.7	80
3	14.7	60

	DATA	10-CPT	3-CPT
STAGE 1 GOR[1]	1057	1057	1057
STAGE 1 Y_G	.6910	.6819	.6708
STAGE 3 Y_L	.8363	.8363	.8324
GOR[2]	1489	1510	1489
B_o	1.8530	1.8530	1.8530

1) SCF Stage 1 Gas/BBL stage 1 liquid
2) Total SCF/STB

TABLE 3

EFFECT OF ROCK VS. VERTICAL-EQUILIBRIUM CAPILLARY PRESSURE CURVES ON CALCULATED INITIAL FLUIDS IN-PLACE

400 FT. VERTICAL COLUMN

GOC = 85 ft. WOC = 285 ft.
$P_{cwo} = 30(1-S_w)^3$ $P_{cwo} = 108\frac{3}{g}$
ΔY_{wo} = .1662 ΔY_{go} = .1181 psi/ft.

INITIAL FLUIDS-IN-PLACE, 1000'S RB

	VE P_c			ROCK P_c		
N_E	WATER	OIL	FREE GAS	WATER	OIL	FREE GAS
1	2747.1	3319	1224.4	1423	5947	0
2	2747.1	3319	1224.4	3518	3727	0
5	2747.1	3319	1224.4	2625	3441	1233
10	2747.1	3319	1224.4	2757	3326	1207
20	2747.9	3319	1224.3	2771	3323	1196

TABLE 4

KAZEMI ET AL FIVE-SPOT EXAMPLE DATA

Reservoir pressure	3959.89 psia
Compressibility of rock, fracture, and water	3.0×10^{-6} 1/psi
Oil compressibility	10^{-5} 1/psi
At reservoir pressure:	
Water viscosity	.5 cp
Oil viscosity	2 cp
B_w	.98812 RB/STB
B_o	.9604 RB/STB
Water Density	.4444 psi/ft.
Oil density	.3611 psi/ft.
Matrix permeability	1 md
Matrix porosity	.19
Shape Factor	.08
Matrix block size	10 x 10 x 30 ft.
Fracture permeability	10000 md
Fracture porosity	.01
Grid	8 x 8 x 1
$\Delta x = \Delta y$	75 ft.
Δz	30 ft.
Water injection rate	200 STB/d
Total liquid production rate	210 STB/d

Matrix k_r and P_c data [17]

S_w	k_{rw}	k_{ro}	P_{cwo}
.25	0	.92	4
.3	.02	.705	2.95
.4	.055	.42	1.65
.5	.1	.24	.85
.6	.145	.11	.3
.7	.2	0	0

TABLE 5

KLEPPE AND MORSE EXPERIMENTAL DATA

Matrix permeability	290 md
Matrix porosity	.225
Core diameter	9.87 cm
Inside diameter of tube	10.39 cm
Core height	122.8 cm
Water density	1.02 g/cc
Oil density	.811 g/cc
Water viscosity	1 cp
Oil viscosity	2.3 cp
Pore volume of core	2114 cc
Volume of fracture	1017 cc
Low injection rate	3.3 cc/min
High injection rate	35 cc/min

k_r and P_c data [27]

S_w	k_{rw}	k_{ro}	P_{cwo}
.3	0	.75	3.1
.352	.0005	.675	2.3
.35	.001	.605	1.83
.375	.0015	.535	1.52
.4	.002	.47	1.29
.425	.003	.4	1.08
.45	.004	.33	.94
.475	.007	.27	.82
.5	.01	.19	.7
.525	.015	.12	.61
.55	.027	.06	.52

TABLE 6

THOMAS ET AL SINGLE-BLOCK DATA

Compressibility of rock, fracture, and water	3.5×10^{-6} 1/psi
Matrix block dimensions, ℓ_x, ℓ_y, ℓ_z	1 ft. or 10 ft.
Permeability, k_x, k_y, k_z	1 md. ϕ_m = .3
Bubble-point pressure	5560 psia
Gas-oil density difference at 5560 psia	.1477 psi/ft.
Water density at 6215 psia	.431 psi/ft.
Oil density at 6215 psia	.2544 psi/ft.
Oil viscosity at 6215 psia	.2213 cp
Water viscosity	.35 cp
Oil density at 5560 psia	.25075 psi/ft.
Gas density at 5560 psia	.10307 psi/ft.
Gas viscosity at 5560 psia	.0274 cp
Oil viscosity at 5560 psia	.21 cp

Matrix k_r and P_c Data:

S_w	k_{rw}	k_{row}	P_{cwo}
.2	0.	1.00	50.0
.25	.005	.86	9.0
.3	.01	.723	2.0
.35	.02	.6	.5
.4	.03	.492	0.0
.45	.045	.392	-.4
.5	.06	.304	-1.2
.6	.11	.154	-4.0
.7	.18	.042	-10.0
.75	.23	0.	-40.0
1.00	1.00	0.	-120.0

$S_{L=1-S_g}$	k_{rog}	k_{rg}	P_{cgo}
.2	0.	1.0	1.0
.45	0.	.42	.386
.5	.028	.31	.255
.6	.11	.19	.145
.7	.25	.103	.115
.8	.45	.05	.095
.9	.7	.015	.085
1.0	1.0	0.	.075

TABLE 7

GAS-OIL DATA FOR 1x1x4 FT. MATRIX BLOCK

Rock compressibility	5.5×10^{-6} 1/psi
Fracture compressibility	5.5×10^{-6} 1/psi
Water compressibility	3×10^{-6} 1/psi
Permeability, k_x, k_y, k_z	1 md
Matrix block dimensions, ℓ_x, ℓ_y, ℓ_z	1 ft. 4 ft.
Matrix porosity	.3
Effective fracture permeability	40 md
Fracture porosity	.002
Initial pressure	5553.7 psia
Initial matrix saturations:	
Oil	.9
Water	.1
Gas	0
Gas-oil density difference at 5553.7 psia	.1181 psi/ft
S_{ge} at 5553.7 psia	.5722
Diffusion tortuosity	3.5
Grid	12 x 1 x 5
Δx	100 ft.
Δy	500 ft.
Δz	50 ft.

Drainage

$S_L=1-S_g$	k_{rog}	k_{rg}	P_{cgo}
0.10000	0.00000	1.00000	0.729
0.20000	0.00000	0.74494	0.512
0.30000	0.00000	0.53351	0.343
0.35385	0.02133	0.43675	0.2698
0.40769	0.06034	0.35137	0.2078
0.46154	0.11086	0.27687	0.1561
0.51538	0.17068	0.21276	0.1138
0.56923	0.23853	0.15849	0.0799
0.62308	0.31355	0.11351	0.05355
0.67692	0.39512	0.07721	0.0337
0.73077	0.48275	0.04894	0.0195
0.78462	0.57603	0.02802	0.010
0.83846	0.67466	0.01365	0.004215
0.89231	0.77835	0.00495	0.001249
0.94615	0.88686	0.00088	0.000156
1.00000	1.00000	0.00000	0.0

Imbibition P_{cgoi} = .1 * Drainage P_{cgo}

Gas injection well completed in all 5 layers at I = 1.

PI per layer	1.23 RB-cp/day-psi
Injection rate	2500 MSCF/d

Injection gas composition:

	Separator Gas	N2
C1	.8621	0
C2-6	.1305	0
P7-9	.0074	0
N2	0	1.0

Production well completed in layers 4 and 5, I = 12.

PI per layer	1.23 RB-cp/day-psi
Flowing bottomhole pressure	5500 psia.

TABLE 8

MATRIX GAS SATURATION VS TIME FOR THE SPE 10 FT. BLOCK CASE

(Results plotted in Fig. 15)

Time Days	S_{gm}	Time Days	S_{gm}
0	0	300	.3173
5	.0069	400	.3690
20	.0273	500	.4020
50	.0670	600	.4243
100	.1300	800	.4531
150	.1878	1000	.4704
200	.2383	7000	.4998
250	.2817		

TABLE 9

RESERVOIR A DESCRIPTION

Rock compressibility	5.5×10^{-6} 1/psi
Water compressibility	3.0×10^{-6} 1/psi
Water viscosity	.22 cp
Initial oil viscosity	.23 cp
B_w	1.06 RB/STB
Water density	63.65 lbs/cu.ft.

Δx: 3691 2461 1640 2 * 1230 3 * 1640 2051 2461 2461 ft.

Δy: 4101 14 * 1640.4 3 * 2461 4921 ft.

Following properties vary over the 11 x 19 x 3 grid. Values given are rough averages.

Layer thickness	200, 100, 150 ft.
Structure	9500 - 11000 ft. subsea
Matrix Permeability	.5 md
Matrix porosity	.3
Matrix block size (x, y, = fracture-spacings)	1.4 x .8 x 4 ft
Effective fracture permeability	50 md
Fracture porosity	.0005
Calculated matrix-fracture exchange coefficient	5×10^{7} RB-cp/day psi
Initial pressure at 10509 ft.	7000 psia
WOC	10650 ft.
OOIP	4.3×10^{-9} STB

TABLE 10

EFFECT OF DIFFUSION ON MATRIX-FRACTURE COMPOSITIONS

Time = 5753 Days (End Of History)
N2 Injected 3472 - 5753 Days
Cell 3 - 8 - 1

			No Diffusion		Diffusion	
		Cpt	Matrix	Fracture	Matrix	Fracture
OIL	x	C1	.4424	.0805	.2899	.2897
	x	N2	.0032	.2496	.1306	.1307
GAS	y	C1	.8208	.1769	.5570	.5567
	y	N2	.0071	.7846	.3178	.3181

TABLE 11

GAS SATURATIONS AT 5753 DAYS

CELL	S_{gf}	S_{ge}	S_{gm}	$S_{gf} \times S_{ge}$
2-9-1	.525	.4998	.2621	.2624
3-8-1	.8625	.4796	.4131	.4136
4-8-1(1)	1.0000	.4627	.5369	.4627
2-10-2	.239	.5044	.1217	.1206
7-10-2(2)	.9796	.4961	.4863	.4860

(1) Active Injector
(2) Shut-In Injector

FIGURE 1

RESERVOIR FLUID A

DIFFERENTIAL EXPANSION

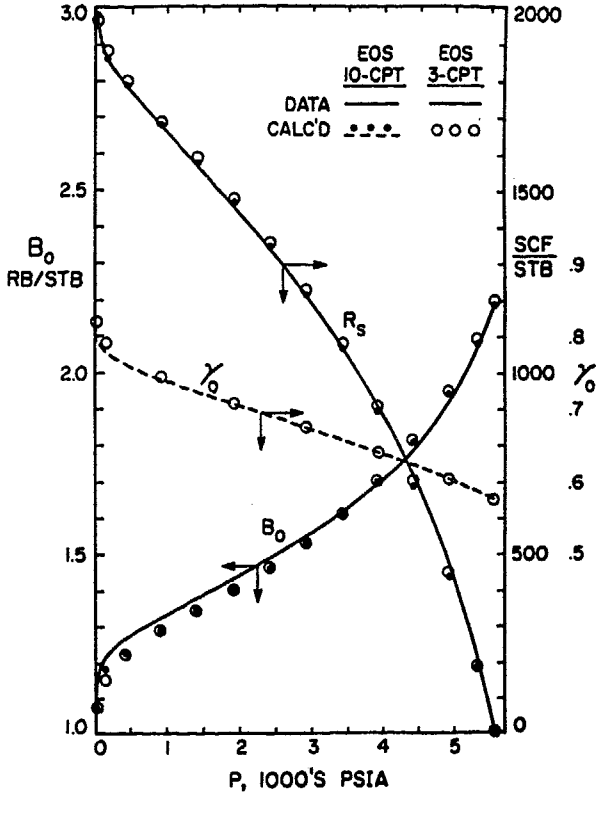

FIGURE 2

RESERVOIR FLUID A
DIFFERENTIAL EXPANSION

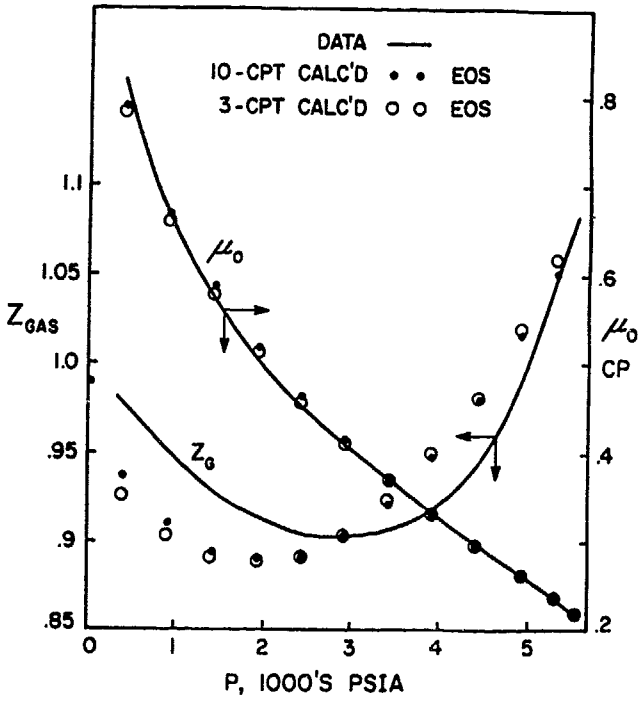

FIGURE 3

RESERVOIR FLUID A
MULTIPLE-CONTACT VAPORIZATION

EOS CALCULATED RESULTS
4415 PSIA 266 °F

10-CPT ——
3-CPT o o

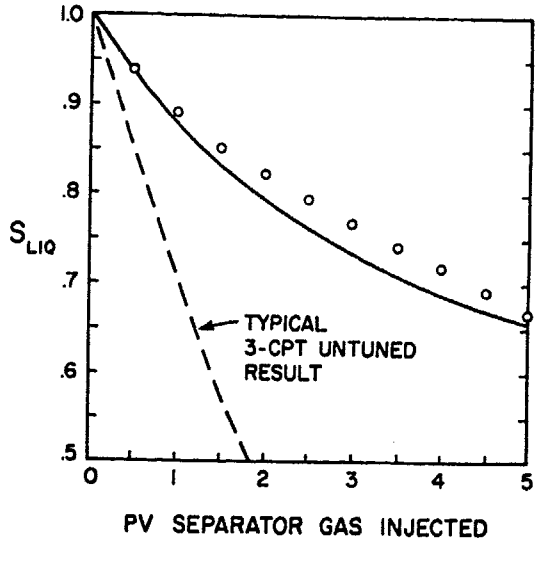

FIGURE 4

TIME TRUNCATION ERROR
IN 4380-DAY RUNS

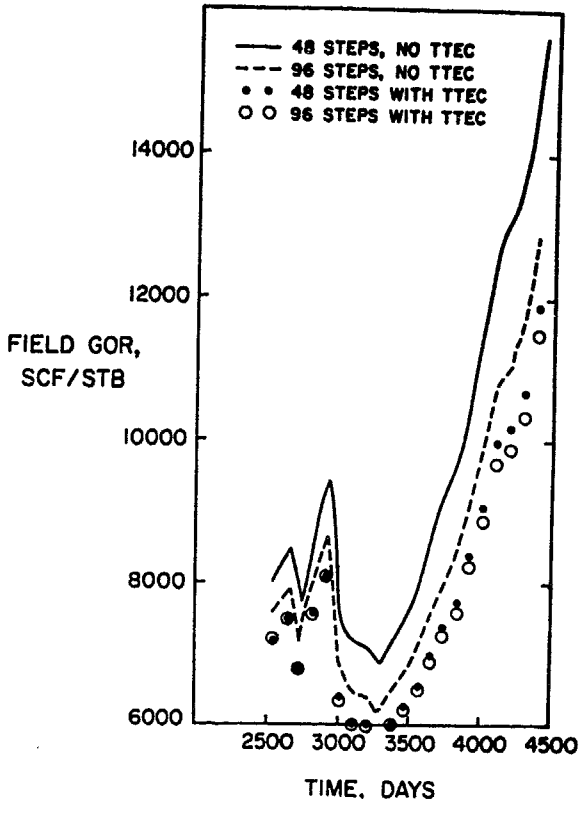

FIGURE 5

GAS-OIL GRAVITY DRAINAGE

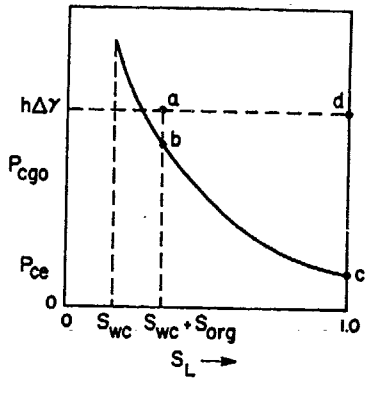

5a

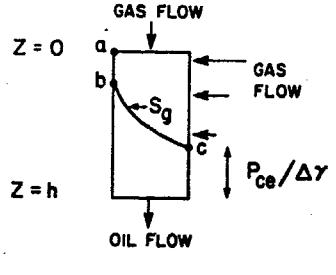

5b

FIGURE 6

WATER-OIL CAPILLARY PRESSURE CURVES

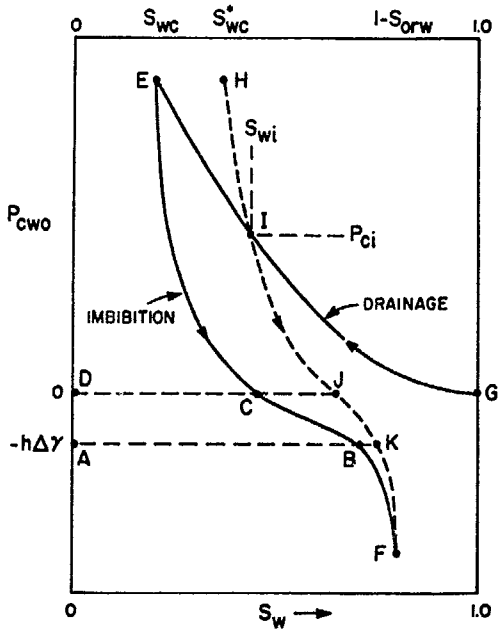

FIGURE 8

WATER IMMERSION CURVE, 10x10x30 FT. BLOCK

KAZEMI ET AL TABLE 4 DATA

(P_c=0.)

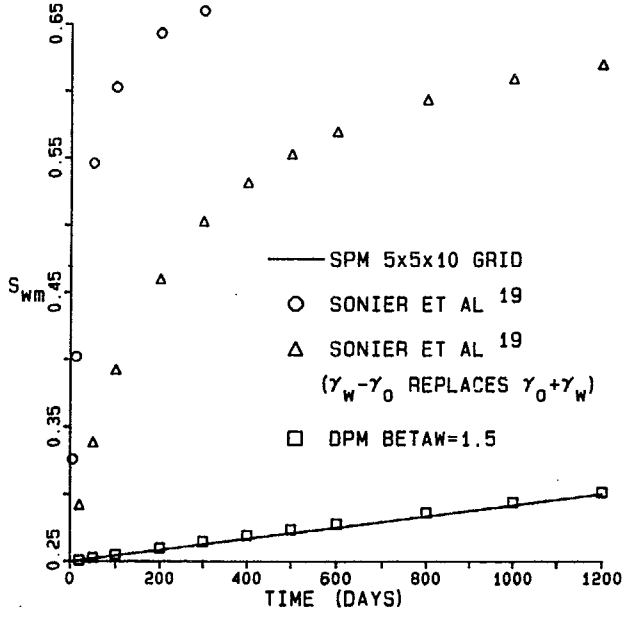

FIGURE 7

GRID BLOCK IN INITIAL

WATER-OIL TRANSITION ZONE

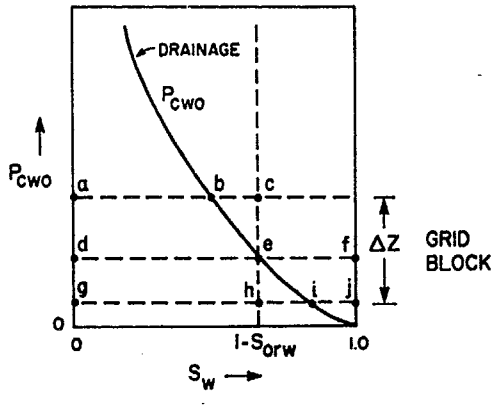

FIGURE 9

WATER IMBIBITION CURVE, 10x10x30 FT. BLOCK

k_m=.1 md TABLE 4 DATA

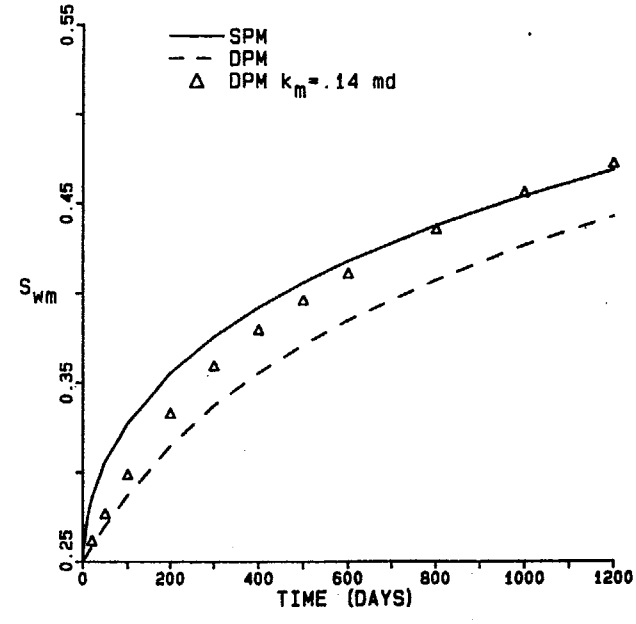

FIGURE 10

COMPARISON OF SPM AND EXPERIMENTAL RESULTS

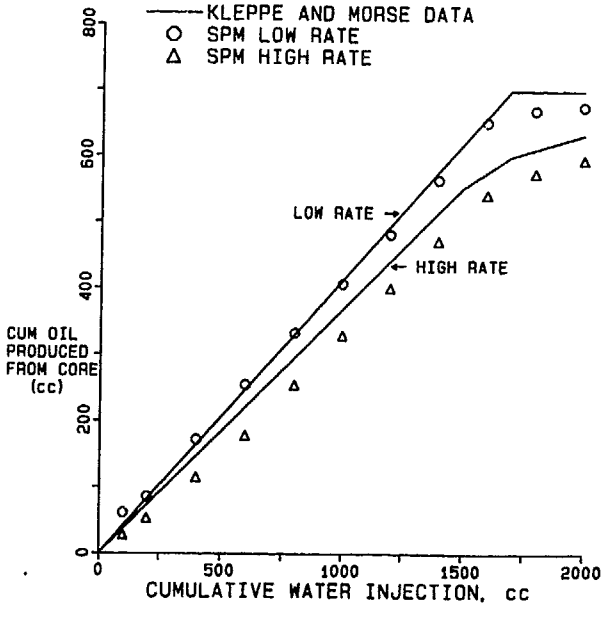

FIGURE 11

COMPARISON OF SPM AND EXPERIMENTAL RESULTS

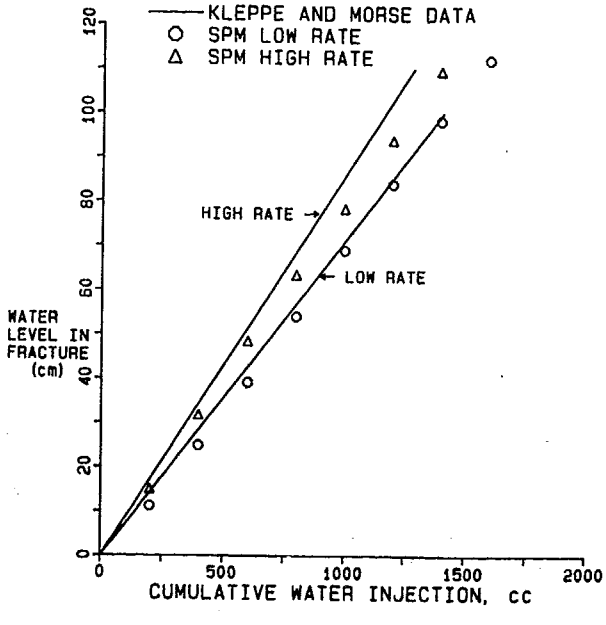

FIGURE 12

COMPARISON OF SPM AND DPM RESULTS

KLEPPE AND MORSE EXPERIMENT

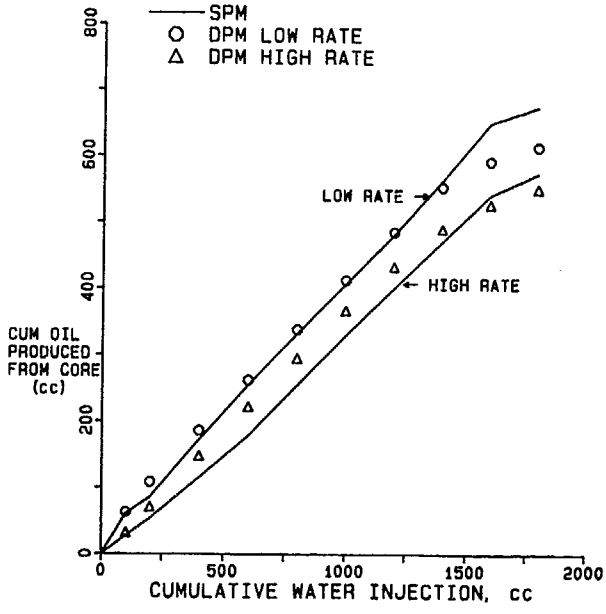

FIGURE 13

SINGLE-BLOCK AND STACK-OF-BLOCK

SPM GRIDS FOR GRAVITY DRAINAGE

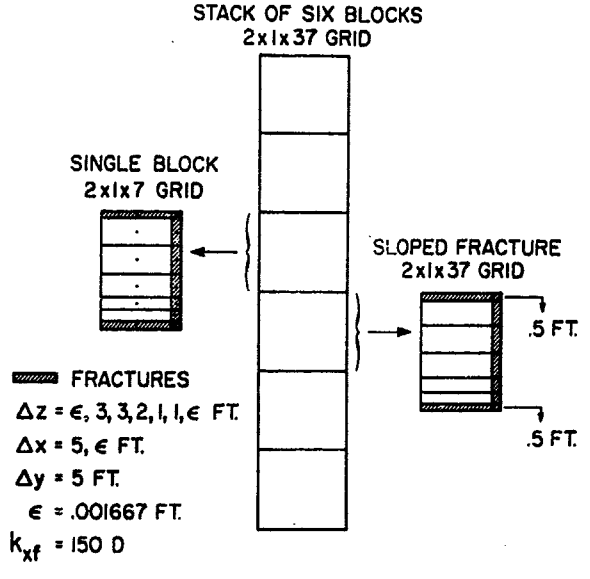

FIGURE 14

RECOVERY FOR SINGLE-BLOCK AND STACK-OF-BLOCK DRAINAGE, h=10 FT.

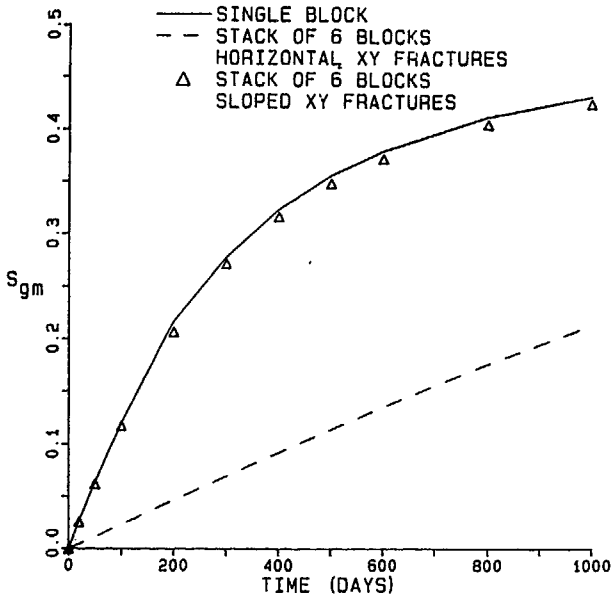

FIGURE 15

GAS/OIL DRAINAGE RECOVERY 10x10x10 FT. MATRIX BLOCK

S_{gf} = 1.0

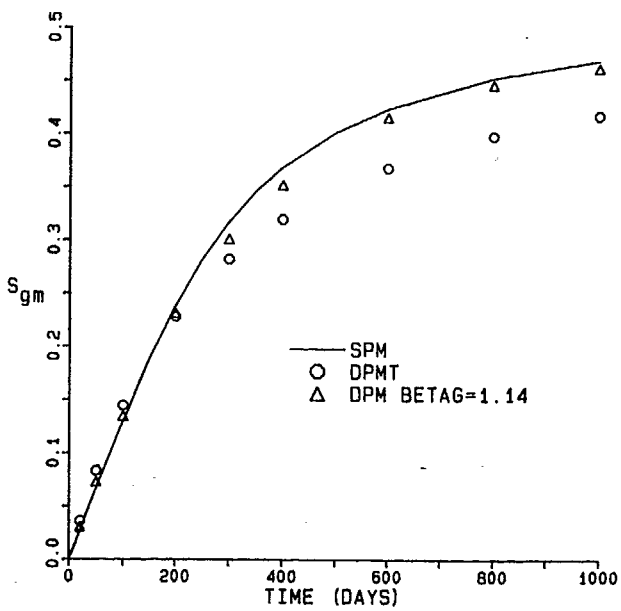

FIGURE 16

GAS/OIL DRAINAGE RECOVERY 10x10x10 FT. MATRIX BLOCK

$k_{rog}/3$

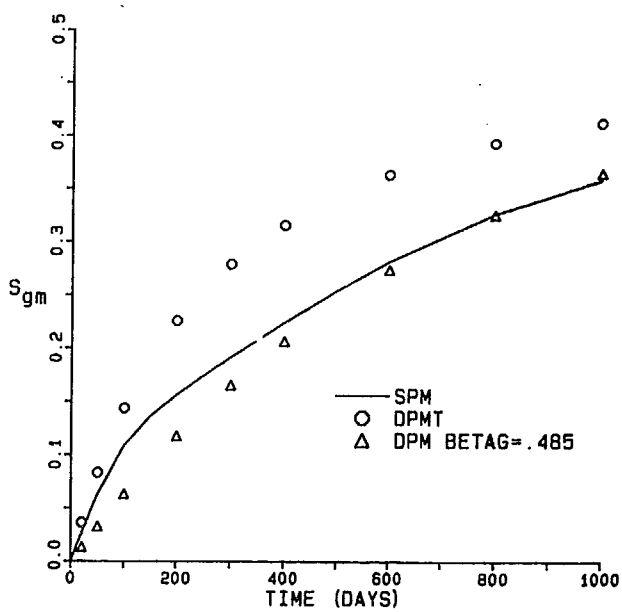

FIGURE 17

GAS/OIL DRAINAGE RECOVERY 1x1x1 FT. MATRIX BLOCK

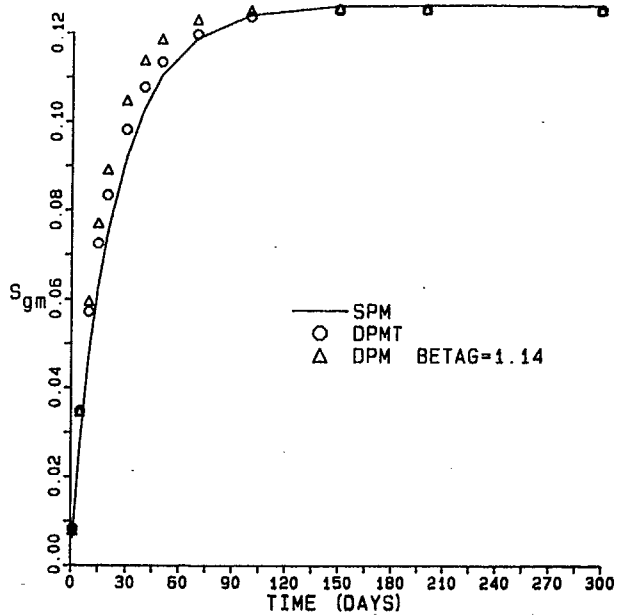

FIGURE 18
PSEUDO P_c FROM SPM GAS/OIL DRAINAGE RESULTS

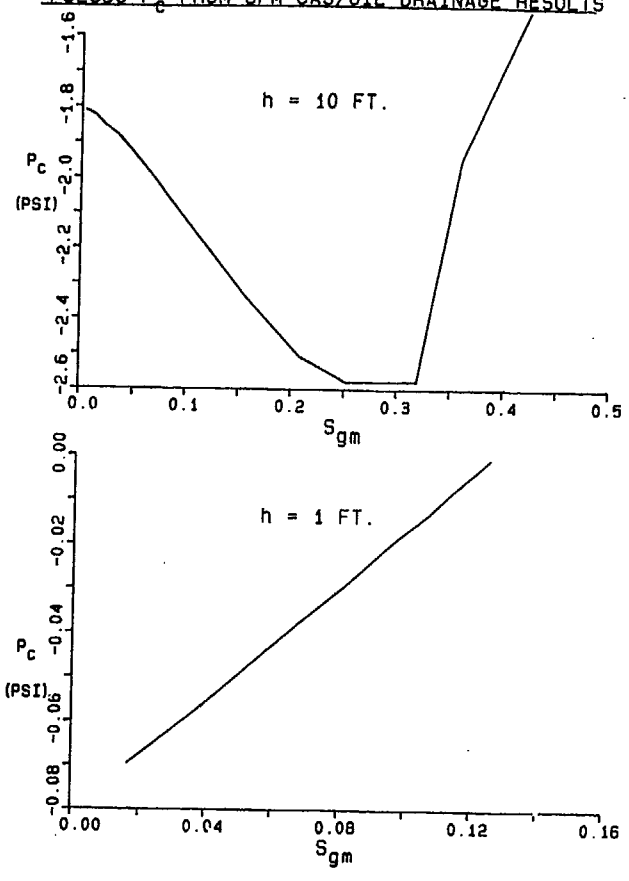

FIGURE 19

GAS/OIL GRAVITY DRAINAGE FOR A 4 FT. MATRIX BLOCK

DATA OF TABLE 7

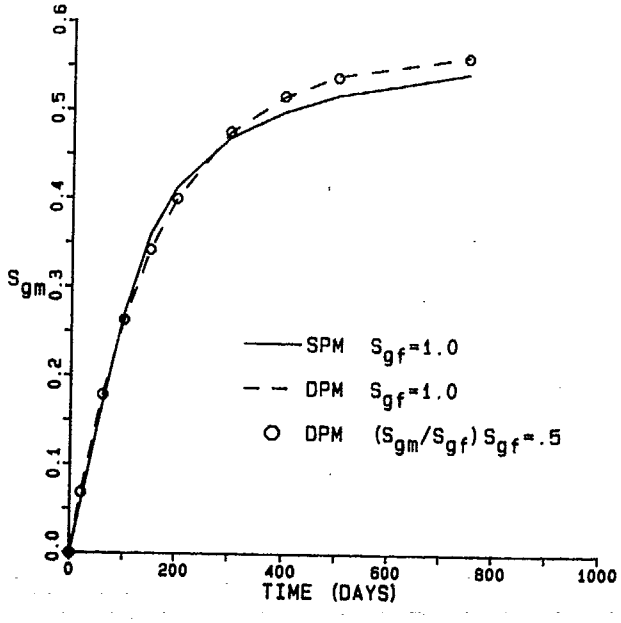

FIGURE 20

GAS/OIL GRAVITY DRAINAGE FOR A 1 FT. MATRIX BLOCK

DATA OF TABLE 7

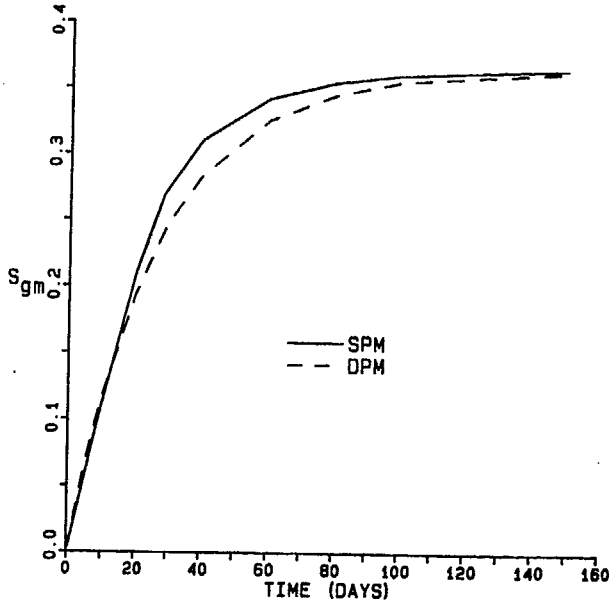

FIGURE 21
SINGLE GRID BLOCK DEPLETION

ΔZ=24 FT. h=4 FT.
S_{gf}=0.

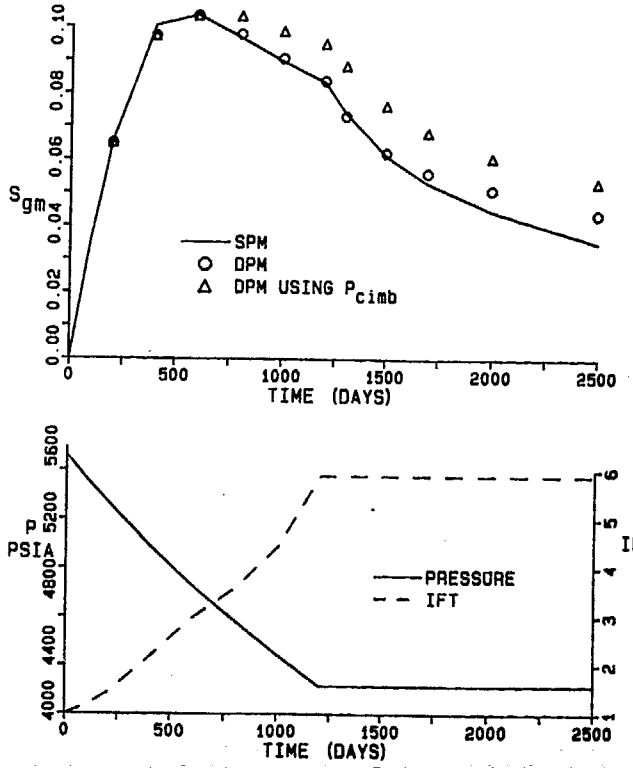

FIGURE 22

SINGLE GRID BLOCK GAS/OIL DEPLETION WITH FRACTURE GAS SATURATION > 0

ΔZ=24 FT. h=4 FT.

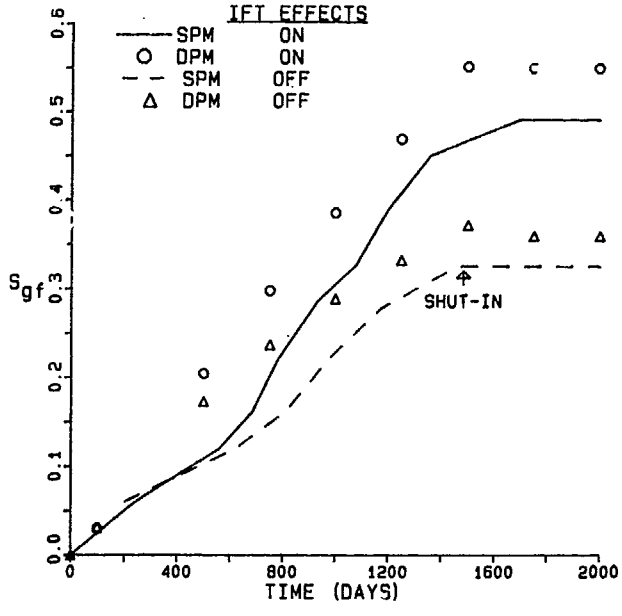

FIGURE 23

SINGLE GRID BLOCK GAS/OIL DEPLETION WITH FRACTURE GAS SATURATION > 0

P AND S_{gm} VS TIME

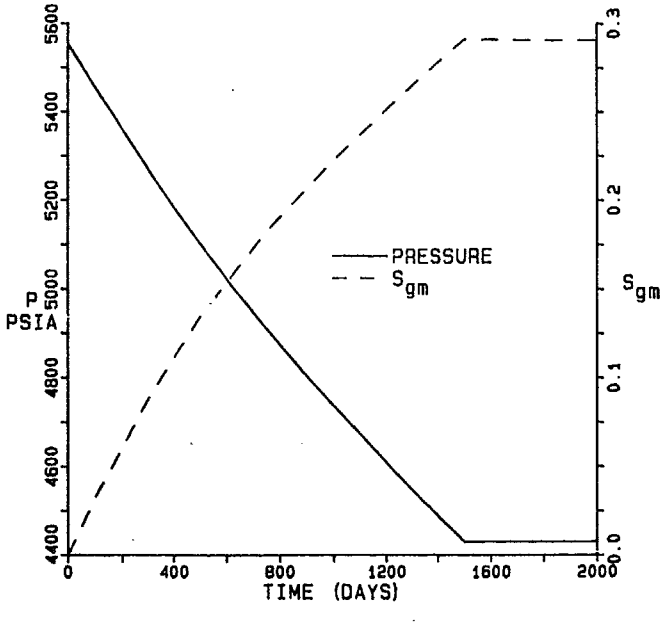

FIGURE 24

FRACTURE OIL IMBIBITION INTO 4 FT. GAS-FILLED MATRIX BLOCK

DATA OF TABLE 7
S_{gmi}=.9

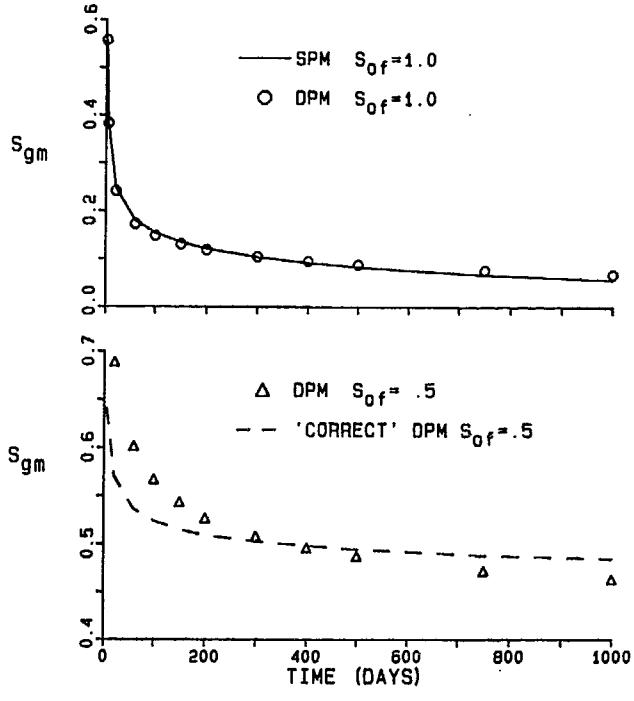

FIGURE 25

EFFECTS OF PARAMETERS ON DPM GAS/OIL DRAINAGE CURVE

4 FT. MATRIX BLOCK
DATA OF TABLE 7

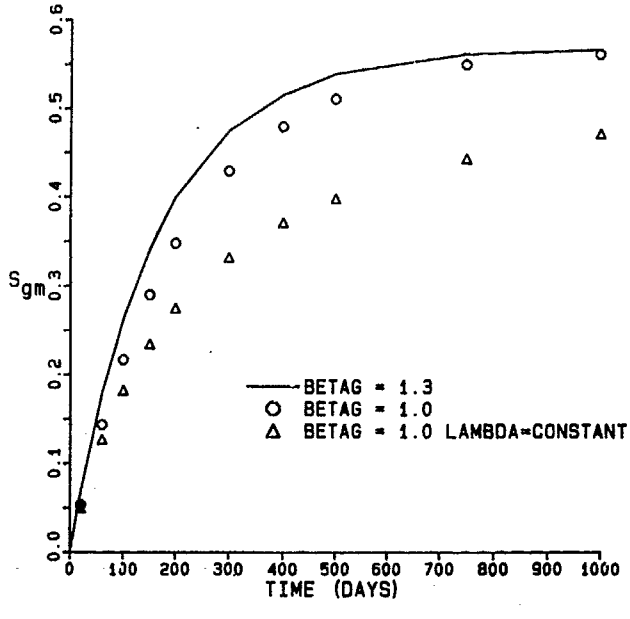

FIGURE 26

SENSITIVITY OF DPM CROSS-SECTIONAL RESULTS TO DPM PARAMETERS

CONSTANT PRESSURE SEPARATOR-GAS INJECTION DIFFUSION = 0.

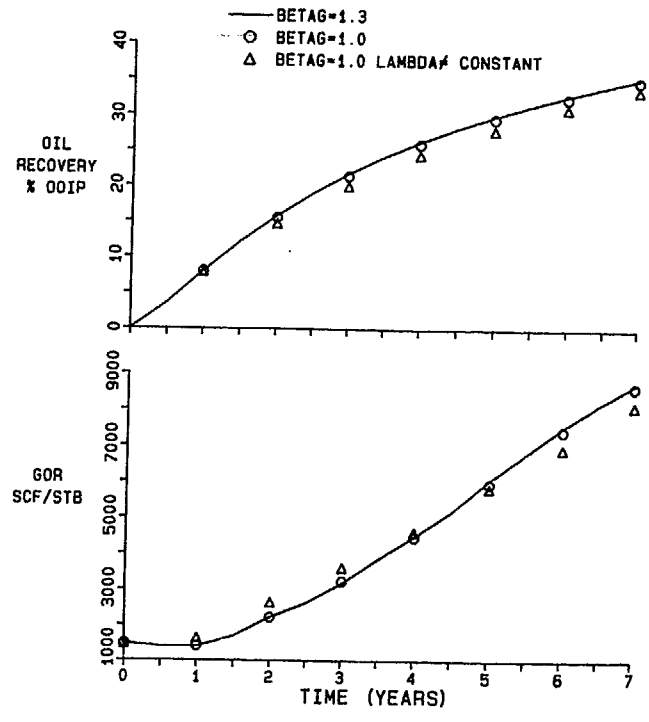

FIGURE 27

EFFECT OF DIFFUSION ON DPM CROSS-SECTIONAL RESULTS

CONSTANT PRESSURE SEPARATOR-GAS INJECTION

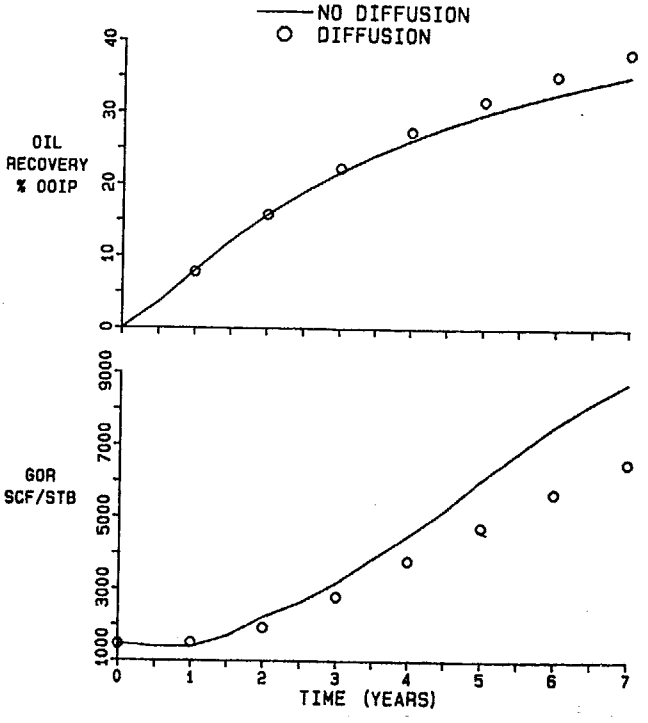

FIGURE 28

EFFECT OF DIFFUSION ON DPM CROSS-SECTIONAL RESULTS

CONSTANT PRESSURE N_2 INJECTION

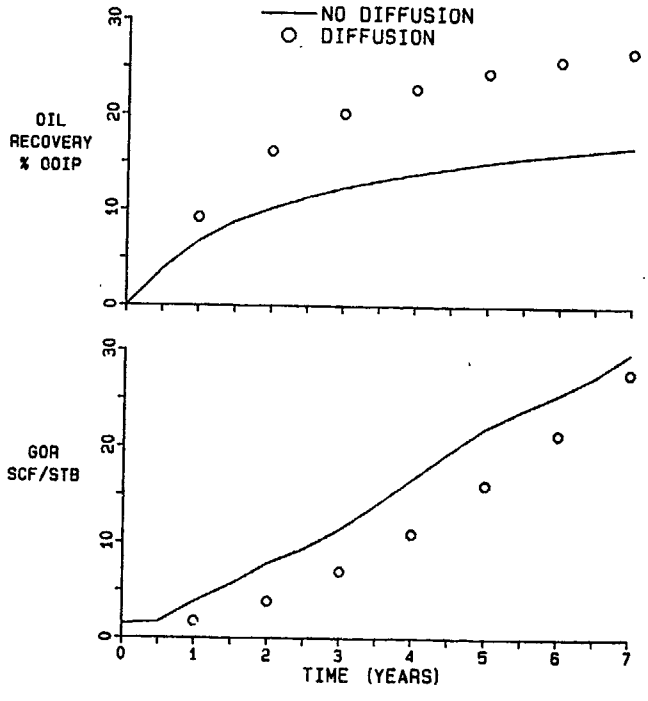

FIGURE 29

WATER IMBIBITION CURVE, 10x10x10 FT. BLOCK

P_c OF TABLE 6

S_{we}=.475

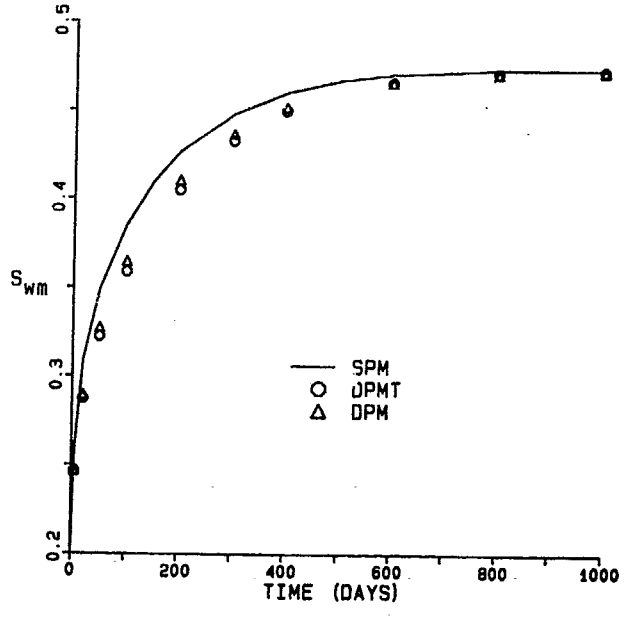

FIGURE 30

WATER IMBIBITION CURVE, 10x10x30 FT. BLOCK

P_c OF TABLE 6

S_{we}=.544

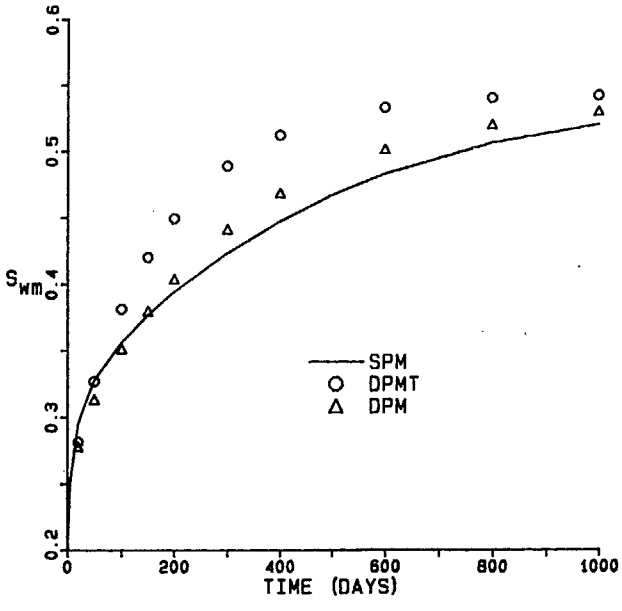

FIGURE 31

WATER IMBIBITION CURVE, 10x10x10 FT. BLOCK

LOW P_{cwo} CURVE

S_{we}=.481

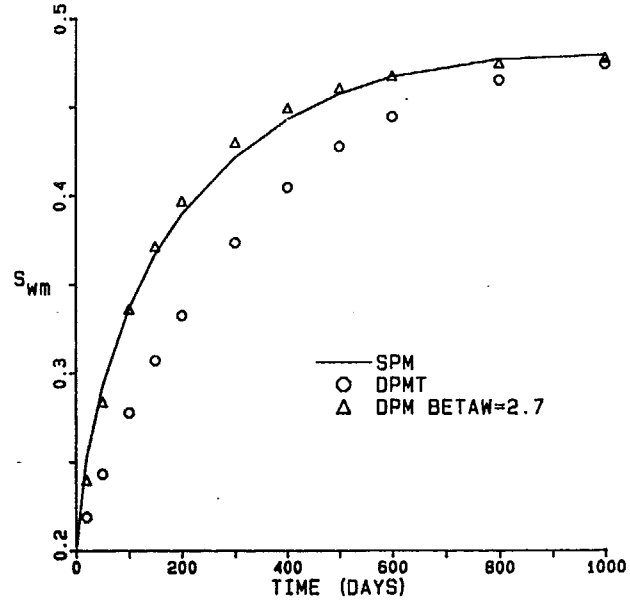

FIGURE 32

WATER IMBIBITION CURVE, 10x10x30 FT. BLOCK

LOW P_{cwo} CURVE

S_{we}=.546

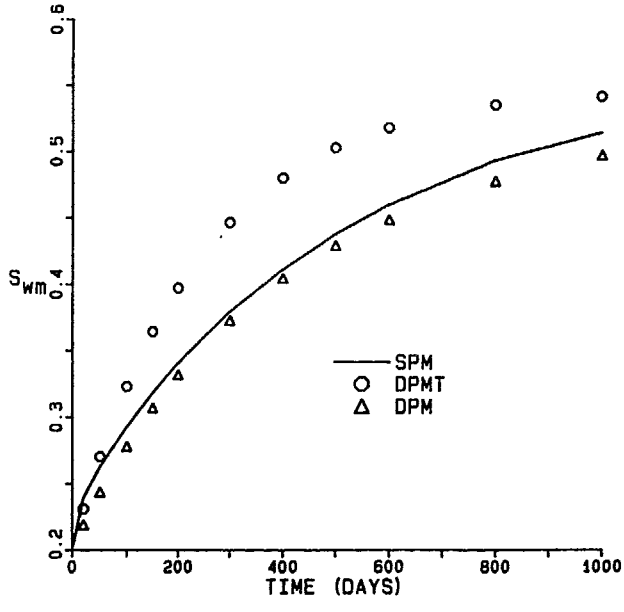

FIGURE 33

INVARIANCE TO FRACTURE WATER SATURATION OF NORMALIZED WATER IMBIBITION CURVE 10x10x10 FT. BLOCK

P_c OF TABLE 6

DPM RESULTS

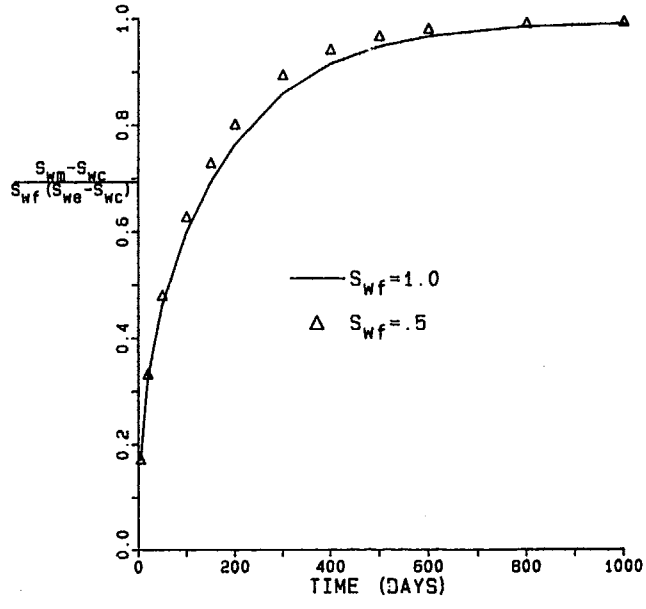

FIGURE 34

EQUILIBRIUM MATRIX WATER SATURATION VS FRACTURE WATER SATURATION

ΔZ = 50 FT. h = 10 FT.

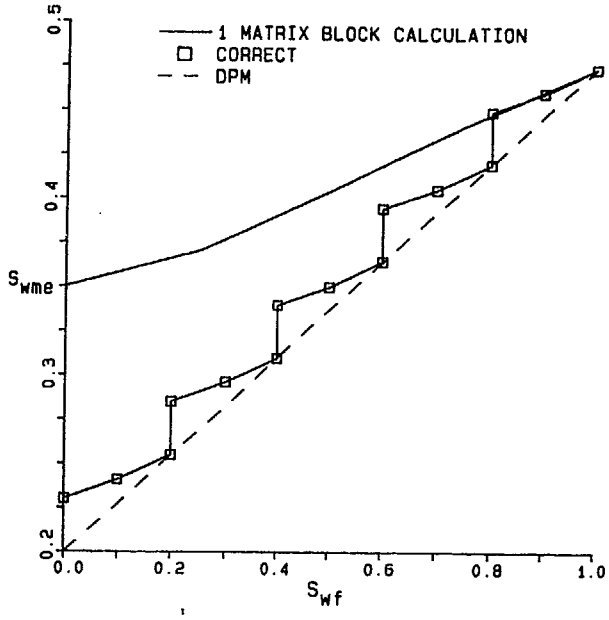

FIGURE 35

3D LINE-DRIVE WATERFLOOD EXAMPLE

DATA OF TABLE 6

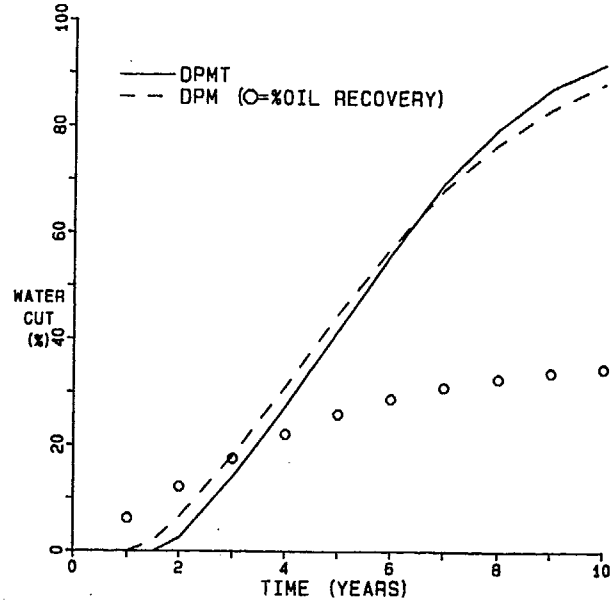

FIGURE 36

WATER IMBIBITION CURVE, 10x10x30 FT. BLOCK

DATA OF KAZEMI ET AL (TABLE 4)

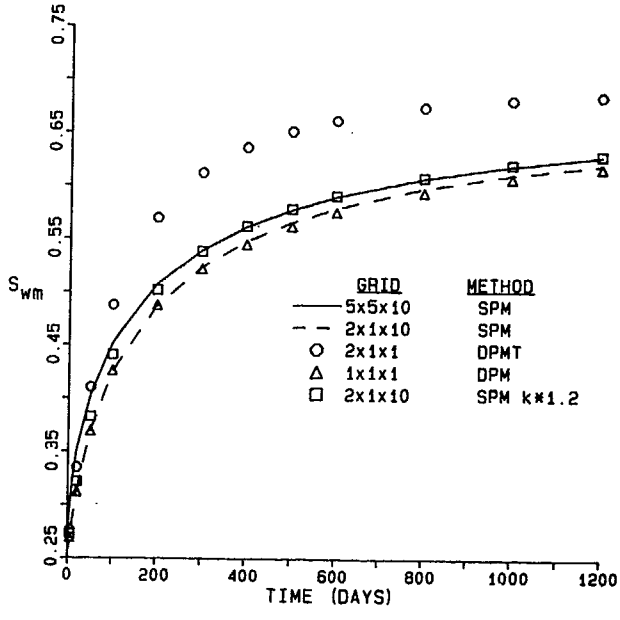

FIGURE 37

GRID BLOCK EQUILIBRIUM CURVES, h=30 FT.

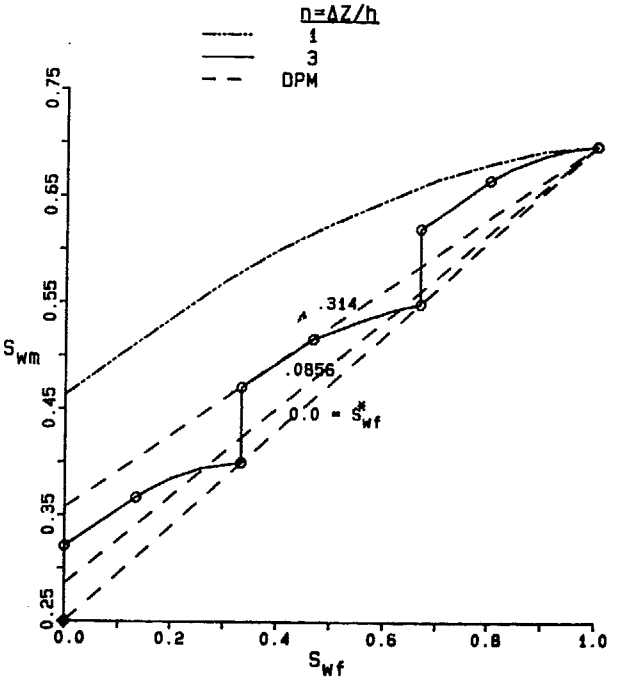

FIGURE 38

LINE-DRIVE OIL RECOVERY AND WATERCUT

ΔZ=30 FT. h=30 FT. q=200 RB/D

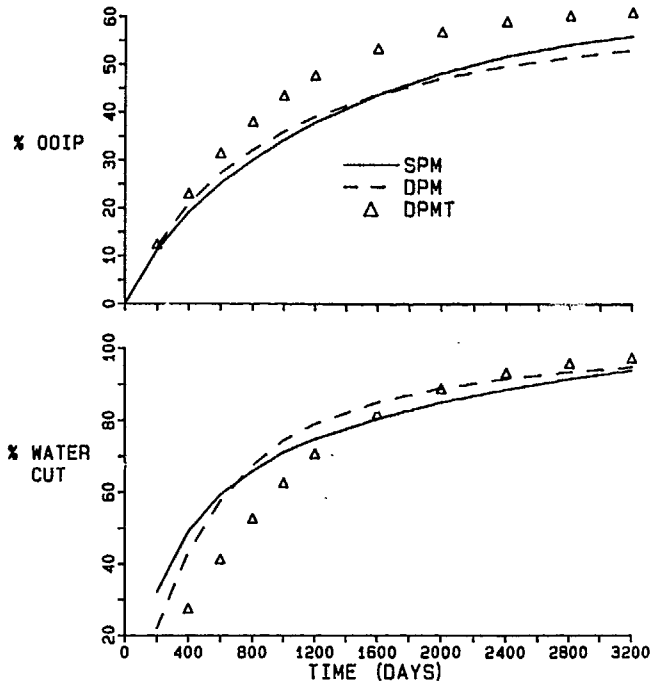

FIGURE 39

LINE-DRIVE OIL RECOVERY AND WATERCUT

ΔZ=90 FT. h=30 FT. q=600 RB/D

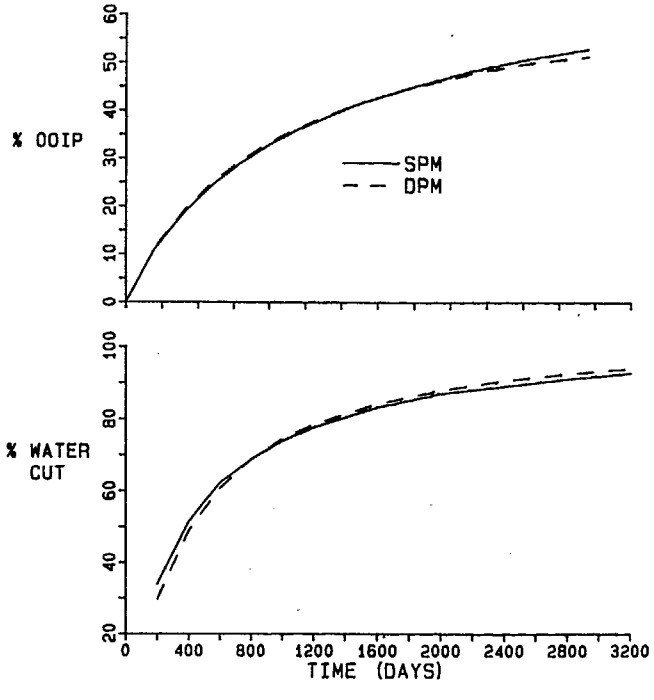

FIGURE 40

FIVE-SPOT OIL RECOVERY AND WATERCUT

8x8x1 GRID
RESERVOIR THICKNESS = 30 FT.

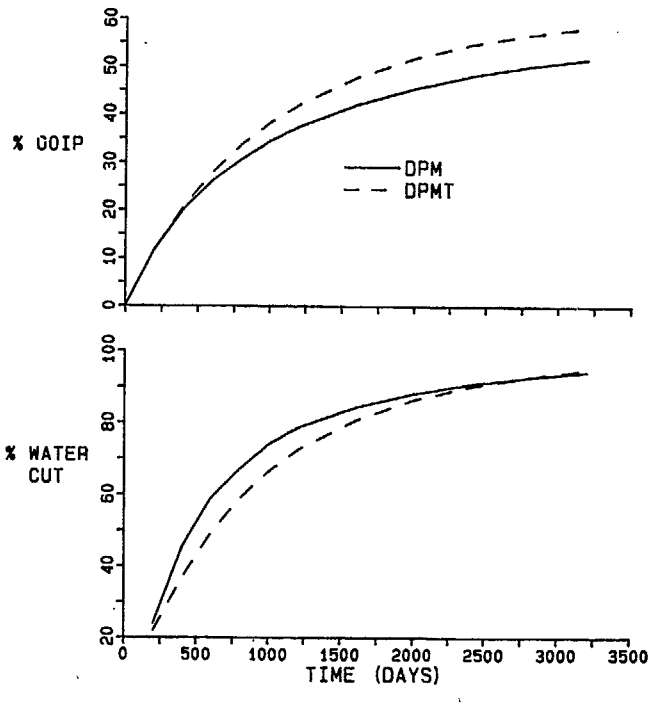

FIGURE 41

TOTAL FIELD A OIL RATE

(91-DAY AVERAGE)

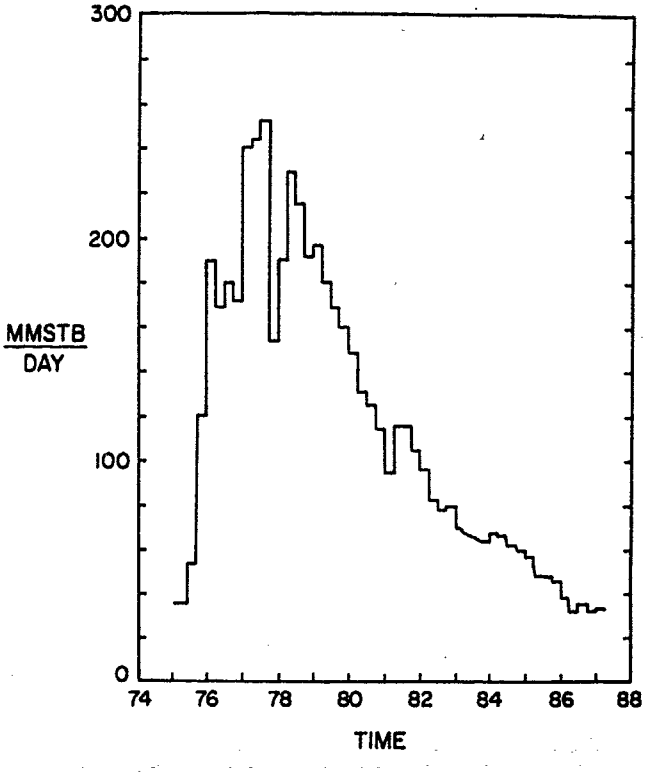

FIGURE 42

TOTAL FIELD A
GAS INJECTION RATE
(91-DAY AVERAGE)

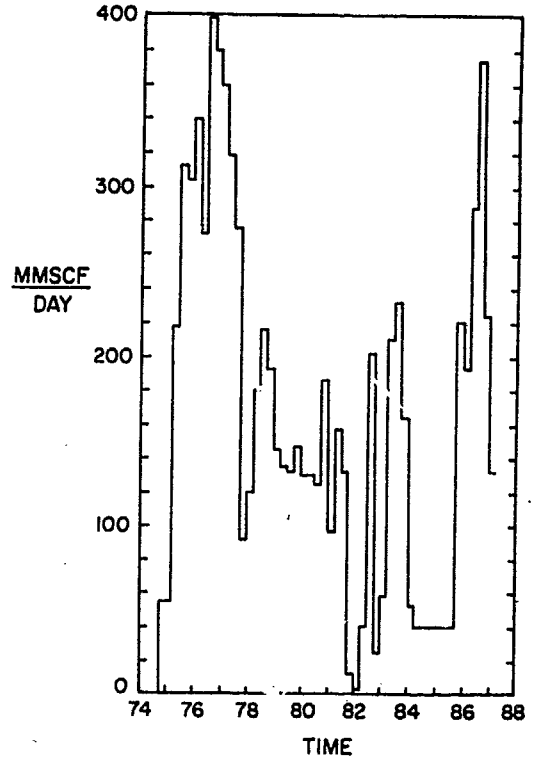

FIGURE 43

CALCULATED FRACTURE S_o VS. TIME

GAS INJECTION WELL 39, LAYER 2

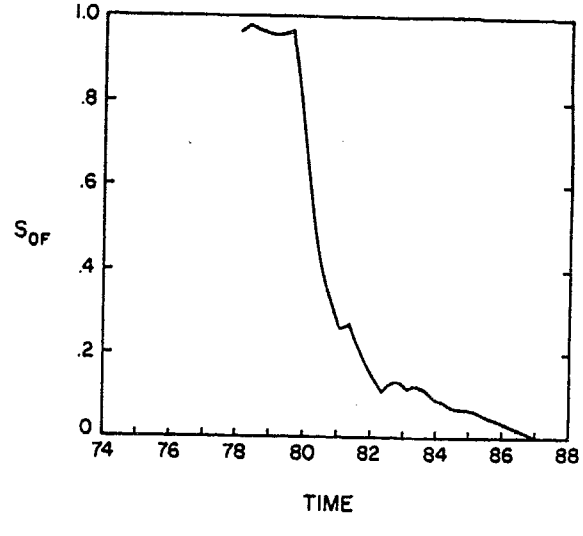

FIGURE 44

RESERVOIR A GOR

— OBSERVED
ooo DPM
S_{ge} - DEPENDENT UPON DENSITIES AND TENSION WITH DIFFUSION

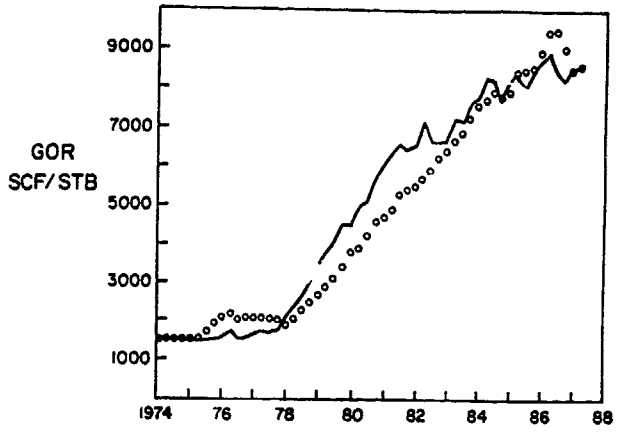

FIGURE 45

N_2 INJECTION STARTING 1981